

ULTRACOLD METASTABLE CALCIUM ATOMS  
IN A BICHROMATIC MAGNETO-OPTICAL TRAP

DISSERTATION  
zur Erlangung des Doktorgrades  
des Fachbereichs Physik  
der Universität Hamburg

vorgelegt von  
Jan Grünert  
aus Mainz

Hamburg  
2002

Gutachter der Dissertation

Prof. Dr. Andreas Hemmerich  
Prof. Dr. Claus Zimmermann  
Prof. Dr. Rudolf Grimm

Gutachter der Disputation

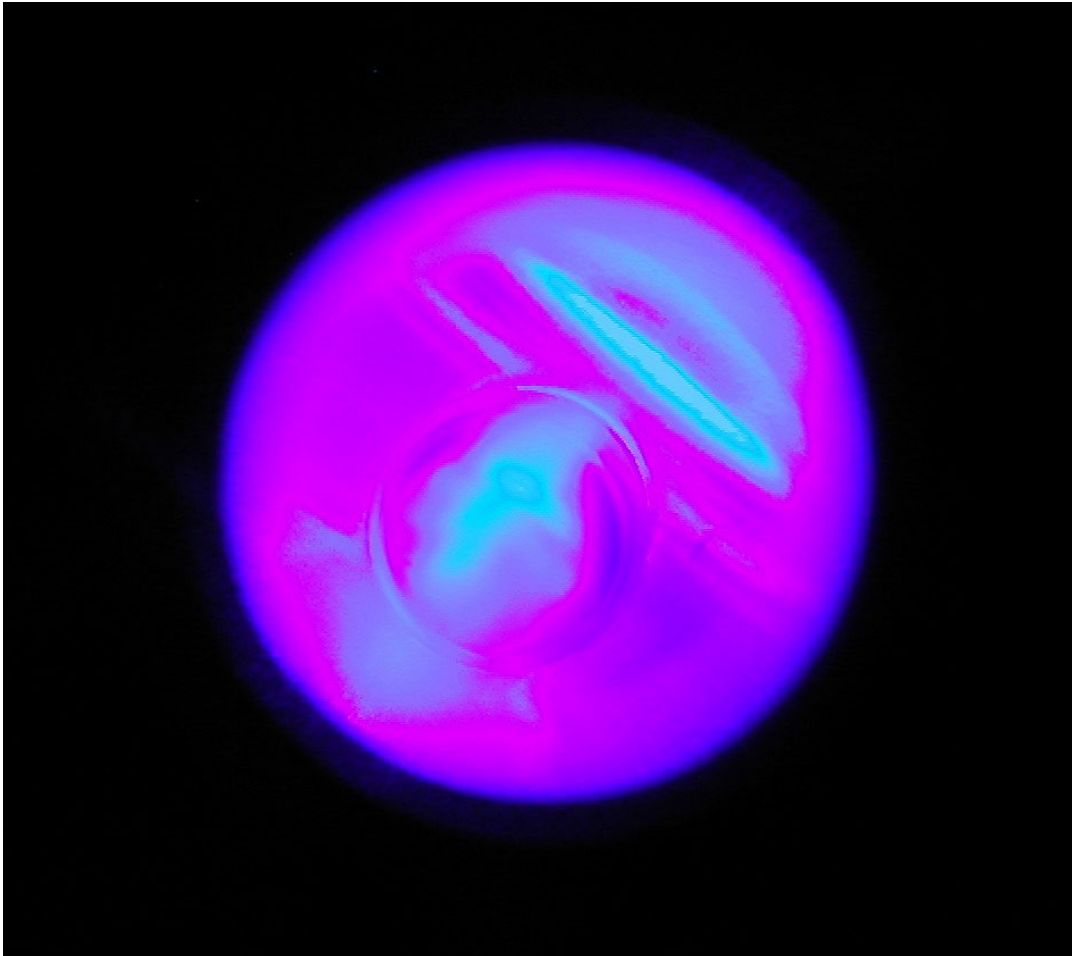
Prof. Dr. Andreas Hemmerich  
Prof. Dr. Klaus Sengstock

Datum der Disputation

15. Mai 2002

Dekan des Fachbereichs Physik

Prof. Dr. F.-W. Büßer



to Ad, Ina, Anke and Karmen

# Contents

<b>List of Figures</b>	<b>6</b>
<b>List of Tables</b>	<b>8</b>
<b>List of Abbreviations</b>	<b>11</b>
<b>Summary, Zusammenfassung</b>	<b>12</b>
<b>1 Introduction</b>	<b>13</b>
1.1 The physics of cold dilute gases . . . . .	13
1.2 Scope of this thesis . . . . .	16
1.2.1 Matter wave amplification by optical pumping . . . . .	16
1.2.2 MAO in calcium . . . . .	17
1.2.3 Efficient loading of the reservoir state with cold atoms . . . . .	18
1.2.4 Laser cooling of earth-alkalis . . . . .	18
1.2.5 Summary . . . . .	19
1.3 Perspectives . . . . .	19
1.4 Applications . . . . .	20
<b>2 A tour through the calcium atom</b>	<b>22</b>
<b>3 Vacuum system</b>	<b>26</b>
3.1 The source chamber . . . . .	26
3.2 The atomic beam . . . . .	30
3.3 Between chambers . . . . .	32
3.4 The main chamber . . . . .	34
3.4.1 General shape and attached components . . . . .	34
3.4.2 Viewports . . . . .	34
3.4.3 Zeeman slower window section . . . . .	36
3.4.4 Main chamber ion pump . . . . .	36
3.5 Baking . . . . .	37
3.6 Vacuum quality assessment . . . . .	38
<b>4 Sources of light</b>	<b>40</b>
4.1 Resonators . . . . .	40
4.1.1 Theoretical description . . . . .	40

4.1.2	Stability of resonators . . . . .	41
4.1.3	Mode matching of resonators . . . . .	43
4.2	Titanium sapphire laser . . . . .	44
4.2.1	Standing-wave resonator . . . . .	45
4.2.2	Output mode . . . . .	48
4.2.3	Pump laser . . . . .	49
4.2.4	Cooling water cycle . . . . .	50
4.2.5	Long-term stabilization of the Ti:sapphire laser . . . . .	51
4.3	Frequency doubling, shifting, and stabilization . . . . .	52
4.3.1	Locking the doubling cavity to the Ti:sapphire laser . . . . .	53
4.3.2	Environment for the nonlinear crystal $\text{KNbO}_3$ . . . . .	53
4.3.3	Improved sum frequency generation using an LBO crystal . . . . .	54
4.3.4	Frequency shifting . . . . .	56
4.3.5	Stabilization of the 423 nm radiation to the calcium line . . . . .	57
4.4	A solid state laser for 2 $\mu\text{m}$ radiation . . . . .	59
4.5	The diode laser for optical pumping at 430 nm . . . . .	64
4.5.1	Littrow configuration . . . . .	64
4.5.2	Frequency doubler . . . . .	64
4.6	Spectroscopy of calcium in gas discharge lamps . . . . .	65
4.7	A stabilized diode laser for 657 nm . . . . .	67
4.7.1	Components . . . . .	67
4.7.2	Output mode . . . . .	68
4.7.3	Spectroscopy of the atomic transition . . . . .	69
4.8	Detectors . . . . .	71
4.9	The optical table . . . . .	73
<b>5</b>	<b>Deceleration of an atomic beam</b>	<b>74</b>
5.1	How to slow atoms using laser light . . . . .	74
5.2	Transverse heating . . . . .	76
5.3	Calculation of the current distribution for the Zeeman slower field . . . . .	77
5.4	Inductivity of the slower solenoid . . . . .	79
5.5	Choosing the right power supply . . . . .	79
5.6	Test of the experimentally realized Zeeman slower magnetic field . . . . .	80
<b>6</b>	<b>Trapping neutral atoms in magneto-optical traps</b>	<b>81</b>
6.1	Principle of operation . . . . .	81
6.2	MOT coils . . . . .	83
6.3	Collection of atoms into the trap . . . . .	84
6.3.1	Capture range . . . . .	84
6.3.2	The atomic beam and gravitation . . . . .	86
6.4	MOT description . . . . .	86
6.4.1	Calibration of the trapped particle number detection . . . . .	87
6.4.2	Trap loss models and rate equations in equilibrium . . . . .	88
6.5	Metastable trap . . . . .	93
6.5.1	Estimation of the infrared fluorescence . . . . .	93

6.5.2	Detection of metastable atoms . . . . .	94
6.5.3	Forces acting upon the trapped metastable atoms . . . . .	95
<b>7</b>	<b>Results</b>	<b>96</b>
7.1	Preparatory measurements . . . . .	96
7.2	Lifetime of the metastable MOT . . . . .	97
7.3	Temperature of the metastable atoms . . . . .	100
7.3.1	Time-of-flight experiment — recapture method . . . . .	100
7.3.2	Time-of-flight experiment — light carpet method . . . . .	105
<b>8</b>	<b>Perspectives</b>	<b>108</b>
8.1	Near-future improvements . . . . .	108
8.2	Light shift trap . . . . .	110
8.2.1	The physical phenomenon . . . . .	110
8.2.2	Dipole trap . . . . .	111
8.2.3	Cooling while trapping . . . . .	112
<b>A</b>	<b>Calcium data</b>	<b>114</b>
A.1	Landé $g$ -factors . . . . .	115
A.2	Spectroscopic data . . . . .	116
<b>B</b>	<b>Useful numbers, equations and relations</b>	<b>117</b>
B.1	Physical constants, conversion factors, and material properties . . . . .	117
B.2	Mathematical relations . . . . .	119
<b>C</b>	<b>Technical data and procedures</b>	<b>120</b>
C.1	Specifications, dimensions, and mechanical drawings . . . . .	120
C.2	Adjustment of Tm:YAG resonator . . . . .	128
C.3	Wavelength measurement . . . . .	129
C.4	Impedance measurement . . . . .	129
C.5	Temperature stabilization . . . . .	130
<b>D</b>	<b>Appliances and materials</b>	<b>131</b>
	<b>Bibliography</b>	<b>134</b>
	<b>Index</b>	<b>143</b>
	<b>Publications</b>	<b>146</b>
	<b>Acknowledgement</b>	<b>147</b>
	<b>Curriculum Vitae</b>	<b>149</b>

# List of Figures

1.1	Theoretical scheme of MAO . . . . .	16
1.2	Implementation of MAO using neutral calcium atoms . . . . .	17
1.3	Efficient supply of cold atoms into the metastable triplet state . . . . .	18
2.1	Electronic ground state of a neutral calcium atom . . . . .	22
2.2	Energy levels and transition in neutral calcium . . . . .	24
3.1	Rough vacuum components . . . . .	27
3.2	Photograph of the UHV chamber . . . . .	33
4.1	Equivalence picture . . . . .	42
4.2	Bow-tie resonator . . . . .	42
4.3	Resonator stability plot . . . . .	43
4.4	Illustration of mode matching with a single lens . . . . .	43
4.5	Fabry-Perot spectrum of the Ti:sapphire laser . . . . .	45
4.6	Ti:sapphire output coupler etalon . . . . .	46
4.7	Photograph of the Ti:sapphire laser . . . . .	48
4.8	Stability range of the Ti:sapphire laser . . . . .	49
4.9	Ring resonator in the Verdi laser head . . . . .	50
4.10	Stabilizing Fabry-Perot etalon setup . . . . .	52
4.11	Photograph of the frequency doubling ring resonator for the LBO crystal . . . . .	55
4.12	Detection and amplification of fluorescence at the calcium cell . . . . .	58
4.13	Main calcium resonance at 423 nm in the atomic beam cell . . . . .	58
4.14	Tm:YAG term scheme . . . . .	60
4.15	Machine shop drawing of the Tm:YAG resonator . . . . .	61
4.16	Photograph of the Tm:YAG-resonator . . . . .	61
4.17	Dual-mode behaviour of Tm:YAG laser . . . . .	62
4.18	Output power of the Tm:YAG laser versus pump power . . . . .	62
4.19	Pound-Drever-Hall lock for the KNbO <sub>3</sub> resonator . . . . .	65
4.20	Schematic of the calcium discharge lamp . . . . .	66
4.21	Saturation spectroscopy setup for the 1978 nm line . . . . .	67
4.22	Photograph of the diode laser setup . . . . .	68
4.23	Optical components of the 657 nm laser system . . . . .	69
4.24	Scan of the 657 nm laser across the intercombination line . . . . .	70
4.25	PMT response to application of light at 657 nm . . . . .	72

5.1	Axial magnetic slower field shape . . . . .	80
6.1	Operation scheme of a standard MOT . . . . .	82
6.2	Energy level diagram as used for rate equations . . . . .	89
6.3	Trap decay and loading for regular operation and with repumping . . . . .	93
6.4	Increased steady-state fluorescence of the GS-trap by applying 430 nm light . . . . .	95
7.1	Saturation spectroscopy signal of the transition $^3P_2$ to $^3D_3$ . . . . .	96
7.2	Decreasing fluorescence peaks map out the IR-MOT lifetime . . . . .	99
7.3	Partial trapping due to insufficiently attenuated infrared MOT beams . . . . .	100
7.4	Pulse sequence and fluorescence signal of the recapture experiment . . . . .	101
7.5	The lifetime and the temperature of the metastable atoms in the IR-MOT . . . . .	104
7.6	Time-of-flight measurement using a sheet of resonant light . . . . .	105
8.1	Schematic of resolved sideband cooling in a dipole trap . . . . .	112
8.2	Qualitative dependance of the Doppler cooling force on detuning . . . . .	113
8.3	Light shift of the levels $^3P_1$ and $^1S_0$ for circular polarization . . . . .	113
C.1	Schematic of the mounted LiNbO <sub>3</sub> crystal . . . . .	122
C.2	Temperature dependence of the tantalum heater wire resistance . . . . .	122
C.3	Schematic of power supply for main calcium oven . . . . .	123
C.4	Wollaston prism as used in polarization spectroscopy setup . . . . .	123
C.5	Calcium oven capsule - atomic beam source . . . . .	126
C.6	Technical drawing of the heat shield that surrounds the main calcium oven . . . . .	127
C.7	Detection circuit for the hollow cathode lamp impedance . . . . .	129
C.8	Low pass filter ( $f_{3dB} = 10$ Hz) in high voltage power supply . . . . .	130



# List of Tables

2.1	Atomic data for major isotopes of Group II elements and Yb . . . . .	23
3.1	Laser cooling data, comparing alkali and earth-alkali atoms . . . . .	28
3.2	Optimal atomic flux - the Lucas description . . . . .	32
3.3	Magnetizability of stainless steel materials . . . . .	34
3.4	Viewport substrate, Helicoflex gasket and coating mask dimensions . . . . .	35
3.5	Leak test data for the KF16 gate valve . . . . .	39
4.1	Free spectral ranges (FSR) of wavelength selective elements . . . . .	45
4.2	Technical data of Ti:sapphire resonators . . . . .	47
4.3	Sagittal and tangential beam parameters . . . . .	49
4.4	Measured beam parameters of the Ti:sapphire laser output beam . . . . .	50
4.5	VERDI beam parameters . . . . .	51
4.6	Refractive indices of LBO . . . . .	55
4.7	FSR and tuning range of the wavelength selective elements in the Tm:YAG resonator . . . . .	60
4.8	Examples of narrow, far infrared calcium lines observed with the hollow cathode lamp . . . . .	65
4.9	Spectral ranges of detectors . . . . .	71
5.1	Fit parameters for the length and radius of the slower solenoid layers . . . . .	78
5.2	Fit parameters for the positions and strengths of the magnet coils . . . . .	79
6.1	Trapping parameters for the ground-state and metastable MOT . . . . .	85
A.1	Physical and chemical properties of calcium [122] . . . . .	114
A.2	Natural abundances above 0.1% of stable calcium isotopes [111]. . . . .	115
A.3	Calcium vapor pressure . . . . .	115
A.4	Landé $g$ -factors for $^{40}\text{Ca}$ . . . . .	116
A.5	$^{40}\text{Ca}$ line data . . . . .	116
B.1	Physical constants . . . . .	117
B.2	Radio frequency power conversion . . . . .	117
B.3	Specific resistivities . . . . .	118
B.4	Material densities . . . . .	118
B.5	Destruction threshold of dielectric coatings . . . . .	118
B.6	Limitations in mechanical engineering . . . . .	118

B.7	Ray transformation matrices for selected optical elements [70]	119
B.8	Confocal Fabry-Perot etalon	119
C.1	Dimensions of magnetic field coils	120
C.2	Tm:YAG-laser data	121
C.3	Specifications of the LiNbO <sub>3</sub> crystal	121
C.4	Detectivity, response time, and responsivity of FIR-detectors at 2 $\mu\text{m}$	123
C.5	Specifications of piezoelectric tubes	124
C.6	Fabry-Perot etalon for analysis of the 657 nm laser	124
C.7	Anti-reflection coatings produced at the ILP	124
C.8	Dielectric coatings produced at the ILP	124
C.9	Dielectric filters	125
C.10	Verdi operating parameters	125
C.11	Calibration data for high voltage supply NSHV-3,5 kV	125
C.12	Response of temperature sensitive sheets to 1978 nm radiation	125
C.13	Detector operating parameters	125
C.14	Accuracy of wavemeter reading	129

# List of Abbreviations

AFG	arbitrary function generator
AOI	angle of incidence
AOM	acousto-optical modulator
AR	antireflection (coating)
BEC	Bose-Einstein-condensate / -condensation
CF	conflat flange
ECDL	extended cavity diode laser
EIT	electromagnetically induced transparency
ENI	equivalent noise input
EOM	electro-optical modulator
FOM	figure of merit
FORT	far-off-resonance optical-dipole trap
FP	Fabry-Perot
FSR	free spectral range
GS	ground state
HR	high reflection (coating)
ID	inner diameter
ILP	Institute for Laser Physics (Hamburg)
IR	infrared
KF	quick flange
LBO	lithium tetraborate ( $\text{Li}_2\text{B}_2\text{O}_4$ )
LD	laser diode
MAO	matter wave amplification by optical pumping
MOT	magneto-optical trap
MS	mass spectrometer
Nd:YVO <sub>4</sub>	neodymium doped yttrium vanadate
OD	outer diameter
OP	operational amplifier
PbS	lead-sulphide
PD	photo diode
ROI	region of interest
SHG	second harmonic generation
Ti:Sa	titanium sapphire ( $\text{Ti:Al}_2\text{O}_3$ )
Tm:YAG	thulium doped yttrium aluminium garnet
TOF	time-of-flight
TP	turbo pump
UHV	ultra high vacuum
VCO	voltage controlled oscillator
VSCPT	velocity-selective coherent population trapping
YAG	yttrium aluminium garnet

## Summary

This thesis explores a particularly efficient method for the production of large samples of ultracold calcium atoms that are required to create a continuous source of coherent matter waves. The existence of extremely long-lived metastable states is used in combination with a narrow band, closed cycle, infrared transition. An optimized conventional magneto-optical trap (MOT) collects atoms from a Zeeman cooled atomic beam using a strong dipole transition within the singlet system. The temperature of the trapped atomic sample is Doppler-limited due to the lack of ground state Zeeman-structure. The cooling transition is not completely closed thus yielding an intense flux of above  $10^{10}$  atoms/s into the metastable triplet state  $^3P_2$ . The ground-state MOT lifetime of 23 ms is mainly limited by this decay channel and not by inelastic collisions.

A second magneto-optical trap sharing the same magnetic field gradient is superimposed which captures and further cools the metastable atoms using the narrow-band infrared transition  $^3P_2 \rightarrow ^3D_3$ . In the present experiment we prepared  $3 \times 10^8$  atoms within 250 ms at temperatures below 20  $\mu\text{K}$ . Minor technical improvements of the setup promise to yield more than  $10^{10}$  atoms at sub-microkelvin temperatures within one second.

This approach offers a combination of very low temperatures and remarkably large sample sizes, which opens up perspectives to reach quantum degeneracy in forthcoming experiments.

## Zusammenfassung

Im Rahmen dieser Arbeit wird eine besonders effiziente Methode zur Erzeugung einer großen Anzahl ultrakalter Kalziumatome untersucht, welche benötigt werden, um eine kontinuierliche Quelle kohärenter Materiewellen zu realisieren. Dazu werden äußerst langlebige metastabile Zustände kombiniert mit einem schmalbandigen geschlossenen infraroten Übergang. Eine optimierte konventionelle magneto-optische Falle fängt Atome aus einem Atomstrahl, der mittels eines starken Dipol-Übergangs zwischen Singulett-Zuständen durch Zeeman-Technik gekühlt wurde. Die Temperatur der gefangenen Atome ist Doppler-begrenzt, weil der Grundzustand von Kalzium keine Zeemanstruktur aufweist. Der Kühlübergang ist nicht vollständig geschlossen, wodurch ein intensiver Fluß von über  $10^{10}$  Atomen pro Sekunde in den metastabilen Zustand  $^3P_2$  erfolgt. Die Lebensdauer der Grundzustandsfalle von 23 ms wird maßgeblich durch diesen Zerfallskanal und nicht durch inelastische Stöße begrenzt.

Eine zweite magneto-optische Falle, die der ersten überlagert ist und somit den gleichen Magnetfeldgradienten verwendet, fängt die metastabilen Atome ein und kühlt sie weiter auf dem schmalbandigen Übergang  $^3P_2 \rightarrow ^3D_3$ . Im vorliegenden Experiment konnten  $3 \times 10^8$  Atome innerhalb von 250 ms auf Temperaturen unter 20  $\mu\text{K}$  gebracht werden. Geringe technische Verbesserungen des Aufbaus sollten erlauben, mehr als  $10^{10}$  Atome innerhalb einer Sekunde auf Submikrokelvin-Temperaturen zu bringen.

Diese Methode stellt eine besonders große Anzahl von Teilchen bei sehr tiefen Temperaturen zur Verfügung, wodurch die Perspektive eröffnet wird, in anschließenden Experimenten Quantenentartung zu erreichen.

# Chapter 1

## Introduction

### 1.1 The physics of cold dilute gases

Laser cooling is an experimental method that allows to decrease the temperature of a dilute atomic gas to very near the absolute zero. Implicitly the foundations of laser cooling can already be found in Einstein's theoretical work [38] of 1917 on quantum theory, where interactions between atoms and light are analyzed. He described the thermalization of molecular gases in the radiation field of a thermal light source. This thermalization could however not be used for efficient cooling of gases as long as only thermal light sources were available.

The advent of the laser in the early 1960's presented devices with exceptionally narrow spectral lines. Another 15 years later Hänsch and Schawlow picked up Einstein's basic ideas when they suggested to apply laser light to cool dilute gases of neutral atoms [51], and in the same year Wineland and Dehmelt proposed a similar concept for ions [124]. The atoms are sent through a light field created by three orthogonal pairs of counterpropagating laser beams. In this *optical molasses* the atoms are slowed down like particles in a glass of sirup, but they are not trapped.

It took another decade until the invention of the magneto-optical trap [100] sparked the explosive expansion of research in the new-born field of laser cooling and trapping. This trap combines the cooling forces of optical molasses with an inhomogeneous magnetic field that allows to capture the atoms at one location in space. Three prominent researchers with important input during this era were honored with the Noble Prize 1997 in physics, Steve Chu, Claude Nobel lectures [22, 27, 95] give a thorough and detailed view on the foundations of this field.

In 1985 a three-dimensional optical molasses of sodium atoms at a density of  $10^6 \text{ cm}^{-3}$  and a temperature of  $240 \mu\text{K}$  was demonstrated by Chu et al. [23]. In 1989 Prentiss et al. created a beam of sodium atoms at a density of  $> 10^8$  with  $10 \text{ m/s}$  velocity spread which corresponds to a temperature of  $150 \mu\text{K}$ . The phase space density was 100 times that of the original Maxwell distribution [98].

Experimental physicists are used to discover less than expected, but in 1988 an experimental result [80] surpassed their expectations: the measured temperature of a cloud of

laser cooled atoms was lower<sup>1</sup> than the theoretical limit! Until then the Doppler temperature was believed to be the ultimate limit according to the accepted laser cooling theory. The new cooling mechanism was finally explained in 1989 by the teams of Chu and Cohen-Tannoudji [31]. Reminiscent of the tragic hero in Greek mythology it was called *Sisyphus Cooling*: a particle is pushed up a potential hill until near the top it is forced into a different internal energy state only to find itself at the lowlands of another potential slope to climb.

After the limit was once crossed several methods were explored to obtain sub-recoil temperatures, e.g. in 1988 one-dimensional cooling by *velocity-selective coherent population trapping* (VSCPT) [4], in 1991 the use of *velocity-selective resonances* (VSR) [109], in 1992 *Raman cooling* using velocity-selective stimulated Raman transitions [62]. 3D-VSCPT was first observed in 1995 with metastable helium at 180 nK [77].

Although impressive — reaching very low temperatures was never the only goal that laser cooling aimed for: the real challenge was to increase the phase space density, thus decreasing temperature while increasing the density of trapped particles. Again, it was Einstein together with the Indian physicist Bose who predicted as early as 1924 a very peculiar effect for bosons reaching a phase space density on the order of one [15, 39]. According to their theory the increasing atomic de Broglie wavelength at decreasing temperatures should lead to an increasing wavefunction overlap among the atoms in case of high densities. At some critical temperature the de Broglie wavelength would reach the same order of magnitude as the macroscopic size of the atomic cloud, and a phase transition would occur, not transforming the cold gas into a liquid but into a new state of matter, a macroscopic manifestation of quantum theory, now called *Bose-Einstein condensate* (BEC) in honor of the original proposers.

It took some 50 years following the proposal, but finally laser cooling had matured to a point where experiments succeeded to prepare such cold and dense gaseous atomic samples to achieve Bose-Einstein condensation. In 1995 two research groups created BEC's of rubidium [2] and sodium [32]. The team leaders, Eric Cornell and Carl Wieman at NIST as well as Wolfgang Ketterle at the MIT, received the Nobel prize 2001.

Also in 1995, Bose-condensation in lithium was achieved by Randy Hulet at Rice University, Texas [17]. Other labs in the U.S. and in Europe followed, mainly with rubidium condensates of different characteristics using a number of different geometries of magnetic traps. The BEC experiments until 1997 are discussed in the review article [88], while [60] is a broad collection of articles on the subject of BEC.

Laser cooling is a very powerful method to quickly reach low temperatures, but at some point the laser light has to be switched off in order to further cool the sample – the heating rate due to reabsorption of scattered light then poses the temperature limit. All BEC experiments until today need an additional technique to bridge this last gap towards condensation.

Here a method comes into play that everyone knows from the morning coffee cup: blowing away the hottest coffee particles in the vapor phase above the liquid will greatly increase the cooling rate of the whole system. In the same way *evaporative cooling* [54] serves as a final step towards condensation of the trapped atomic ensemble.

In evaporative cooling the idea is thus to expel atoms from a trap that carry more

---

<sup>1</sup>optical molasses of sodium atoms at  $T_{\text{exp}} = 43 \pm 20 \mu\text{K}$  while  $T_{\text{doppler}} = 240 \mu\text{K}$

than the average kinetic energy. If a subsequent thermalization through elastic collisions is guaranteed, the resulting temperature of the atoms remaining in the trap will be decreased. Originally introduced to the laser cooling community by people interested in cryotechnology, this method proved very successful and paved the way to BEC.

The two main disadvantages of evaporative cooling are the heavy loss in particle number and the long time required to evaporate and rethermalize. Improvements of magnetic field and laser stability as well as large initial trap populations can guarantee a sufficient amount of condensed atoms, see e.g. [50], where a BEC with  $2 \times 10^5$  condensed atoms was created loading  $1.5 \times 10^9$  atoms into a so-called *time-orbiting potential* (TOP) trap. Today condensates usually contain about  $10^7$  atoms.

Before the advent of laser cooling, the prime candidate for an experimental demonstration of Bose-condensation was spin polarized hydrogen. It can be cooled sympathetically by liquid helium using cryotechnology, and the three-body collision rate leading to molecule formation is negligible. Only later it was realized that for alkalis there also exists an intermediate density regime where the two-body collision rate is sufficiently high for evaporative cooling, but where the three-body collision rate is low enough to allow to reach the quantum degenerate regime of BEC.

Progress in hydrogen experiments towards higher phase space density was steady but slow, so that only in 1998 the group of Dan Kleppner at MIT could finally announce a condensate of atomic hydrogen [41]. It contained  $10^9$  atoms at a peak density of  $5 \cdot 10^{15} \text{ cm}^{-3}$  below a transition temperature of  $50 \mu\text{K}$ .

In the year 2001 another non-alkali element was condensed, at the same time being the first non-ground-state condensate: metastable helium ( $\text{He}^*$ ). The two French institutes who had given themselves an exciting race very much like the groups in 1995, announced their findings within one week from another [19, 94]. The interaction of ultracold metastable rare-gas atoms have been described in [35, 79].

Apart from seeking to condensate ever more atomic species the focus of research interest moved on to the study of BEC behavior and applications. One of the most exciting possibilities is the prospect of *atom lasers* which opened up the completely new field of *atom optics*.

An atom laser<sup>2</sup> is an analogon to a traditional laser where the atoms and photons trade roles: the macroscopic atomic wavefunction of a BEC assumes the place of previous resonator modes, and the resonator is established by the trapping potential instead of mirrors. The output of such a device is no longer a beam of coherent light but instead a *coherent matter wave* [45, 21]. Still missing is unfortunately the equivalent to a pump source keeping the traditional laser alive by creating inversion and therefore refilling photons into the resonator, compensating the losses due to intra-cavity deficiencies and outcoupling. Conventional BEC experiments can operate atom lasers only in a non-continuous way where the duty cycle is restricted by the considerable delay time that is required to recreate a new condensate once the original trap population is consumed [87, 1, 13].

---

<sup>2</sup>sometimes also called *boser*

## 1.2 Scope of this thesis

The work presented in this thesis commenced under the impression of the aforementioned experiments. To abandon the time-consuming step of evaporative cooling in Bose-condensation, several all-optical techniques have been proposed and their principles experimentally explored, such as ground state laser cooling using *electromagnetically induced transparency* (EIT) [91]. Only very recently an all-optical method actually produced a BEC of rubidium atoms<sup>3</sup> in an optical trap created by two crossed CO<sub>2</sub>-laser beams [6], again using evaporative cooling as a final step before condensation.

However, in 1995 Janicke and Wilkens proposed a scheme for a continuous atom laser [112, 5] that relied on matter wave amplification by optical pumping (MAO) as it was called later [61]. This all-optical scheme which does not rely on evaporation will be described below, since its implementation is the leading motivation for this research project.

### 1.2.1 Matter wave amplification by optical pumping

In MAO, atoms in the ground state are trapped in the potential of a dipole trap or an optical lattice. Like in a conventional three level laser three energy levels are required: two ground states  $|g_1\rangle$  and  $|g_2\rangle$ , well separated in energy and without transitions between them, and an excited state  $|e\rangle$  that couples the higher ground state  $|g_2\rangle$  (called *reservoir state*) to the absolute ground state  $|g_1\rangle$ , see figure 1.1. Before the process can start, atoms must

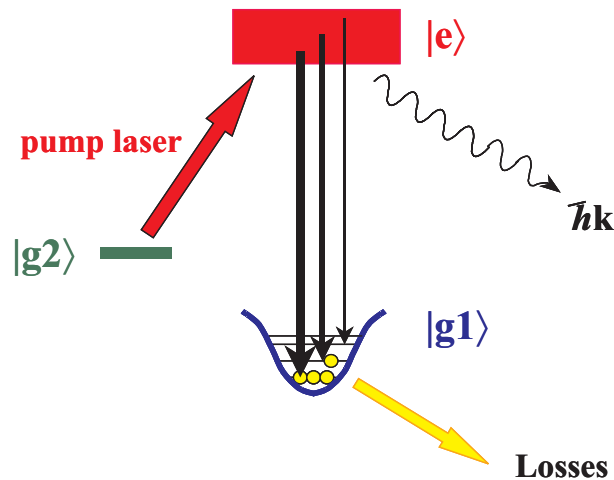


Figure 1.1: Theoretical scheme of MAO

be accumulated in the upper, metastable ground state  $|g_2\rangle$ . Some mechanism has to exist to continuously refill the reservoir state with precooled atoms. Then an optical excitation, the pump laser, can bring atoms to the excited state from where they will decay into  $|g_1\rangle$ . This state offers a ladder of vibrational levels due to the trapping potential. When bosons are used, the final transition will preferentially connect to vibrational levels with a high initial population, which is called *bosonic enhancement*. One can think of this last

<sup>3</sup>the condensate fraction contained  $3.5 \times 10^4$  atoms



transition as a stimulated emission of an atom into a mode of the coherent matter wave. Most importantly, in case of a dominant population of the lowest vibrational level, almost every atom coming from the excited state  $|e\rangle$  is bosonically attracted into this lowest level, a macroscopic population in a single mode jumps into existence, thus a BEC is created, and the atom laser starts. One condition for this is that the reservoir atoms are already cold enough, since the initial population distribution among the vibrational levels in the ground state trap reflects the temperature of the sample before laser action has started. If the initial temperature is too high, then the lower vibrational levels will have nearly equal population, and no bosonic enhancement will favor a transition into the lowest vibrational level – the laser will not start.

In stark contrast to the existing atom lasers as described in the last section, this scheme allows continuous reloading of the condensate without disturbing it and therefore a continuous atom laser operation.

To complete the analogy to conventional lasers, losses are here manifested again by outcoupling and by losses due to collisions in the optical trap such as light-assisted inelastic two-body collisions.

### 1.2.2 MAO in calcium

Earth-alkali atoms, found in the second column of the periodic table of elements, are particularly suited for an experimental implementation of the MAO scheme: due to their two valence electrons the earth-alkalis have two separate energy level systems, the spin zero singlet states and the spin one triplet states. Transitions between both systems are spin-forbidden and thus usually weak.

In calcium we found the perfect candidate for MAO [48]. One of the lowest triplet states is metastable with a calculated lifetime of about two hours [34]. This state can act as a reservoir state  $|g_2\rangle$ , see figure 1.2. A weak link from the first excited level in the singlet

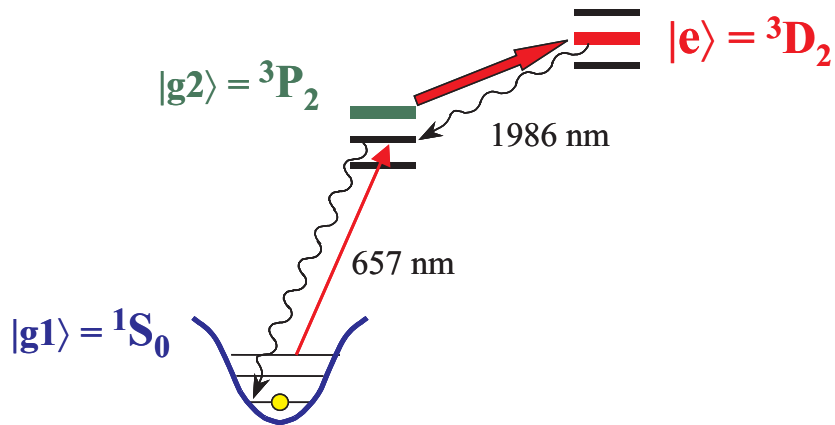


**Figure 1.2:** Implementation of MAO using neutral calcium atoms

states to the metastable state can provide the required reloading with precooled atoms, that have been laser cooled and trapped very efficiently on the main calcium transition. Trapping atoms in the absolute ground state with a dipole trap should not impose new

difficulties apart from the ones encountered in alkali experiments [46, 26]. The metastable atoms can be excited to a level that decays to a triplet state which in turn is connected to the ground state  $|g_1\rangle$  via a narrow intercombination line. One last requirement for the implementation of MAO in calcium is the reservoir state loading.

### 1.2.3 Efficient loading of the reservoir state with cold atoms

The reservoir state needs to get populated at a high rate with already very cold atoms. Calcium is the perfect system for this challenge: its energy level structure provides two separate transitions that are linked by a small transfer channel. This allows to use the strong main transition between the ground state  $^1S_0$  and the first excited state  $^1P_1$  to trap and precool atoms from an atomic beam very efficiently, see figure 1.3. From this ground-

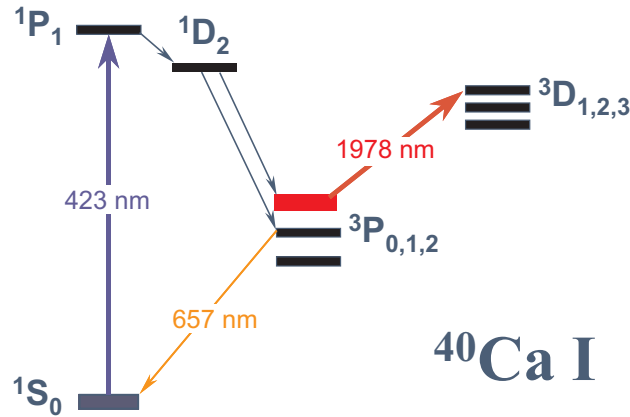


**Figure 1.3:** *Efficient supply of cold atoms into the metastable triplet state*

state trap the metastable triplet state  $^3P_2$  is populated across the intermediate state  $^1D_2$  via a small transfer channel out of the first cooling cycle [78]. Beverini et al. measured a *branching ratio* of  $R = (1.0 \pm 0.15) \times 10^5$  into the  $^1D_2$  state [9]. A second closed-cycle trap operating on the transition  $^3P_2 \longleftrightarrow ^3D_3$  captures the atoms branching off from the main cooling cycle and falling into the metastable state. In contrast to the first trap the fine structure of the metastable triplet state allows for sub-Doppler cooling. Also, the much smaller linewidth and the longer wavelength of the metastable trap transition lead to a lower Doppler and recoil limit. This will be explained in more detail in chapters 2 and 6.

### 1.2.4 Laser cooling of earth-alkalis

Only briefly some laser cooling experiments on other earth-alkalis shall be mentioned to illustrate the progress in this field: already in the early nineties Kurosu and Shimizu worked on laser cooling and trapping of calcium and strontium [72, 73, 71]. Later on especially the work on strontium by the Katori group is important: an optimized design of dipole potentials allowed to load Sr atoms very efficiently into a far-off-resonance optical-dipole trap (FORT) and to proceed with laser cooling in this trap [64]. The minimum temperature

near the photon recoil limit was only 400 nK [63], and thus a high phase-space density exceeding 0.1 was obtained [59]. Although very close, unfortunately the required value for Bose-condensation was not reached since strong losses due to inelastic collisions could not be suppressed. Magnesium features an even narrower intercombination line (30 Hz) than calcium, so progress in laser cooling of this species [53] is often driven by applications in metrology and interferometry [105].

### 1.2.5 Summary

To conclude the scientific goals of this thesis, it was intended to develop a laser cooling experiment that allows the implementation of a matter wave amplification scheme in calcium. The challenge therefore has been to create an optimal flux of already very cold atoms into the reservoir, the metastable triplet state. This goal has been attained by successfully demonstrating a bichromatic MOT with  $3 \cdot 10^8$  metastable atoms at temperatures in the range of 20  $\mu$ K and with loading rates for the metastable trap of close to  $10^{10}$  atoms per second [49].

The main part of this thesis describes the work that has been done to design, build, and operate a suitable experimental system that allows to accomplish the previously mentioned results. Our system consists of an ultrahigh-vacuum system, several smaller vacuum cells, a frequency doubled, high-power laser system driving the main calcium transition, a novel infrared solid-state laser for the metastable trap, a frequency doubled diode laser system for probing, an ultra-stable diode laser to resolve the intercombination line, saturation spectroscopy setups using our own discharge lamps, numerous active feedback-loop circuits for temperature and current controls, and countless other electronics, that we built ourselves to precisely meet our specifications.

Several relevant technologies for efficient laser cooling of calcium have been developed and optimized [47], so that future work on the experiment will be able to proceed with the study of the MAO scheme and other quantum optics issues.

## 1.3 Perspectives

The present status of the experiment allows to continuously produce cold metastable calcium atoms at a high rate. With some minor additions to the apparatus it should be possible in the near future to obtain submicrokelvin temperatures by running the experiment in a pulsed mode where trap loading is terminated at some point to optimize the metastable trap for lowest temperatures. This is achieved by decreasing the magnetic field gradient in the trap, decreasing the power in the trap laser and its detuning from resonance.

A next step will demand for a restructured vacuum system: another small chamber will have to be added on top of the existing main chamber. Cold metastable atoms from the bichromatic trap will be launched into the second chamber, where they get trapped in yet another metastable trap. Since the required technology for this trap has been extensively studied, no fundamentally new problems are expected for the setup of this extension. Adding the upper chamber and transferring atoms to the remote trap will improve several aspects of the experimental setup:

**Lower vacuum pressure** can be reached in the upper chamber by differential pumping and added vacuum pumps at the connection of the chambers.

**The remote trap magnetic field** will no longer have to be shared between two traps, thus an optimized field gradient will allow for lower temperatures in the upper trap while maintaining continuous operation.

**The high energy blue photons** from the ground-state trap that can disturb sensitive quantum measurements are banned from the upper metastable trap.

**Optical access** will be improved in the upper chamber by using a glass cell. This will allow for more flexible implementation of experimental proposals.

In the new chamber the improved optical access will make it possible to install a dipole trap for the ground state. Careful considerations about the dipole trap laser wavelength are necessary to enable *resolved sideband cooling* while trapping. This technique offers an additional temperature reduction to get into the regime where the MAO scheme is proposed to create amplification of coherent matter waves, lighting up a continuous atom laser and thus opening the door to a vast number of new and exciting quantum optics experiments.

## 1.4 Applications

This section will conclude the introduction although it could just as well serve as the beginning: apart from the aforementioned incentives for the creation of ultracold calcium ensembles there are several applications that would benefit from ultracold atoms or which even cannot be realized without them.

### Atomic clocks

Since the early days of atom manipulation using laser light, it was recognized that the very low velocities of laser cooled atoms would prove beneficial for atomic clocks [25]. The width of the atomic resonances, a key parameter for the clock performances, can be significantly reduced with laser cooled atoms. This results from the long interaction time between the atoms and the apparatus which can be achieved with slow atoms.

In 1994, a cold atom clock developed in France at BNM-LPTF was the first to surpass the performances of classical devices with a frequency accuracy of  $3 \times 10^{-15}$  [24]. In this device, called an atomic fountain, cold cesium atoms are launched upwards and fall back due to gravity.

In order to further increase the accuracy of frequency measurements one can increase the absolute value of the frequency by using optical transitions instead of radio frequencies like in conventional atomic clocks. In the last few years cold atom clocks operating in the optical domain were investigated [92, 101, 119]. Earth-alkalis offer narrow intercombination lines thus the attainable accuracy of frequency measurements is high. The short-term stability now approaches 1 Hz in 1 s (using the intercombination line of calcium at 657 nm [92, 93]). Riehle and Helmcke at the PTB/Braunschweig performed high-resolution spectroscopy of

laser cooled calcium [125, 68] which provided the basis for a transportable optical frequency standard [65].

A major deterrent against optical frequency standards was recently removed when an acceptable method for the direct measurement of optical frequencies was found [56], replacing the tedious process of optical frequency comparison through multiple sum frequency generation. This cleared the way for atomic clocks that rely on narrow optical transitions in laser cooled atoms.

## Cold collision studies

Cold collisions have been a field of extensive research in recent years: Gallagher and Pritchard showed in their theory paper [42] from 1989 that the rate of *fine-structure changing collisions* exceeds that of *radiative redistribution*. Burke Jr. et al. developed a theoretical model of two-body ground state collisions of alkali atoms [20]. The Heinzen group studied the photoassociation of ultracold  $^{85}\text{Rb}$  atoms in collaboration with the Dutch theorist Verhaar [43], and in 1998 Gensemer and Gould observed ultracold collisions on the microsecond timescale in real time [44]. A review of cold collision studies was published in 1999 by Weiner et al. [123].

In 1999 theorists initiated cold collision studies of earth-alkali atoms [83, 36]. These atomic species are especially suited for an experimental validation of theoretical cold collision studies since their ground states have no magnetic substructure, and thus the number of collision channels entering the calculations is greatly reduced compared to the situation in alkalis. Trap loss photoassociation spectra in alkalis can be modelled quite precisely for large detunings of the light field. However, alkaline atoms are too complex with their extensive hyperfine structure to allow for theoretical calculations in the small detuning trap loss regime. For earth alkalis and similar elements this is possible, and a theoretical model was presented for Mg [83], Ca, Sr, Ba, and Yb [84]. In 2000 Zinner et al. at the PTB reported the photoassociation of cold calcium<sup>4</sup> atoms [129].

---

<sup>4</sup>The preliminary (June 2000) ab initio result of a high-precision calculation of the calcium  $C_6$ -coefficient is  $C_6(\text{Ca}) = 2694$  atomic units  $\pm 5\%$  (private communication with A. Derevianko, Harvard, Cambridge).

# Chapter 2

## A tour through the calcium atom

This chapter gives a detailed analysis of the properties, peculiarities, and pitfalls of neutral calcium atoms as seen from the perspective of an experimental laser cooling scientist.

### Overview

Calcium is an earth-alkaline element possessing two valence electrons (see figure 2.1) that can add their spins resulting in a total angular spin of  $S=0$  or  $S=1$ . The resulting energy

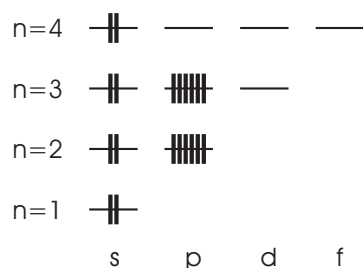


**Figure 2.1:** *Electronic ground state of a neutral calcium atom*

levels are called singlet and triplet states respectively. Transitions between these subsystems are spin-forbidden and therefore weak compared to transitions among levels of equal total spin. The spectral lines associated with these weak transitions are the narrow intercombination lines that are one of the attractions of all earth-alkaline atoms: atomic clocks are based on the measurement of atomic transition frequencies, and therefore the relative accuracy of these clocks increases with decreasing linewidth when the transition frequency itself remains more or less constant.

The following paragraphs introduce the calcium transitions relevant for this experiment which will be excited by laser light fields.

### 423 nm

The strongest line in neutral calcium at 422.6 nm connects the ground state  $^1S_0$  with the first excited singlet state  $^1P_1$ , see also table 2.1 and figure 2.2.

**Table 2.1:** Atomic data for major isotopes of Group II elements and Yb without hyperfine structure (natural abundance shown). This table was taken from [84]. The lifetime  $\tau$  for  $^1P_1$  is taken to be the inverse of the  $^1P_1-^1S_0$  spontaneous emission rate  $\Gamma_{\text{at}}/\hbar$ , thus neglecting weak transitions to other states for Ba and Yb. The linewidth in frequency units is  $\Gamma_{\text{at}}/h = (2\pi\tau)^{-1}$ . The Doppler temperature is defined as  $T_D = \Gamma_{\text{at}}/(2k_B)$  and the recoil temperature as  $T_R = (\hbar^2)/(m\lambda^2k_B)$ , where  $\lambda = \lambda/2\pi$  and  $m$  is the atomic mass. The dipole moment is  $d_0 = \sqrt{3\Gamma_{\text{at}}\lambda^3/4}$  (in a.u.). The atomic units for dipole moment, length, and energy are  $ea_0 = 8.4783 \times 10^{-30}$  Cm,  $a_0 = 0.0529177$  nm, and  $e^2/(4\pi\epsilon_0a_0) = 4.3597482 \times 10^{-18}$  J respectively.

	Be	Mg	Ca	Sr	Ba
Major isotopes without hyperfine structure (abundance)	$^9\text{Be}(100\%)$	$^{24}\text{Mg}(78.99\%)$ $^{26}\text{Mg}(11.01\%)$	$^{40}\text{Ca}(96.94\%)$	$^{88}\text{Sr}(82.58\%)$ $^{86}\text{Sr}(9.86\%)$	$^{138}\text{Ba}(71.70\%)$
$\tau$					
$^1P_1$ (ns)	1.80	2.02	4.59	4.98	8.40
$^3P_1$ (ms)		5.1	0.48	0.021	0.0014
$\Gamma_{\text{at}}/h$					
$^1P_1$ (MHz)	88.5	78.8	34.7	32.0	18.9
$^3P_1$ (kHz)		0.031	0.33	7.5	120
Doppler-cooling limit					
$^1P_1$ (mK)	2.1	1.9	0.83	0.77	0.45
$^3P_1$ (nK)		0.75	8.0	179	$2.8 \cdot 10^3$
Recoil limit					
$^1P_1$ ( $\mu\text{K}$ )	39	9.8	2.7	1.0	0.45
$^3P_1$ ( $\mu\text{K}$ )		3.8	1.1	0.46	0.22
$d_0$ (a.u.)					
$^1S_0-^1P_1$	1.89	2.38	2.85	3.11	3.16
$\lambda$ (nm)					
$^1S_0-^1P_1$	234.861	285.21261	422.6728	460.733	553.548
$\tilde{\lambda} = \lambda/(2\pi)$ ( $a_0$ )					
$^1S_0-^1P_1$	706.4	857.8	1271.2	1385.7	1664.9
FS splitting					
$^3P_2-^3P_0$ (a.u.)	$1.36 \cdot 10^{-5}$	$2.77 \cdot 10^{-4}$	$7.20 \cdot 10^{-4}$	$2.65 \cdot 10^{-3}$	$5.69 \cdot 10^{-3}$

The lifetime of the excited state is short — only 4.6 ns — so that this line is predestined for laser cooling. This can be seen once you remind yourself that Doppler cooling with laser light relies on the net momentum transfer associated with an absorption / emission cycle: in this simplified picture photons repeatedly impinge on the atom with about the same momentum since they originate from a laser which produces a highly collimated flux of photons. The inevitable emission of a spontaneous photon from the excited atom will occur in a random direction, and therefore the change in atomic momentum due to the emitted photons will average out after many emission cycles. The total atomic momentum change is then purely given by the momentum transfer due to the impinging photons presenting a force on the atoms in the propagation direction of the laser. Obviously the force increases with the rate of absorption-emission cycles which scales with the time that the atom spends in the excited state. In other words, the slowing or cooling force increases with decreasing lifetime of the cooling transition<sup>1</sup>.

<sup>1</sup>See <http://www.nobel.se/physics/educational/poster/1997/> for a basic illustration on laser cooling

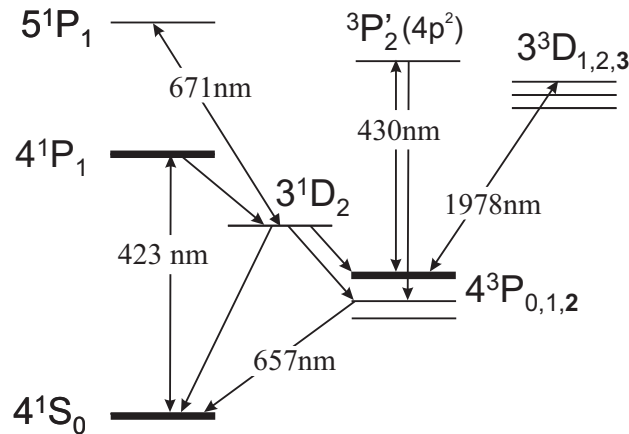


**Figure 2.2:** Energy levels and transition in neutral calcium. Not drawn to scale; only levels relevant to this work are displayed

## 657 nm

The most well known intercombination line in calcium at 657 nm connects the ground state  $^1S_0$  with the triplet state  $^3P_1$  and is the prime candidate for modern optical atomic clocks. A number of recent experiments have used this line for second stage laser cooling after precooling on the strong blue transition [11, 30]. The linewidth of 0.4 kHz is too narrow to allow for direct Doppler cooling in a MOT, but an additional quenching laser can broaden the line by removing population from the excited state into a higher lying energy level. With this *quench cooling* method Binnewies et al. reached calcium temperatures as low as 6  $\mu$ K in a MOT operating on the spin-forbidden transition, quenching via  $4s4d\ ^1D_2$  [11]. Curtis et al. achieved similar 1D-temperatures by cooling and velocity-selecting atoms on the 657 nm transition and quenching with the  $4s4p\ ^3P_1 \rightarrow 4s5s\ ^1S_0$  transition at 553 nm [30].

## 1978 nm and 1986 nm

Another interesting transition at 1978 nm connects the triplet states  $^3P_2$  and  $^3D_3$ . Since this transition has a linewidth of 60 kHz and offers a closed optical pumping cycle  $J = 2 \leftrightarrow J' = 3$  it can be used for laser cooling. The lower state of this transition  $^3P_2$  is metastable with a lifetime of 118 min [34] indicating the feasibility of building a magneto-optical trap using this transition.

A neighboring line at 1986 nm connects  $^3P_2$  and  $^3D_2$ . This transition may be valuable to extract atoms from the metastable state  $^3P_2$ . Once excited to  $^3D_2$  the atoms can not only decay back to  $^3P_2$  but also to  $^3P_1$ , from where they decay to the ground state  $^1S_0$ .

## 671 nm

All earth-alkaline atoms except Mg possess a  $n=3\ ^1D_2$ -state with an energy between the ground state  $n=4\ ^1S_0$  and the first excited state  $n=4\ ^1P_1$ . Therefore, excited atoms in  $^1P_1$  can take an alternative route instead of the direct decay back to the ground state. The



branching ratio into  $^1D_2$  was determined by Beverini et al. [9] as  $R = (1.0 \pm 0.15) \times 10^5$ . The lifetime of the  $^1D_2$ -state is  $3.1 \pm 0.3$  ms according to theory [7], and in experiment  $2.3 \pm 0.5$  ms were found [58]. To close the sometimes undesired path into  $^1D_2$  one can pump atoms to  $n=5$   $^1P_1$  immediately after they have fallen into  $^1D_2$  (see e.g. [92]) and before they can decay into long-lived triplet states. In calcium a laser at 671 nm is required for this optical pumping process. From the higher  $^1P_1$  state the atoms have several decay channels, the most probable one leads back to the original  $^1D_2$  state. Averaged over a few cycles though the most likely decay is down to the ground state  $^1S_0$  where they end up quickly enough to be recaptured in the ground-state trap since the pumping time is in the order of microseconds. This method is used in ordinary earth-alkaline ground-state traps to prolong their lifetime and to increase the number of trapped atoms in the steady state.

# Chapter 3

## Vacuum system

*L'Être par qui le Néant arrive dans le monde  
est un être en qui, dans son Être, il est question du Néant de son Être:  
l'Être par qui le Néant vient au monde doit être son propre Néant.*  
Sartre [106, p.59]

This part of my thesis is dedicated to the various components of the vacuum system that create a suitable environment for laser cooling experiments. This goal is achieved when unwanted collisions with background atoms occur at a rate that is lower than any other loss channel associated with the cooling process. As we will see, at consecutive steps of the experiment varying degrees of vacuum requirements apply.

The ultrahigh vacuum (UHV) system can be separated into three logical units as follows: in the source chamber an oven produces a thermal beam of neutral calcium atoms. These atoms enter a connecting tube where Zeeman cooling is applied to them. Leaving the tube they enter the main vacuum chamber, where they get trapped and further cooled. Although not strictly a vacuum component, I will also describe the oven in the vacuum section since its prerequisites dictate the design of the source chamber. The characteristics of the atomic beam leaving the oven will also be discussed.

To pump the system down from atmospheric pressure and to operate turbomolecular pumps that are attached to the source and main chamber a *foreline vacuum* setup is necessary. It provides a rough vacuum on the  $10^{-2}$  to  $10^{-3}$  mbar level at the turbo pump exhaust and thus reduces the required gas compression by the turbo pumps by several orders of magnitude. At steady-state the foreline pressure gauge<sup>1</sup> gives a reading of  $< 5 \cdot 10^{-4}$  mbar. The components<sup>2</sup> of the rough vacuum side are depicted in figure 3.1.

### 3.1 The source chamber

There are two common options to produce and trap a dilute atomic gas in experiments with metallic alkali or earth-alkali elements:

---

<sup>1</sup>Pirani gauge: Thermovac transmitter TTR 221S by Leybold; range  $5 \cdot 10^{-4}$  to  $1 \cdot 10^3$  mbar

<sup>2</sup>The foreline pump is described on page 131.

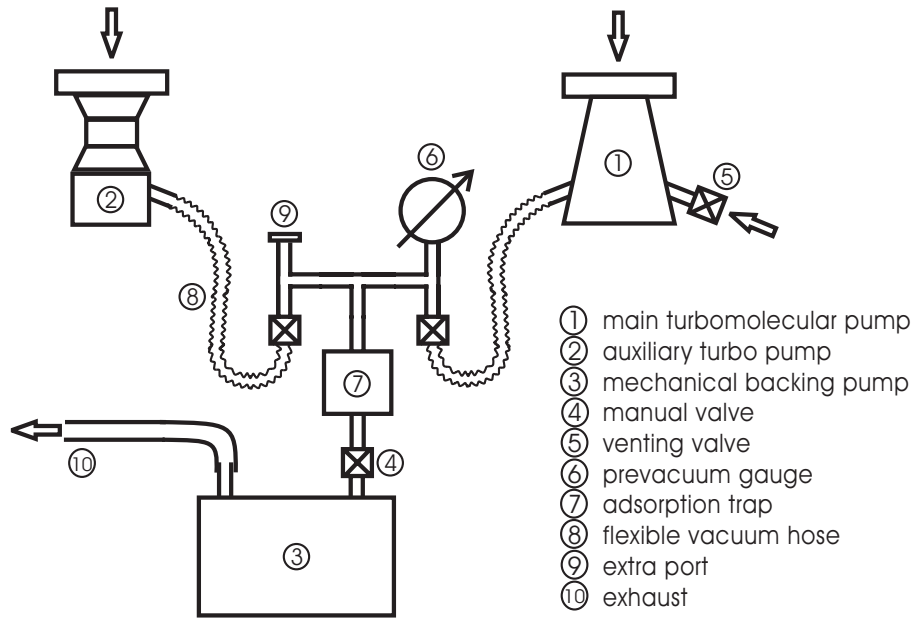


**Figure 3.1:** *Rough vacuum components*

1. Electric dispensers or a thermal oven provide atoms that are trapped in a *vapor cell trap* in MOT configuration. These precooled atoms can be transferred via a cold beam into a trap in a second chamber where a very clean vacuum is maintained avoiding the high losses in the vapor cell trap due to background pressure.
2. An oven produces an expanding thermal atomic cloud from which an atomic beam is formed by selecting atoms flying into some smaller solid angle. These atoms are then precooled longitudinally by chirped cooling or Zeeman cooling and finally captured in a MOT.

There are several reasons to choose option two for calcium: a vapor cell trap for calcium is more difficult to build than for alkali atoms since no dispensers exist so far for calcium due to its very low vapor pressure, see next paragraph. Another incentive to choose the second option is that the required length of the Zeeman slower is short compared to that in the more traditional experiments with alkali atoms. The cooling transition's shorter wavelength (here 423 nm vs. 780 nm in rubidium) presents a greater momentum transfer per photon and the shorter lifetime of the upper level in the cooling transition (here 5 ns vs. 29 ns in rubidium) increases the cycling rate and therefore the momentum transfer rate. This leads to a sevenfold shorter minimum slower length (see table 3.1 for a comparison between alkali and earth-alkali atoms). In summary, a Zeeman slower for calcium demands less space and experimental effort than its considerably larger and more electric power consuming counterparts in alkali experiments which have been studied extensively and which present a solid foundation for all cooling experiments.

Calcium has a very high melting temperature of 850°C compared to the alkali atoms, e.g.  $P_{melt,Rb} = 39^\circ\text{C}$  [76]. While those can be evaporated at moderate temperatures<sup>3</sup> it is

<sup>3</sup>e.g.  $P_{vap,Rb}(130^\circ\text{C}) = 10^{-3}$  torr [76]

	$^{23}\text{Na}$	$^{133}\text{Cs}$	$^{24}\text{Mg}$	$^{40}\text{Ca}$	unit
$\lambda_{\text{main}}$	589.0	852.1	285.2	422.6	nm
lifetime $\tau$	16	32	2.02	4.57	ns
recoil velocity $\Delta v$	2.29	0.35	5.84	2.36	cm/s
initial velocity $v_0$	800	300	1000	800	m/s
scattering events $N$	35	85.7	17.1	33.9	$\times 10^3$
min. stopping length $L_{\text{min}}$	45	82.3	3.46	12.4	cm

**Table 3.1:** *Laser cooling data [116], comparing alkali (Na,Cs) and earth-alkali (Mg,Ca) atoms:  $N$  is the number of photons needed for cooling starting from the velocity  $v_0$*

necessary to heat calcium to temperatures above 600°C to get sufficient evaporation from the metallic compound that is used in the oven. The vapor pressure of calcium is given in the range of  $10^{-5}$  to  $10^{-1}$  torr [76, pp. 2,12] as

$$\log p [\text{torr}] = -\frac{A}{T} + B + C \log T \simeq -\frac{A}{T} + B + DT \quad (3.1)$$

where  $A = 9388$ ,  $B = 10.796$ ,  $C = -0.6648$ ,  $D = -1.5308 \cdot 10^{-4}$ , and the temperature  $T$  is in Kelvin. In the range of 960°C to 1110°C the vapor pressure of calcium [122, p. D-213] is

$$\log_{10} p [\text{torr}] = -\frac{19325.1}{T} + 16.240 \quad (3.2)$$

Numerical values are given in table A.3.

The source chamber is a standard KF63-Tee whose symmetry axis is placed parallel to the tabletop and whose two opposing ports point into the vertical direction. A small extra KF16 port was added as an exit port for the atomic beam, just opposite to the horizontal port which contains the oven and its cooling shield. The chamber is pumped from below by a turbo-molecular pump (see appendix D) that can evacuate the complete vacuum system from a rough vacuum pressure of several mbar down to high vacuum condition below  $10^{-6}$ mbar. As vacuum gaskets we used viton o-ring seals at the source chamber as a convenient way to multiply and easily open this part of the system for recharging the oven with metallic calcium. The vibrations of the turbo-pump are largely decoupled from the rest of the vacuum system by two different vibration damping elements<sup>4</sup> in series between pump and chamber. They are vital to suppress the otherwise strong oscillations on the laser locks at the turbo pump drive frequency of 860 Hz. The top port of the main chamber is closed by a KF63 viewport for visual inspection and adjustment of the Zeeman slower beam.

The oven itself (see appendix C.5) is a stainless steel cylinder of 60 mm length and 20 mm diameter with 45 holes drilled in the front as oven exits. These channels are 10 mm long and 1 mm in diameter to yield a precollimated beam. The channel dimensions are determined by feasibility limits of mechanical engineering, see table B.6. A groove with 14 turns is cut into the steel cylinder to receive the heater wire. For this purpose we used a

<sup>4</sup>Vibration damper # 85425 by Leybold and model PM006 800-X by Pfeiffer, both with DN63 ISO-K flanges

heater<sup>5</sup> which can be used up to 1000°C. It consists of a central nickel-chromium (80/20) wire embedded in insulating mineral powder (MgO<sub>2</sub>) surrounded by a weldable cladding (Inconel). A special feature of this wire are the 50 cm long cold ends that allow to heat the one meter long heating section between them to high temperatures while keeping the connections at a lower and more convenient level. This is particularly useful since the electrical feedthroughs penetrating the vacuum chamber wall must not be heated to more than 400°C. As a connector between heater wire and feedthrough we chose a ceramic-metal type (CV10) with absolute maximum ratings of 550°C and 9 A which is sufficient since at  $T_{\text{oven}} = 700^\circ\text{C}$  we apply a current of 5 A corresponding to a flux of 5 Watt/cm<sup>2</sup>. The total resistance of the heater wire at room temperature is  $R = 12.5 \Omega$ .

The oven temperature is monitored with a type K thermo element<sup>6</sup> that was permanently fixed to the front end of the oven capsule. The inconel coating allowed to braze the element into the oven chamber flange. The temperatures range of the Chromel(+) Alumel(−) element is  $-200$  to  $+1000^\circ\text{C}$  with a tolerance of  $\pm 2.5^\circ\text{C}$  below  $333^\circ\text{C}$  and  $\pm 0.75\%$  above that.

The oven is fixed inside a copper heat shield by six screws with sharpened heads to minimize heat conduction to the shield which is just a copper tube with ID 30 mm and OD 38 mm. A copper tubing<sup>7</sup> is wound around the shield to cool it with tap water at room temperature.

Calcium is loaded into the oven cylinder through a lid on its face opposite to the oven exit. The size of the metallic pieces of calcium<sup>8</sup> filled into the oven should exceed the diameter of the exit channels yet maximize the filling ration of the very limited oven volume. The purity of the metallic sample is not critical — in any case the metal forms a layer of oxide during the oven filling period until vacuum conditions are restored. This oxide and other contaminants must be removed prior to an experiment with the atomic beam. For this purpose the oven is after pump-down separately heated to several hundred degrees Celsius for at least one afternoon. During this period the KF16 gate valve towards the Zeeman slower *must be closed* to avoid contamination of the main vacuum chamber.

## Power and cooling requirements

To determine the required heater power and the resulting cooling requirements for the copper heat shield we estimate the heat radiation of the source cylinder since this is here the dominant heat loss process. Heat conduction from the oven is greatly suppressed by the reduced contact area of sharpened screws and heat transfer by convection is negligible in the high vacuum environment. The surface area of the oven cylinder (length 40 mm,

---

<sup>5</sup>Thermocoax SEI 10/100:  $\varnothing$  1 mm, Inconel cladding (12% of diameter), Ni-Cr conductor (34% of diameter), heater length 1 m, *cold ends* 15 cm each, CV10 plug

<sup>6</sup>Thermocoax FKI 10/25, 41  $\mu\text{V}/^\circ\text{C}$

<sup>7</sup>ID 4 mm, OD 6 mm

<sup>8</sup>Calcium granules, redistilled, -16 mesh, purity 99.5% (metals basis), Alfa-Nr. 042917. Caustic and easily inflammable.

diameter 10 mm) is  $A = 14 \text{ cm}^2$ . The energy flux  $R$  from a perfect radiator is

$$R = \frac{\text{energy/sec}}{\text{surface area}} = \frac{c}{2} \int_0^{\infty} \rho(\nu, T) d\nu = 5.67 \cdot 10^{-8} T^4 [\text{W/m}^2], \quad (3.3)$$

and in our case the radiated power at  $T = 700^\circ\text{C}$  amounts to 72 Watt. Since the oven is not a black radiator, the absorption coefficient  $\alpha < 1$  and therefore the calculated value is an upper limit for the specific radiation and thus an upper limit for the necessary heater power. With the heater wire mentioned above this power can be generated by applying about 30 Volts.

One could be suspicious about the energy taken from the oven by the atoms in the beam. At 1000 Kelvin the atomic flux at the oven exit is on the order of  $10^{16}$  atoms/sec (see section 3.2). The energy loss rate  $R_{\text{kin}}$  due to leaving atoms equals the product of the particle flux times the kinetic energy carried away on average by each atom:

$$R_{\text{kin}} = 10^{16} \times 973 \cdot 1.4 \cdot 10^{-23} \text{ J s}^{-1} \simeq 10^{-4} \text{ W}. \quad (3.4)$$

Alas, this contribution is negligible. The final design of the oven cylinder and cooling shield is shown in figures C.5 and C.6.

## 3.2 The atomic beam

The following calculation will estimate the flux of atoms leaving the oven, entering the slower, leaving the slower and entering the MOT capture range. Several approximations and assumptions are necessary and will be pointed out during the calculation.

Generally, the atomic flux [102] through a circular hole with an area  $A_s$  is

$$Q_0 = \frac{1}{4} n \bar{v} A_s, \quad (3.5)$$

where  $n$  is the atomic density on the high pressure side, and  $\bar{v} = \sqrt{\frac{8k_B T}{\pi m}}$  is the mean atomic velocity in the oven at a given temperature  $T$ . More specifically the flux through an extended channel or tube with cross section  $A_s$ , radius  $r$ , and length  $l$  is

$$Q_0 = \frac{1}{\kappa} \frac{1}{4} n \bar{v} A_s, \quad (3.6)$$

where  $\frac{1}{\kappa} = \frac{8}{3} \left(\frac{r}{l}\right)$  for channels with  $l \gg r$ . Since the transfer from the interior to the exterior of our oven proceeds through 45 channels of 1 mm diameter and 10 mm length we get with  $\frac{1}{\kappa} = \frac{4}{30} \simeq 0.13$  while the total flux is just the summation over all channels.

The Maxwell-Boltzmann velocity distribution is known as

$$f(v) = \left(\frac{m}{2\pi k_B T}\right)^{3/2} \exp\left[-\frac{mv^2}{2k_B T}\right] = \left(\frac{1}{\pi v_0^2}\right)^{3/2} \exp\left[-\left(\frac{v}{v_0}\right)^2\right] \quad (3.7)$$

with  $v_0 = \sqrt{\frac{2k_B T}{m}}$  being the most probable velocity since it maximizes  $f(v)$ . Integrating over the radial coordinate we get the one-dimensional distribution of velocities

$$f(v) = \frac{4}{\sqrt{\pi} v_0} \left(\frac{v}{v_0}\right)^2 \exp\left[-\left(\frac{v}{v_0}\right)^2\right]. \quad (3.8)$$

The mean velocity is defined as the first moment of the velocity distribution:

$$\bar{v} = \int_0^\infty v f(v) dv = \frac{2v_0}{\sqrt{\pi}}. \quad (3.9)$$

The velocity distribution in an atomic beam on the other hand is slightly different:

$$g(v) = \frac{2}{v_0} \left(\frac{v}{v_0}\right)^3 \exp\left[-\left(\frac{v}{v_0}\right)^2\right]. \quad (3.10)$$

The mean velocity in this case is given as

$$\bar{v} = \int_0^\infty v g(v) dv = \frac{3}{4} \sqrt{\pi} v_0. \quad (3.11)$$

To calculate the fraction of atoms in the beam below a certain velocity  $v_r$  it is valuable to keep in mind the relation

$$\int_0^{v_r} g(v) dv = \left(\frac{v_r}{v_0}\right)^4 \quad (3.12)$$

which is valid as long as  $v_r \ll \bar{v}$ . Both distributions  $f(v)$  and  $g(v)$  are normalized and thus follow

$$\int_0^\infty f(v) d^3v = \int_0^\infty f(v) dv = \int_0^\infty g(v) dv = 1. \quad (3.13)$$

The velocity distribution can be used to calculate the rate of transmitted atoms through a circular tube of radius  $r$  and length  $l$ . Defining a maximum free opening angle  $\theta_{max} = r/l$  we get

$$Q = \rho \frac{A}{2} 2\pi \int_0^\infty f(v) v^3 dv \int_0^{\theta_{max}} \sin \theta d\theta \quad (3.14)$$

$$= \rho \frac{A}{2} 2\pi \frac{v_0}{2\pi^{3/2}} \int_0^\infty g(v) dv \int_0^{r/l} \sin \theta d\theta \quad (3.15)$$

$$\cong \rho A \frac{v_0}{2\sqrt{\pi}} \frac{1}{2} \left(\frac{r}{l}\right)^2 \quad (3.16)$$

$$= \frac{1}{4\sqrt{\pi} \rho A v_0} \left(\frac{r}{l}\right)^2 \quad (3.17)$$

$$(3.18)$$

where  $\rho$  is the atomic density which can be derived from the ideal gas equation  $pV = NRT$  as  $\rho = N/V = \frac{p}{k_B T}$ . One can directly ask how many of the atoms leaving the oven through

$T$	[°C]	500	600	700	800
$Q_{\text{opt}}$	[atoms/sec]	$7.4 \cdot 10^{12}$	$7.9 \cdot 10^{12}$	$8.3 \cdot 10^{12}$	$8.7 \cdot 10^{12}$

**Table 3.2:** *Optimal atomic flux into the MOT region as calculated in the Lucas description*

one channel will contribute to the flux into the MOT-region: the flux from the oven into the solid angle of the MOT as seen from the source is  $(R/L)^2 \approx 1/2500$  with  $R = 10$  mm and  $L = 500$  mm while the flux through one channel scales with  $(r/l)^2 \approx 1/400$ . Their ratio 1/6 shows that only every sixth atom leaving the oven will potentially contribute to the trap population due to the distance between trap and oven required for deceleration, which we learned from purely geometrical considerations.

One mole of  $^{40}\text{Ca}$  contains  $6 \cdot 10^{23}$  atoms weighing 40 g, therefore one oven filling of about 1 g corresponds to  $10^{22}$  atoms. Since the atomic flux from the oven is estimated to be on the order of  $10^{12}$  atoms per second at reasonable operating temperatures, the calcium reservoir should last for a sufficiently long time.

An optimization of the atomic flux is possible with the so-called *Lucas description* which is explained below. A prerequisite is that the mean free path between collisions ranges between the tube diameter  $d$  and the length  $l$ . In this description the pressure behind the tube is  $P = P_{\text{R}}/(l\sigma)$  (in torr), the beam width  $H = H_{\text{R}} \left(\frac{d}{l}\right)$  (in degrees), the gas flux  $I = \sqrt{\frac{T}{295 M}} \frac{d^2 I_{\text{R}}}{l\sigma^2}$  (in  $\frac{\text{atoms}}{\text{sec}\cdot\text{sr}}$ ), and the throughput  $Q = \sqrt{\frac{T}{295 M}} \frac{d^3 Q_{\text{R}}}{l^2 \sigma^2}$  (in  $\frac{\text{atoms}}{\text{sec}}$ ). The normalization parameters  $H_{\text{R}}$ ,  $I_{\text{R}}$  and  $Q_{\text{R}}$  depend on the normalized pressure  $P_{\text{R}}$  as  $H_{\text{R}} = 2.48 \cdot 10^2 \sqrt{P_{\text{R}}}$ ,  $I_{\text{R}} = 1.69 \cdot 10^{20} \sqrt{P_{\text{R}}}$  and  $Q_{\text{R}} = 2.16 \cdot 10^{21} \sqrt{P_{\text{R}}}$ . In the above equations  $T$  is the temperature [K],  $M$  the molecular weight [g],  $\sigma$  the molecular diameter [ $\text{\AA}$ ] and  $l$  and  $d$  the tube dimensions [cm]. The optimum gas flux is given for  $P_{\text{R}} \rightarrow 1$  and

$$I_{\text{opt}} = 6.7 \cdot 10^{17} \sqrt{\frac{T}{295 M}} \frac{H d}{\sigma^2}. \quad (3.19)$$

Using  $d = 0.5$  mm and  $d/l = 1/10$  we get  $H = 24.8^\circ$  and the optimal flux of atoms into the MOT region  $Q_{\text{opt}} = 2.659 \cdot 10^{11} \sqrt{T}$  atoms/sec is shown in table 3.2. We can see that its variation is small across the temperature region of interest and can be assumed constant at about  $8 \cdot 10^{12}$  atoms/sec.

### 3.3 Between chambers

On their way from the oven to the main experimental chamber the atoms in the thermal beam pass three vacuum parts: a small gate valve, the Zeeman slower tube, and the transverse cooling section.

The DNKF16 gate valve is directly attached to the oven chamber exit flange and allows to vent the oven chamber while still keeping the rest of the vacuum system evacuated. This valve is always closed for security unless the experiment is run to prohibit venting of the main chamber in case of a turbo pump malfunction or a power shortage. Closing this valve during laser maintenance while the oven is hot avoids unnecessary Ca deposition on the slower beam window.



The Zeeman slower tube with 16 mm inner diameter and 27 cm length is surrounded by the Zeeman slower coil described in chapter 5. A photograph of the central part of the ultra-high vacuum system is shown in figure 3.2. The picture was taken early in the construction, so the configuration has changed to now include a Zeeman slower window section and different viewports at the transverse cooling section.

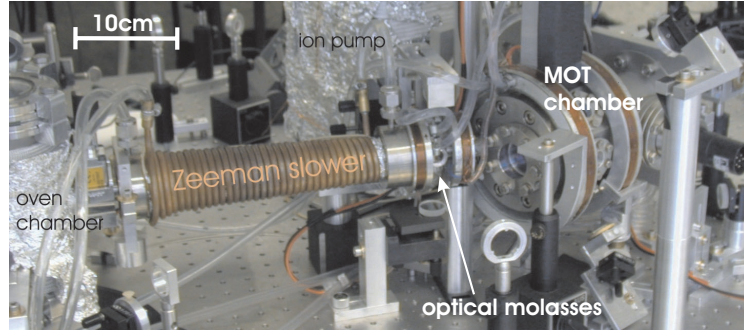


**Figure 3.2:** Photograph of the UHV chamber. From left to right: oven chamber, KF16 gate valve, Zeeman slower magnet, transverse cooling section, main chamber.

The transverse cooling section offers optical access to the atomic beam through four windows, two on a horizontal and two on a vertical axis, where both axes are perpendicular to the beam propagation axis. In a first version as shown in figure 3.2 we used a stainless steel cube (40 mm side length) with two opposing CF16 flanges on short tubes for the vacuum connections. The windows were sealed with indium wire (see end of section 3.4.2). In the current version four commercial AR-coated CF16 viewports occupy four ports of a standard CF16 double cross. This change facilitates bakeout, minimizes vacuum leaks at the windows and at welding joints of the cube, and it increases the mechanical stability while only minor compromises had to be accepted such as a slightly degraded optical quality and increased size. Both the entrance and the exit flange for the beam are surrounded by a magnetic coil: the first produces a field axially reversed to the slower coil field to pull the field below zero and then decouple the atoms from the slowing process. The second coil at the transverse cooling section exit reduces and compensates the stray field in the trap region resulting from the first two coils.

The geometrical dimensions of the connection between oven and main chamber lead to a small conductivity of only

$$C = 12 \frac{(1.6)^3}{40} \text{ l/s} = 1.23 \text{ l/s}. \quad (3.20)$$

This value shows that the turbo pump contributes only little to the pumping speed experienced in the main chamber. When a pressure of  $10^{-8}$  mbar is reached in the main chamber by only operating the oven chamber turbo pump, then we know that the pressure in the oven chamber must be below  $10^{-10}$  mbar when the oven is not in operation. This can be seen by using the continuity relation  $S_1 P_1 = S_2 P_2$  and the vacuum master equation which is described in section 3.4.4 as equation (3.21).

## 3.4 The main chamber

### 3.4.1 General shape and attached components

The central part of this chamber is a standing octagon with DN 63 CF flanges on both vertical faces and eight ports radially on the flat sides, see section 3.4.2. One vertical face is closed by a special flange that contains an off-center viewport and the entrance for the atomic beam. The other face attaches to a cylinder that itself is terminated by a large viewport flange and which features several ports: vertically upwards are two DN 35 CF ports, one spare and one used by the pressure gauge<sup>9</sup>. A small DN 16 CF port used for electrical feedthroughs points downwards, and a DN 40 CF port to the side connects the main chamber with a large ion pump via a DN 35 CF gate valve and a CF 35 to CF 63 adapter piece (see section 3.4.4). The pumping speed in the main chamber is considerably reduced from the pumping speed at the mouth of the ion pump due to the valve because it imposes a diameter reduction and length increase of the tubing connection to the pump. The valve is necessary to protect the pump in times of prolonged venting during installations in the main chamber. Opposite to the atomic beam entrance a DN 40 CF tube connection attaches to the slower window section, see section 3.4.3.

In choosing the chamber wall material special care was taken to avoid unnecessary magnetic stray fields induced by the chamber walls themselves. The different kinds of stainless steel and their application in the construction of the vacuum system are summarized in table 3.3.

AISI	DIN	$\mu$	application
316LN	1.4429 “ESU”	1.001	main chamber
304	1.4404, 1.4435	1.03	all tubes, sheets
304L	1.4301	1.03	flanges, other fittings
	1.4571 “NIRO”		V4A, not used

**Table 3.3:** *Magnetizability of stainless steel materials*

### 3.4.2 Viewports

There are 11 viewports in the main chamber giving optical access to the experiment. Eight small ports with 16 mm free diameter are equally distributed over the octagon chamber surface in a plane perpendicular to the optical table. Of these both MOT’s laser beams use four ports each. The windows on the endcaps of the cylindric chamber are shared by both MOT’s as third axis. One of these windows has only 50 mm diameter and sits off-center, while the opposite viewport with its 60 mm diameter optimally uses the space on the DN 63 CF flange. This was necessary to allow for the atomic beam to enter the main chamber. The angle between the beam axis and the radial symmetry axis of the hexagonal chamber is 30°. Opposite to the atomic beam entrance an extruding tube prolongs the

<sup>9</sup>ionization vacuum gauge ITR 100, Leybold

chamber along the beam axis towards a viewport which is used by the Zeeman slowing laser.

Commercial vacuum viewports are sufficient for visual inspections of the chamber interior, but they are usually far from the optical quality desired in laser cooling experiments. To avoid wavefront distortions by uneven surfaces and bulk material impurities we decided to use quartz substrates with high optical perfection instead. Unfortunately this gain in optical performance leaves one with more difficulties when seen from the vacuum engineering point of view. To seal the ultra-high vacuum (UHV) chamber at the viewports we first used so-called Helicoflex<sup>®</sup> gaskets<sup>10</sup>, toroidal aluminum rings with an outer cut and an inner spring that presses the softer outer shell onto the two contacting surfaces establishing the vacuum seal. These gaskets turned out to be truly useful only at large windows of min. 60 mm diameter since at smaller viewports the necessarily small number of compressing screws cannot distribute pressure evenly enough to avoid leaks. More leaks are introduced if the metal chamber surface on which the gasket rests is not machined on a lathe and subsequently polished to perfection with a polishing wheel — if milling is used even an apparently perfect surface shows leaks due to microgrooves that cross the gaskets' contact line.

Suitable viewport substrate materials are BK7 for visible/near-IR light (400–900 nm) and quartz<sup>11</sup> for far-IR (1978 nm). All windows were given a wavelength optimized antireflection (AR) coating on both faces. A mask restricted the coating area to an inner circle to keep the gasket contact area on the substrates uncoated since it had turned out that a coating can get brittle due to the high local pressure under a gasket, and vacuum leaks can occur. The dimensions of the window substrates, suitable gaskets, and the coating masks

substrate OD	mask OD	ID×OD×Ø	Δd	Ref.-Nr.
25	18	18.5 × 23.7 × 2.6	0.8	H15014
50	37	37.6 × 44.2 × 3.3	0.9	H15027
60	46	47.9 × 56.9 × 4.5	1.0	H15031

**Table 3.4:** *Viewport substrate, Helicoflex gasket and coating mask dimensions (in mm)*

are shown in table 3.4, where ID (OD) is the inner (outer) diameter, Ø is the diameter of the toroidal cross-section, and Δd the change in thickness under compression.

Although the Helicoflex gaskets remained tight after a single bake-out, it proved to be impossible to keep the smaller diameter gaskets since they presented unmanageable leaks. The alternative gaskets used now are indium seals where sealing rings were prepared from wire<sup>12</sup> with slanted cut ends. These seals allow to reach the 10<sup>-9</sup> mbar level but prohibit further improvement. The main reason is the low melting point of indium (≈ 170°C) that helps to secure a good seal at room temperature but abolishes baking of the chamber.

The windows on the transverse cooling section are also sealed with indium. The dimensions have a concentric symmetry: a central 14 mm hole in the chamber for optical

<sup>10</sup>Type HN100 series 15000, aluminum / Nimonic 90, Deutsche Carbone AG

<sup>11</sup>see [66] for the index of refraction of quartz

<sup>12</sup>Indium wire Puratronic 99.9985%, diameter 1 mm, Alfa 944349

access, 15 mm outer diameter of the AR-coating on the substrates, 19 mm substrate OD, and the indium ring rests at a 17 mm diameter.

### 3.4.3 Zeeman slower window section

In the first version of our vacuum system, the Zeeman slowing laser was sent into the chamber through the 50 mm main chamber window onto a mirror inside the vacuum chamber and deflected into the slower magnet tube. The dielectric mirror was heated by a flat round heater element<sup>13</sup> between the mirror substrate and the steel mirror mount to about 150°C to discourage deposition of calcium. Although this temperature is well below the Ca vapor pressure, it is possible to prolong the duration until the mirror gets coated with Ca, and its reflectivity is reduced from 99.9% to useless  $\sim 50\%$ . It is not possible to remove the calcium coating using a strong focused laser beam — even with only 1 W at 532 nm (unfocused) the pressure in the chamber raises within seconds from  $10^{-8}$  mbar to more than  $10^{-7}$  mbar since the heater and the mirror mount heat up excessively before any calcium is ablated. Maintaining the small heater with its delicate connections and the prospect to frequently open the main vacuum chamber to clean the mirror turned out to pose serious experimental difficulties. Therefore, we decided to replace the mirror and use a different approach instead.

Continuing its way past the trap region the atomic beam now enters a tube that finally ends in a commercial DN35CF window<sup>14</sup>. The distance between trap and window is about 36 cm, large enough to reduce the calcium deposition by simple geometrical scaling such that the window has to be cleaned or replaced only every few months. The calcium deposition rate is further reduced by constantly heating the window to approx. 100°C. Once a monolayer of calcium has formed the deposition rate obviously increases greatly since then only few hours of beam operation are enough to form a calcium layer thick enough to reflect the slowing laser so strongly that the slowing and trapping process breaks down. To facilitate the window replacement and reduce the experiment down-time a DN35CF gate valve between trap and window allows to separate the slower window section from the rest of the vacuum system. A small auxiliary turbo pump<sup>15</sup> is permanently attached to this section via an all-metal right angle valve to pump down again from atmosphere after window replacement. Removing the calcium deposition on the window from outside using a focussed 10 W green light beam was not feasible: the calcium layer evaporated due to strong absorption but also destroyed the inner AR coating rendering the window unusable although the laser did not destroy the AR coating at positions without calcium.

### 3.4.4 Main chamber ion pump

To address the question about the level of vacuum that can be expected to be achieved with the applied pumps we will look at the pumping speed at the trap site in the main chamber

---

<sup>13</sup>Kapton heater element HK5539 R10.2 L12, MINCO,  $\varnothing$  19.8 mm,  $10.4 \Omega$  at 20°C, connected to 5V line via  $18.7 \Omega$  shunt,  $I = 189$  mA,  $P \approx 0.5$  W

<sup>14</sup>Kodial viewport, Vacuum Generators # ZVPZ38

<sup>15</sup>TurboVac 50, Leybold

due to the ion pump (see appendix D). A few quantities necessary for the description of gas flow regimes are introduced [90].

The throughput — which is the mass flow rate through some vacuum connection — is given as  $Q = C(P_1 - P_2)$  where  $P_1$  and  $P_2$  are the pressures at both ends of the connection ( $P_1 > P_2$ ) with a conductance  $C$ , which is a geometrical constant. The throughput is also  $Q = P \cdot S$ , usually in [mbar l/s], where  $S = dV/dt$  [l/s] is the pumping speed. Mathematically conductances in networks of vacuum connections behave like capacities in electrical circuits (e.g.  $C_{\text{parallel}} = C_1 + C_2 + \dots$ ). The vacuum master equation derived from above definitions is

$$\frac{1}{S} = \frac{1}{S_P} + \frac{1}{C} \quad (3.21)$$

where  $S$  is the pumping speed at the point of interest, e.g. the atomic trap,  $S_P$  the pumping speed at the pump mouth, and  $C$  the total conductance between both points. The conductance for air at 20°C of a straight tube with diameter  $D$  [cm] and length  $L$  [cm] depends on the flow regime: in viscous flow  $C$  [l/s] =  $180 D^4/L P_{\text{avg}}$  where  $P_{\text{avg}}$  [torr] is the pressure averaged over the tube length. However, in the molecular flow regime the conductance of the same tube is  $C$  [l/s] =  $12 D^3/L$ .

The total conductance between the main chamber and the ion pump is  $C = 54.9$  l/s since the conductance of the DN35CF gate valve is 131.7 l/s and the reducer piece conducts at  $C_{\text{red}} = 12 \cdot (3.8)^3/7$  l/s. With a pumping speed at the ion pump of  $S_P = 50$  l/s for nitrogen we get a pumping speed  $S = 26.2$  l/s in the main chamber using (3.21). For comparison, the resulting pumping speed for other geometrically allowed options are given: using an elbow valve ( $C_{\text{elbow}} = 35$  l/s) with a reducing CF63-CF35 flange<sup>16</sup> ( $C = 274.4$  l/s) would yield  $C = 31.0$  l/s and  $S = 19.2$  l/s. Using the gate valve with a section of straight tubing<sup>17</sup> ( $C = 52.3$  l/s) and the reducing flange would result in  $C = 32.9$  l/s and  $S = 19.9$  l/s.

A comparison of this result and the value calculated in (3.20) shows that the contribution of the turbo pump to the pumping speed in the main chamber is negligible.

## 3.5 Baking

Although much time was spent in the effort to improve the vacuum purity by several techniques of which the heat treatment is the most important one, I will only shortly sketch the process of *baking* the system which is necessary every time the vacuum chamber is vented and opened to atmosphere.

All optical components close to the vacuum chamber are removed. Glass fibre insulated heater tapes are wrapped around the whole chamber excluding the turbo pump, the vacuum gauge, and all indium sealed ports. Sharp edges are covered with aluminum sheet which is also used as an outer layer around the heater tapes to distribute the heat as evenly as possible. The heaters are connected to temperature controls which use sensors placed close to the heater tapes. The temperature of all heaters is changed only slowly — e.g. heating from 20°C to 200°C requires at least one hour — to prohibit cracks in viewports or other

---

<sup>16</sup>thickness 2.4 cm

<sup>17</sup>length 12.6 cm

vacuum failure at weak spots like the Zeeman slower tube due to mechanical stress exerted by the fixtures. The large port with its indium seal can be cautiously heated to 120°C using a blackened cover and an infrared heater bulb.

Three points in the system can be heated immediately without additional installations: the Zeeman slower tube, the high vacuum gauge, and obviously the oven. Running current through the Zeeman slower coil will heat the vacuum tube inside, but since the coil thickness is not constant along the tube, the heat will not be distributed uniformly. Therefore, it is advisable to heat this part in a more controlled manner like all others with externally wrapped heater tapes. The vacuum gauge surface is cleaned from depositions by activating the Degas option that temporarily activates a built-in heater near the gauge wires. The oven finally should always run for some hours after venting at high temperature with the KF16 gate valve closed to get rid of dirt and trapped gases in the calcium grains. This will avoid contamination of the main vacuum chamber.

### 3.6 Vacuum quality assessment

There are several measurements that give information about the level of vacuum that has been achieved and that help to minimize leaks and optimize overall vacuum performance. The most obvious are the readings of the pressure gauges<sup>18</sup> in the foreline and the main vacuum chamber. To improve the pressure once it has settled at some level one needs to detect possible leaks that can often be closed by further tightening of certain flange screws. These leaks to the vacuum chamber exterior were analyzed with a helium leak detector (see appendix D). Two modes are possible: either the vacuum system is pressurized with helium above atmospheric pressure and a sniffing detector allows to find the positions where helium seeps through the flanges. Alternatively the detector directly pumps the vacuum system and measures the amount of helium inside while small amounts of helium are flushed onto the chamber from outside. The second method was chosen since the positional detectability of leaks is better, and considerably less helium is used which is of particular interest when the process is repeated after every change to the vacuum system.

Internally the leak detector uses a counter-current method to increase the sensitivity to helium in the main vacuum line: the internal roughing pump backs the main pump of the vacuum system and at the same time an internal turbo pump (TP) that pumps a mass spectrometer (MS) included in the leak detector.

This spectrometer measures the partial helium pressure mainly due to helium molecules originating from the main vacuum chamber and passing through the internal TP *against* its pumping direction, therefore the term counter-current is applied. The displayed leak rate  $Q_A$  [mbar l/s] is proportional to the measured partial pressure of helium

$$P_{MS}(\text{He}) = \frac{Q(\text{He})}{K_{TP}(\text{He}) \cdot S_V(\text{He})}, \quad (3.22)$$

where  $K_{TP}(\text{He})$  is the inverse pumping speed of the internal TP,  $S_V(\text{He})$  is the rough vacuum pumping speed, and  $Q(\text{He})$  is the actual helium leak rate in the chamber.

---

<sup>18</sup>see pages 26 and 34

What is the significance of, for example, a 1 mbar l/s leak? It means that the pressure in a one liter vacuum container increases in one second by 1 mbar.

If possible, every single vacuum component was leak checked by itself. The test results for the gate valve between the oven chamber and the Zeeman slower are shown in table 3.5. All other vacuum parts of the main chamber were tested down to the  $10^{-9}$  mbar l/s level.

valve status	tested spot	He leak rate [mbar l/s]
closed, one side vented	valve plate	$< 10^{-10}$
	actuator base	$5 \cdot 10^{-10}$
opened, both sides evacuated	plate gaskets	$< 10^{-10}$
	actuator base	$5 \cdot 10^{-10}$
	stem guide	$< 10^{-10}$
moving valve stem	stem guide	$< 10^{-10}$

**Table 3.5:** Leak test data for the KF16 gate valve

Testing the complete main UHV chamber at first we found leaks on the  $10^{-4}$  mbar l/s level, but by tightening window by window about  $5 \cdot 10^{-9}$  mbar l/s were reached. Further analysis of the rest leak was impossible since the test setup saturated with helium too fast at this low leak level.

# Chapter 4

## Sources of light

*The essential elements of a laser device are (i) a laser medium,  
(ii) a pumping process to excite this medium,  
and (iii) suitable optical feedback elements that allow a beam of radiation  
to bounce back and forth repeatedly through the laser medium.*  
based on Siegman [110, p.2]

The following chapter presents the various laser light sources applied to the experiment and how these light fields can be detected.

### 4.1 Resonators

It's beyond the scope of this work to give a full introduction to the theory of laser resonators, but since considerable time and effort was invested to create several laser systems I will at least present some general ideas to develop the terminology used in the following sections and point to the appropriate literature along the way.

#### 4.1.1 Theoretical description

A Gaussian light beam can be described (see [70]) as a travelling wave  $u = \Psi(x, y, z) \cdot e^{-ikz}$  that follows the homogenous wave equation  $\Delta u + k^2 u = 0$ . Neglecting  $\frac{\partial^2 \Psi}{\partial z^2}$  we get the second order differential equation

$$\frac{\partial^2 \Psi}{\partial x^2} + \frac{\partial^2 \Psi}{\partial y^2} - 2ik \frac{\partial \Psi}{\partial z} = 0, \quad (4.1)$$

which can be solved using the ansatz

$$\Psi = e^{-i\left(P + \frac{kr^2}{2q}\right)}, \quad (4.2)$$

where  $P = P(z)$  is the complex phase shift,  $r^2 = x^2 + y^2$ , and  $q = q(z)$  is the complex beam parameter. The beam parameter  $q(z)$  combines the experimentally accessible parameters radius of curvature  $R(z)$  and beam radius  $w(z)$  as

$$\frac{1}{q} = \frac{1}{R} - i \frac{\lambda}{\pi w^2}. \quad (4.3)$$



In a focus —also called the beam waist — the wavefront is plane and  $1/R = 0$ , hence the beam parameter there is  $q_0 = i\frac{\pi w_0^2}{\lambda} = i z_R$ , where we defined the Rayleigh range  $z_R$  and where  $w_0 = w(z = 0)$  since we can arbitrarily decide to place the origin of the  $z$ -axis into the beam focus. A beam parameter away from the focus is simply  $q(z) = q_0 + z = z + i z_R$ , and from this  $w$  and  $R$  can be expressed in terms of their values in the focus:

$$w(z) = w_0 \sqrt{1 + \left(\frac{\lambda z}{\pi w_0^2}\right)^2} = w_0 \sqrt{1 + \left(\frac{z}{z_R}\right)^2} \quad \text{and} \quad R(z) = z \sqrt{1 + \left(\frac{z_R}{z}\right)^2}. \quad (4.4)$$

A Gaussian intensity distribution is defined by  $I(r) = I_0 e^{-2r^2/w^2} = \frac{2P}{\pi w_0^2} e^{-2r^2/w^2}$  where  $P$  is the total power in the beam and  $I_0$  the on-axis intensity. The values  $w_0$  and  $w(z)$  are then the radii of  $1/e^2$ -irradiance at the focus and at a distance  $z$  from the focus, which itself is the plane where the wavefront is flat. In the far field, where  $z \rightarrow \infty$ , we find the asymptotes  $R \rightarrow z$  and  $w(z) \rightarrow \frac{\lambda z}{\pi w_0}$ , which form a cone with radius  $\theta = \frac{w(z)}{z} = \frac{\lambda}{\pi w_0}$ .

In *paraxial optics* it is assumed that the angle between the propagation direction of a light beam and the symmetry axis of the optical system is small. Then the light beam is described at every position along its path by a two-component vector  $\xi$  containing the transverse distance from the central line of symmetry and the angle between this line and the direction of propagation. This vector is transformed along the beam by optical elements like lenses and mirrors or just free space. Any such transformation can be mathematically expressed as element-specific matrices (see table B.7 and [70] for more) acting upon the light ray vector  $\xi$ . Multiple subsequent elements correspond to a multiplication of matrices from the left — for an example, see equation (4.6).

The propagation of a *Gaussian beam* is completely described by the transformation of the beam parameter  $q$  according to the so-called *ABCD-law* (see e.g. [117])

$$q_2 = \frac{A q_1 + B}{C q_1 + D} \quad \text{or} \quad \frac{1}{q_2} = \frac{C + D/q_1}{A + B/q_1} \quad (4.5)$$

where the letters  $A$  through  $D$  represent the four matrix elements in the ray vector transformation matrix  $M = \begin{pmatrix} A & B \\ C & D \end{pmatrix}$ .

### 4.1.2 Stability of resonators

Any resonator can be described as an infinite series of optical elements that appear periodically along the light path. To characterize a resonator it is then sufficient to describe all elements that the light beam passes during one cycle through the resonator. Since the effect of a curved mirror on the beam properties is comparable to that of a lens and since a plane mirror does not change anything but the direction of propagation, most resonators can be described in an equivalence picture where only lenses are used as shown in figure 4.1. The complete transfer matrix of the “resonator” in figure 4.1 is given as

$$M = \begin{pmatrix} 1 & -1/f \\ 0 & 1 \end{pmatrix} \begin{pmatrix} 1 & 0 \\ L_1 & 1 \end{pmatrix} \begin{pmatrix} 1 & -1/f \\ 0 & 1 \end{pmatrix} \begin{pmatrix} 1 & 0 \\ L_2 & 1 \end{pmatrix}. \quad (4.6)$$

A specific resonator like the bow-tie resonator<sup>1</sup> in figure 4.2 can now easily be described as

<sup>1</sup>this kind of resonator is used as an enhancement cavity for the frequency doubler

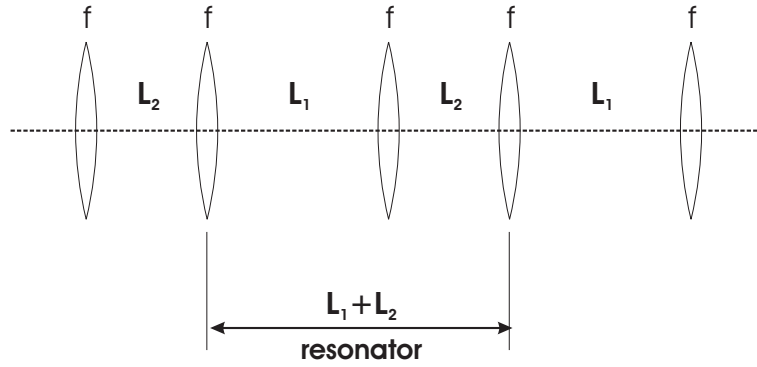


Figure 4.1: *Equivalence picture*

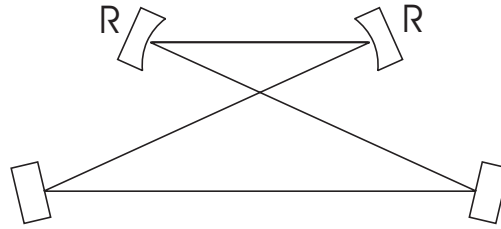


Figure 4.2: *Bow-tie resonator*

$$M = \begin{pmatrix} 1 & -2/R \\ 0 & 1 \end{pmatrix} \begin{pmatrix} 1 & 0 \\ L_1 & 1 \end{pmatrix} \begin{pmatrix} 1 & -2/R \\ 0 & 1 \end{pmatrix} \begin{pmatrix} 1 & 0 \\ L_2 & 1 \end{pmatrix} \quad (4.7)$$

$$= \begin{pmatrix} g_1 g_2 + g_2 - 1 & -\frac{2}{R}(g_1 + 1) \\ \frac{R}{2}(1 - g_1 g_2) & g_1 \end{pmatrix}, \quad (4.8)$$

where we have substituted  $f$  for the focal length of a curved mirror  $f = R/2$  and introduced the dimensionless variables  $g_{1,2} = 1 - 2L_{1,2}/R$  that express the relation of mirror distances  $L_{1,2}$  and mirror curvatures  $R$  ( $R_1 = R_2$ ). The equality  $\det M = 1$  is valid for all matrices describing resonator elements. Now the resonator stability can be analyzed by solving the eigenvalue equation  $M\xi = \lambda\xi$ . The solutions for the eigenvalues are  $\lambda_{\pm} = m/2 \pm \sqrt{m^2/4 - 1}$  with  $m = g_1 + g_2 + g_1 g_2 - 1$ .

A resonator is only stable for  $|\frac{m}{2}| \leq 1$ , thus  $|g_1 + g_2 + g_1 g_2 - 1| \leq 2$ . Two cases are possible:

1.  $(g_1 + g_2 + g_1 g_2 - 1) \geq 0 \implies 1 \leq g_1 + g_2 + g_1 g_2 \leq 3$
2.  $(g_1 + g_2 + g_1 g_2 - 1) < 0 \implies 1 \geq g_1 + g_2 + g_1 g_2 \geq -1$

Both together combine to  $-1 \leq g_1 + g_2 + g_1 g_2 \leq 3$ . The regions of stability are visualized as shaded areas in graph 4.3 where  $g_1$  and  $g_2$  are plotted against each other. The diagonal through this plot ( $g_1 = g_2$ ) marks three noteworthy points where it intersects the boundaries of the stable region:

- (1)  $L_1 = L_2 = 0$
- (2)  $L_1 = L_2 = R$
- (3)  $L_1 = L_2 = 2R$

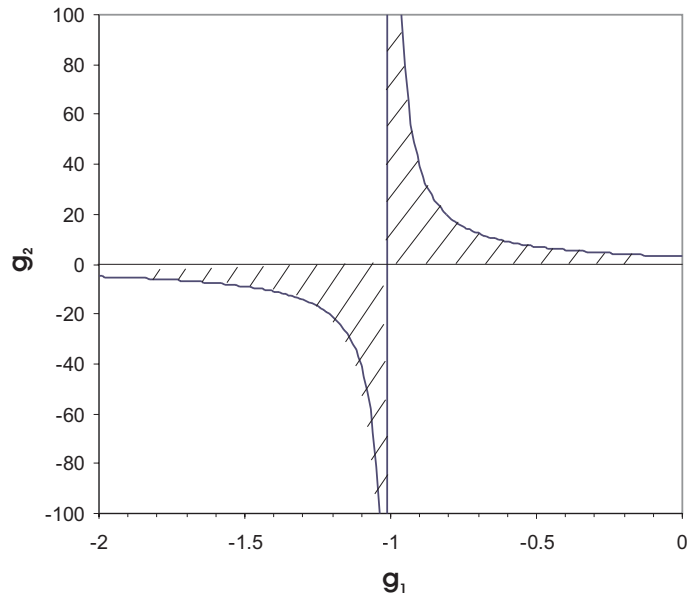


**Figure 4.3:** Resonator stability plot

Case (2) is called the *confocal resonator* and case (3) the *concentric resonator*.

### 4.1.3 Mode matching of resonators

When two optical resonators are connected it is necessary to match their electro-magnetic field modes in order to maximize the transmission through the entire system on resonance. The output mode of a resonator is described by the beam parameter  $q$ . Therefore, matching modes means finding suitable optical elements that transform the first resonator's  $q_1$  such that it matches the second resonator's  $q_2$ .

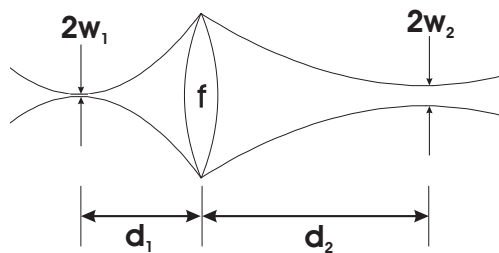


**Figure 4.4:** Illustration of mode matching with a single lens

In the most simple optical system with only one lens (see figure 4.4) there are three degrees of freedom, which are the distances from the lens to the resonator foci and the focal length  $f$  of the lens<sup>2</sup>. The Gaussian beam at the foci is described by the beam parameters

<sup>2</sup>In the more restricted case of a fixed distance between resonators — e.g. when both resonators have

$q_{1,2} = i \frac{\pi w_{1,2}^2}{\lambda}$ . Matching  $q_2$  and the propagated  $q'_1$  leads to the conditions

$$\frac{d_1 - f}{d_2 - f} = \left( \frac{w_1}{w_2} \right)^2 \quad (4.9)$$

$$\text{and} \quad (d_1 - f)(d_2 - f) = f^2 - f_0^2 \quad (4.10)$$

with  $f_0 = \pi w_1 w_2 / \lambda$ . For a given lens and known resonator foci the required distances are then

$$d_1 = f + \frac{w_1}{w_2} \sqrt{f^2 - f_0^2} \quad (4.11)$$

$$d_2 = f + \frac{w_2}{w_1} \sqrt{f^2 - f_0^2} \quad (4.12)$$

One lens is not always sufficient to achieve a perfect match. Often the beams are astigmatic, so the matching condition (4.9) has to apply for both transverse directions. This additional difficulty is most easily overcome by using two separate sets of cylindrical lenses. This decouples the transverse conditions but seriously increases the number of lenses and adjustments. On the other hand, even using only one spherical lens, a compromise close to optimal mode matching can be found. Table 4.3 lists resonator beam parameters that had to be matched. The Ti:sapphire resonator was coupled to the KNbO<sub>3</sub> resonator by an  $f = 150$  mm lens at a distance of 31.5 mm from the Ti:sapphire-outcoupler and at 52.5 mm from the incoupling mirror of the KNbO<sub>3</sub> resonator. This resulted in about 65% incoupling efficiency which means that the reflectance dropped from 100% away from resonance to 35% on resonance.

## 4.2 Titanium sapphire laser

A titanium sapphire (Ti:Al<sub>2</sub>O<sub>3</sub>) laser is a solid state laser in which a titanium doped sapphire crystal inside an appropriate resonator is optically pumped by an external green pump laser. Usually high-power ( $P > 20$  W) gas lasers like argon-ion lasers were applied as pump sources, now more and more replaced by diode laser pumped frequency doubled solid state lasers that consume considerably less electrical power and cooling water (see appendix 4.2.3). Ti:sapphire lasers offer radiation over a wide power and spectral range: the emission wavelength can be adjusted in the range of 780 nm to 860 nm by tuning the intracavity etalons. This range is mainly limited by the dielectric mirror coatings whose reflectivity degrades outside this part of the spectrum. Since the effect of the etalons is to force the laser to run at some specific wavelength by introducing intracavity losses for other wavelengths it is understandable that they cannot continue to work as intended when the mirror losses start to exceed the etalon losses.

---

already other optical links and thus cannot be moved — only two degrees of freedom remain, usually insufficient for satisfactory mode matching.

### 4.2.1 Standing-wave resonator

The design of our laser follows a concept by [128]. The active medium is placed in the center of symmetry between two curved mirrors which are tilted to create two sidearms terminated by flat retroreflecting mirrors. These extensions of the resonator contain wavelength selective elements that ensure stable dual mode operation and frequency tunability. Their free spectral ranges, as summarized in table 4.1, limit the respective tuning ranges. The four mirror symmetric z-shaped cavity design is particularly appropriate because this

	charact. length	FSR
Resonator length	12.7 cm	1.2 GHz
Outcoupling etalon	6 mm	$\sim 30$ GHz
Single thin etalon	150 $\mu\text{m}$	1200 GHz
Two thin etalons combined	coincidences	several 10 nm

**Table 4.1:** Free spectral ranges (FSR) of wavelength selective elements in the Ti:sapphire laser resonator

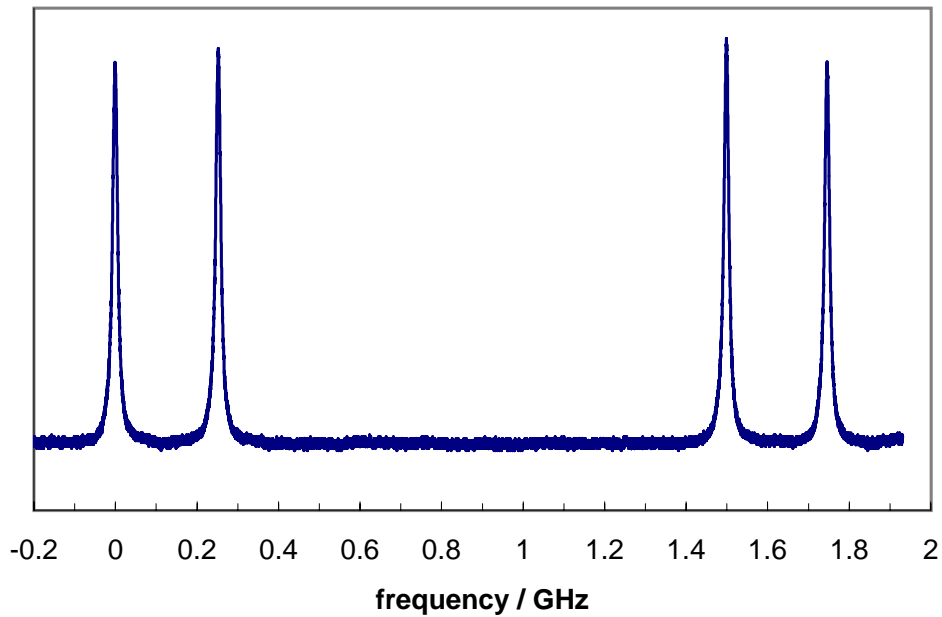


**Figure 4.5:** Fabry-Perot spectrum of the Ti:sapphire laser

due to the flat outcoupling mirror, the emitted laser beam is inherently non-astigmatic. Finally, with a crystal in the center of the resonator the entire inversion is depleted by exactly two longitudinal modes. Fluctuations due to mode competition are almost completely suppressed. A Fabry-Perot spectrum (see fig. 4.5) clearly demonstrates the dual frequency

operation of the laser. The spectrum is generated by recording<sup>3</sup> the transmission through a *confocal*<sup>4</sup> etalon whose length is scanned while the laser resonator length remains fixed.

The resonances in the confocal etalon occur at

$$\nu_{\text{lmn}} = \frac{c}{4L} [2n + (1 + l + m)], \quad l, m, n \in \mathbb{N}. \quad (4.13)$$

The *finesse*  $F$  is defined as the ratio of the distance between resonances to the width of the resonances:

$$F = \frac{\Delta\nu_{\text{FSR}}}{\Delta\nu_C} = \frac{\pi\sqrt{R}}{1-R} \quad \text{where} \quad \Delta\nu_{\text{FSR}} = \frac{c}{4L}. \quad (4.14)$$

The transmission of the etalon is given as

$$T = \frac{(1-R)^2}{(1-R)^2 + 4R\sin^2\phi} \quad \text{with} \quad T_{\text{min}} = \frac{(1-R)^2}{(1+R)^2} \quad \text{and} \quad T_{\text{max}} = 1. \quad (4.15)$$

See table B.8 for numerical values of  $F$ ,  $T_{\text{min}}$  and  $\Delta\nu_C$  for various mirror reflectivities.

The finesse of the analyzing etalon can be calculated from the free spectral ranges<sup>5</sup> of the laser resonator and the Fabry-Perot etalon by fitting Lorentzian curves to the spectrum:  $F = 144$ . The four peaks are recorded on one single ramp, in other words the two pairs are not merely mirror images but successive resonances of the laser with respect to the changing etalon length. The abscissa can be translated to the frequency domain by noting that the frequency distance between the peaks of one pair is equal to the difference of the free spectral ranges and therefore about 300 MHz.

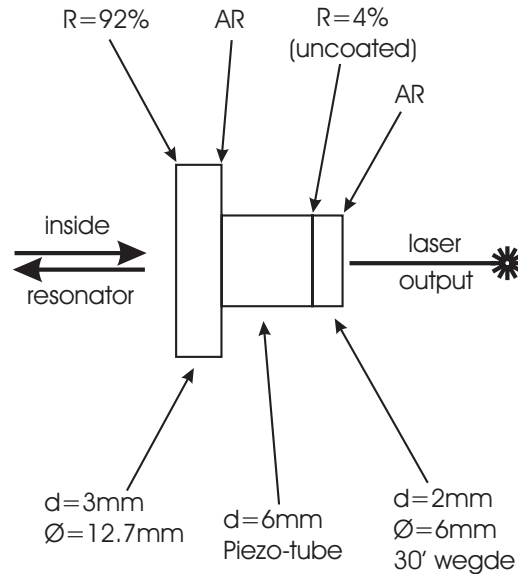


**Figure 4.6:** *Ti:sapphire output coupler etalon*

<sup>3</sup>LeCroy digital oscilloscope, global bandwidth limit (BWL) set to 30 MHz

<sup>4</sup>etalon length = mirror curvature ( $L = R$ ) and  $R_1 = R_2$

<sup>5</sup> FSR(Ti:Sa)=1.2 GHz and FSR(FP)=1.5 GHz, derived from the geometrical dimensions

Figure 4.6 shows in detail the substrate sizes and coatings used for the outcoupling etalon. Neglecting the reflectivities of the AR-coated surfaces in the outcoupler etalon, the total transmission is given by

$$T = \frac{(1 - R_1)(1 - R_2)}{(1 - \sqrt{R_1 R_2})^2 + 2\sqrt{R_1 R_2} \sin^2 \phi} \quad (4.16)$$

where  $R_1 = 92\%$ ,  $R_2 = 4\%$ , and transmission maxima (minima) occur at  $\sin^2 \phi = 0$  ( $\sin^2 \phi = 1$ ). The etalon contrast is given by the transmission range

$$5.4\% < T < 11.8\% \quad (4.17)$$

which varies with the mirror separation. A  $12\Omega$  resistor attached to the piezo allows to heat the outcoupler etalon. Together with an AD592 temperature sensor on the outcoupler mirror mount the etalon temperature is stabilized. It is necessary to be able to tune the etalon one outcoupler FSR of 0.08 nm by temperature (corresponding to about  $\Delta T = 20^\circ\text{C}$ ) in order to shift the center frequency of the laser scan to the desired position relative to the calcium transition.

At 5 Watt pump power 800 mW of outcoupled laser light indicate that at an averaged outcoupling mirror reflectivity of 94% the circulating intensity in the cavity is nearly 20 Watt. If there occurs absorption at the laser wavelength inside the crystal then instabilities due to thermal lensing are unavoidable.

According to the manufacturer the figure of merit (FOM)<sup>6</sup> of the laser crystal is greater than 250, therefore the round-trip linear absorption at the laser wavelength<sup>7</sup> should be below

$$\alpha_{\max} \cdot L = \frac{1.92/\text{cm}}{250} \cdot 2.4 \text{ cm} = 2\%. \quad (4.18)$$

Instabilities should be avoided if the excess heat of about 0.5 W can be removed from the crystal e.g. by chilled water. Experimentally we found that cooling is not strictly necessary for 5 Watt pump power but is a prerequisite at 10 Watt pump power as used in the production of 423 nm light.

	$R/\text{mm}$	$d_1/\text{mm}$	$d_2/\text{mm}$	$l/\text{mm}$	$\alpha$	$\beta$	FSR/MHz
Prototype	25.0	40.4	77.4	12.0	$12^\circ$	$31^\circ$	1180.0
“Simon version”	25.0	40.4	70.0	12.0	$12^\circ$	$31^\circ$	1253.6

**Table 4.2:** *Technical data of Ti:sapphire resonators*

The prototype Ti:sapphire laser is still used as a pump laser for a Tm:YAG-laser<sup>8</sup>, but a second, more permanent version of the Ti:sapphire laser was built using the resonator design of Mr. Simon from MPQ/Garching, for technical data see table 4.2. Figure 4.7 shows a photograph of the laser in operation.

<sup>6</sup>defined as the ratio of the absorption at the pump wavelength to the absorption at the laser wavelength

<sup>7</sup>the absorption at the pump wavelength is 1.92/cm

<sup>8</sup>see section 4.4

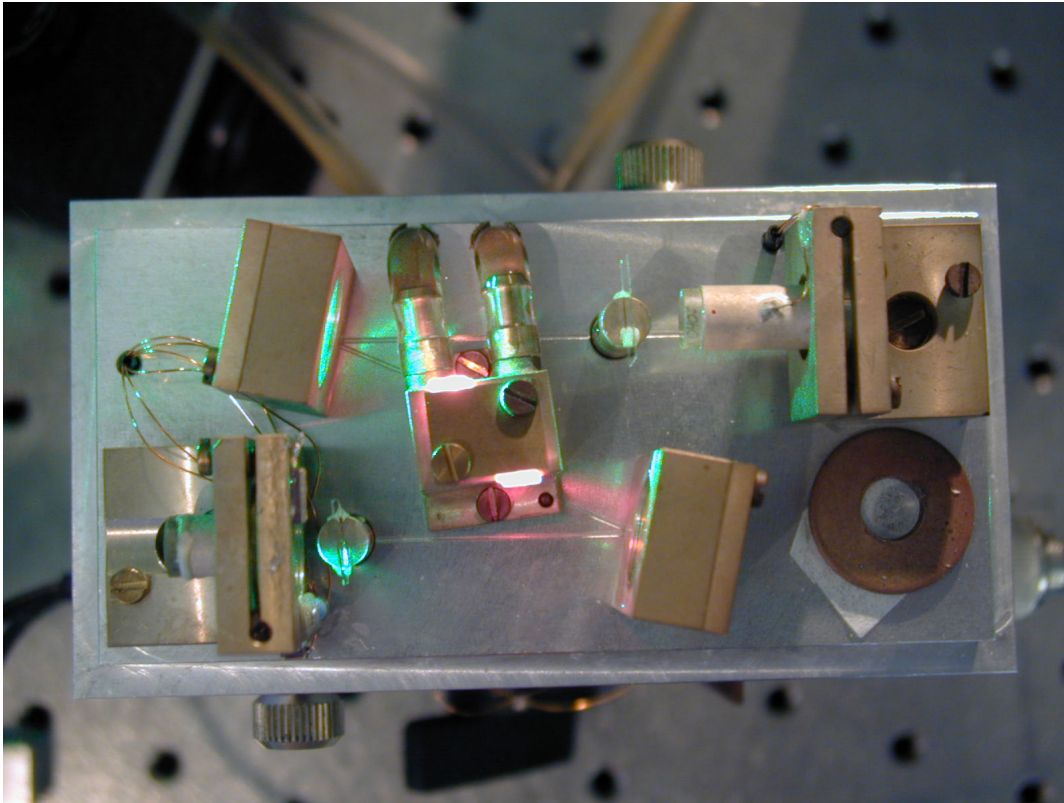


**Figure 4.7:** Photograph of the Ti:sapphire laser (approx. drawn to scale).

There are two main improvements of this setup compared to the prototype: firstly the thin etalons can be adjusted while the lid is closed thanks to o-ring translation of two orthogonal axes that connect outer knobs to the etalon holders through the base plate. Secondly both etalons are now located very close to the plane end mirrors since they don't share one branch of the resonator anymore. This places them at a position where the wavefront curvature is minimal as desired for an etalon placement. The stability diagram for this resonator is shown in figure 4.8.

Yet another Ti:sapphire laser for the calcium experiment was built by Stephan Ritter, this time a ring resonator [104]. The laser is in its optimization phase and will replace the standing wave resonator if it allows to reach higher intensities of blue light after the frequency doubler.

### 4.2.2 Output mode

The output beam parameters of the laser have to be known accurately enough to perform optimal mode matching with other resonators. The theoretical values are given in table 4.3, and we measured them for the Ti:sapphire laser: the beam scanner<sup>9</sup> was placed at a distance of  $z = 355$  mm to the laser focus in the resonator and averaged over 20 scans. The measured values are given in table 4.4.

<sup>9</sup>BeamScan Model 1180, Photon Inc. (courtesy of the Huber research group at ILP)



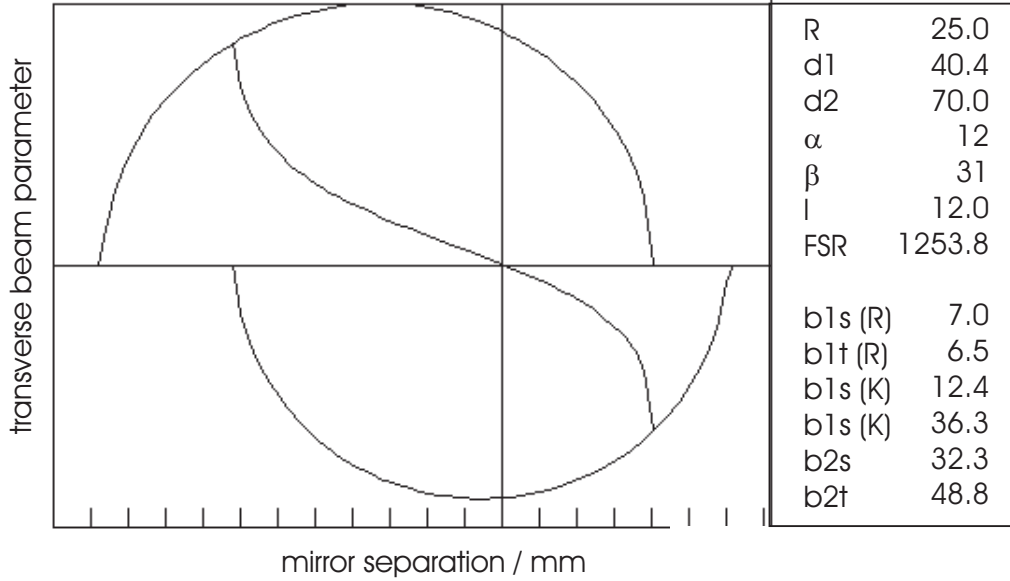


**Figure 4.8:** Stability range of the Ti:sapphire laser. The beam waist at the crystal position  $b_1$  is plotted against the separation of the curved mirrors  $d_1$  (in mm). The three traces are the sagittal, the transversal waist, and their difference. Values for the position of zero difference are given on the right.

resonator	$b_1^s(\mathbf{R})$	$b_1^t(\mathbf{R})$	$b_1^s(\mathbf{C})$	$b_1^t(\mathbf{C})$	$b_2^s$	$b_2^t$
Ti:sapphire	7.0	6.6	12.4	36.3	32.3	48.7
KNbO <sub>3</sub> (423nm)					204.3	164.2

**Table 4.3:** Sagittal ( $s$ ) and tangential ( $t$ ) beam parameters  $b = 2\pi w^2/\lambda$  at the crystal position ( $b_1$ ) without crystal ( $\mathbf{R}$ ), inside the crystal ( $\mathbf{C}$ ), and at the output coupler focus ( $b_2$ ), all values in mm.

### 4.2.3 Pump laser

The Ti:sapphire laser is pumped by a commercial, diode bar pumped solid state laser called VERDI<sup>®</sup> by Coherent: the power supply container houses and controls two diode laser arrays with aluminum-free InGaAsP active areas which are electrically pumped at about 18 Amp. Their radiation is transferred to the adjustment-free, sealed laser head via glass fibres inside a 3 m long umbilical. There a Nd:YVO<sub>4</sub> crystal gets pumped, and its radiation (1064 nm) is frequency doubled by an intra-cavity LBO crystal, see figure 4.9. Other optical elements in the resonator are an etalon, an astigmatic compensator, and an optical diode which only allows lasing in one direction by suppression of the counterpropagating laser mode. The etalon is adjusted for minimal walkoff error and is tuned by temperature. The LBO crystal is used for type I frequency doubling — its noncritical phase matching temperature is at 142° C. The laser diodes, the two crystals, the etalon, and the baseplate of the laser head are temperature controlled by the power supply unit. The laser runs single-

	$\emptyset/\mu\text{m}$	$w_s(z)/\mu\text{m}$	$\theta$	$w_0/\mu\text{m}$	$b/\text{mm}$
sagittal	1725	862.5	$2.43 \cdot 10^{-3}$	110.6	91.1
transversal	1543	771.5	$2.17 \cdot 10^{-3}$	123.6	113.8

**Table 4.4:** Measured beam parameters of the Ti:sapphire laser output beam: beam waist  $w$ , divergence angle  $\theta = w/z = w_0/z_R = 2/(k w_0)$ , beam waist at the focus  $w_0$ , and confocal beam parameter  $b = 2\pi w^2/\lambda$

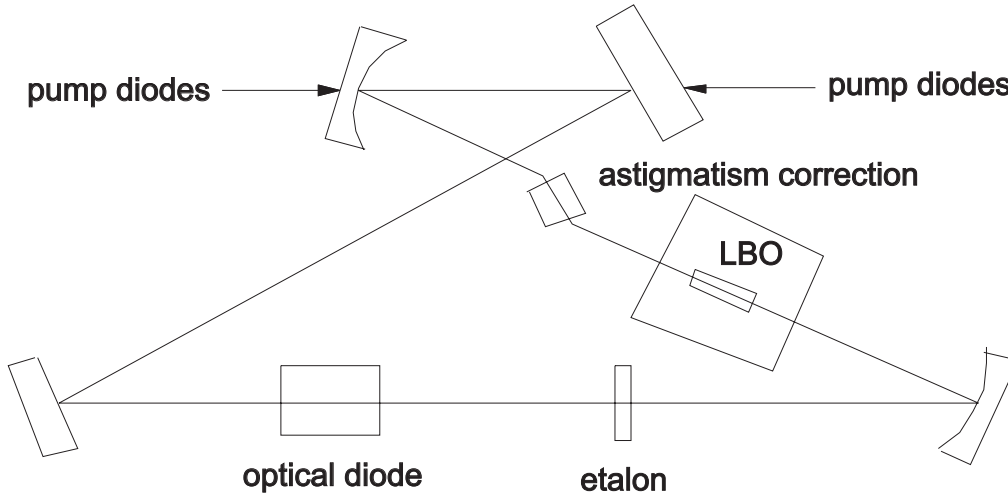


**Figure 4.9:** Ring resonator in the Verdi laser head

mode at 532 nm with a linewidth  $< 5$  MHz and low noise  $< 0.02\%$  rms. Two VERDI lasers are used in the experiment: a 10 W model is used in the 423 nm setup, and a 5 W model pumps the Ti:sapphire laser that in turn pumps the Tm:YAG laser described in section 4.4. The power stability of  $\pm 1\%$  and the pointing stability were checked with a quadrature photo diode. To verify the advertised beam parameters we performed a measurement on the 10W-VERDI using a Coherent *Modemaster* beam propagation analyzer, results for different VERDI output powers see table 4.5.

#### 4.2.4 Cooling water cycle

The pump laser is cooled by a closed loop chiller system<sup>10</sup> running on purified water. Cold water — usually at  $16^\circ\text{C}$  — is sent to the diode bars as well as the laser head<sup>11</sup>. Unfortunately the materials of the chiller reservoir (copper) and the Verdi laser head (aluminium) reacted, and corrosive material deposited at the laser head cooling water exit which got increasingly clogged. This resulted in a temperature increase of the base plate under operation to well above  $30^\circ\text{C}$ , once after 5 hours of operation even  $43^\circ\text{C}$  were found!

Two remedies resolved the obstruction: the cooling liquid connections at the laser head were increased from M4 to M6, and secondly about 20% of the cooling water were replaced

<sup>10</sup>Neslab CFT-25 recirculating chiller with PD-1 pump, cooling capacity 580 W @  $20^\circ\text{C}$ , max. 5.5 bar

<sup>11</sup>cooling liquid channel in laser head base plate: width 5 mm, depth 10 mm

	200 mW	1 W	5 W	10 W
$M^2$	1.15	1.12	1.11	1.15
$2 w_{0x}$ (mm)	1.687	2.539	2.051	1.412
$2 w_{0y}$ (mm)	2.085	2.464	2.048	1.474
$z_{0r}$ (m)	-7.563	-7.409	-7.134	-5.899
divergence $\Theta_r$ (mrad)	0.41	0.30	0.37	0.54
astigmatism $(z_{0y} - z_{0x})/z_{rr}$	-29.9%	14.6%	14.0%	11.7%
waist asymmetry $2w_{0y}/2w_{0x}$	1.236	0.971	0.999	1.044
divrg. asymmetry $\Theta_y/\Theta_x$	0.827	1.077	1.053	1.012

**Table 4.5:** External VERDI beam parameters calculated from measurements at 3 m distance to laser exit

by an corrosion inhibitor<sup>12</sup>. Also, an anti-algae substance<sup>13</sup> is added to the cooling liquid since transparent tubing is used on parts of the system.

Switching from 5 Watt to 10 Watt pump power it turned out that cooling of the pumped Ti:sapphire crystal is strictly required at this high power, and thus a link to the crystal was added to the existing cooling cycle. Without cooling the crystal a stable bimodal operation of the Ti:sapphire laser is not possible due to thermal lensing caused by the high intensity in the pump focus.

#### 4.2.5 Long-term stabilization of the Ti:sapphire laser

To stabilize the output of the Ti:sapphire laser with respect to long-term frequency drifts we built a feedback loop consisting of a wavelength discriminator (a scannable Fabry-Perot etalon, see figure 4.10 and table B.8) that provides an error signal and an electrical feedback generator (called lockbox from now on) that influences the laser emission through changes to the length of the wavelength selective elements in the resonator. The Fabry-Perot etalon consists of two convex mirrors (2) glued to a Zerodur glass spacer (1) that features a low temperature expansion coefficient to minimize drifts due to temperature changes. One of the mirrors additionally sits on a thin piezoelectric disc (3) that allows to scan the resonator length while keeping possible temperature drifts to a minimum. The electrical leads (8) are very thin (angel's hair) to avoid coupling to external vibrations. The resonator rests inside a rectangular aluminum container (4) filled with wool as a damping material which also suppresses convection and therefore heat transport. A second aluminum container (5) surrounds the first separated by yet another layer of insulation. Three large heater sheets<sup>14</sup> on the top, the front, and the back side heat the outer box (6) to about 35°C. A temperature sensor attached to the inside of this container allows to measure and stabilize the temperature using an electrical feedback loop to within 20 mK. The required heating power is estimated by  $P = mc \Delta T / \Delta t \approx 80$  Watt, where  $m = 1300$  g and  $c = 0.89$  J/(kg K) are the mass and the heat capacity of the enclosure,  $\Delta T = 40$  K is the proposed

<sup>12</sup>Ethylene glycol, used about 750 ml on 2.2 l H<sub>2</sub>O (dest.)

<sup>13</sup>Chloramine T Trihydrate, Merck 8.18705.0250, about 1 g per 3.5 l water

<sup>14</sup>Minco HR5175 R49.4 L12B, 76.2 × 127.0 mm, 49.4 Ω @ 20°C

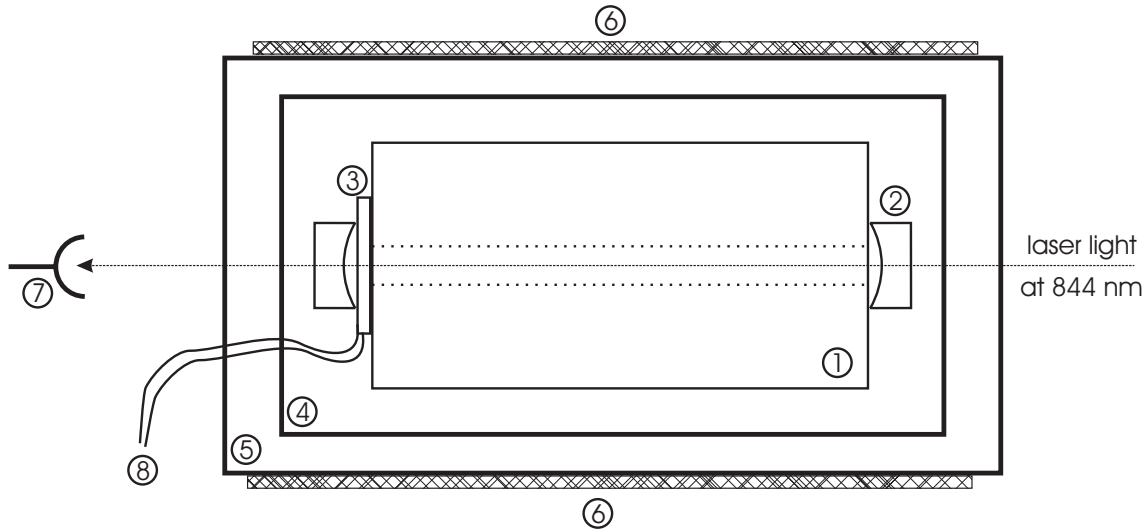


**Figure 4.10:** *Stabilizing Fabry-Perot etalon setup (labels see text)*

temperature difference between not heating and heating, and  $\Delta t = 10$  min is the desired heating-up time.

Some light from the Ti:sapphire laser is coupled into the resonator via two adjustable mirrors, and a silicon photo diode (7) records the transmission. Scanning the laser frequency one can observe the resonances in the transmitted signal. The stabilization of the laser on this error signal is also called side-of-fringe lock.

### 4.3 Frequency doubling, shifting, and stabilization

Nonlinear processes in certain crystals provide a way to transform light of frequency  $\nu$  partially into its harmonics  $2\nu, 3\nu, \dots$  which allows to obtain coherent radiation in the blue and ultraviolet region of the electro-magnetic spectrum [127]. The material  $\text{KNbO}_3$  offers a high conversion efficiency for second harmonic generation (SHG), which was extensively studied by several groups [96, 14, 55]. The light power  $P_2$  in the harmonic beam depends on the incident fundamental power  $P_1$  as

$$P_2 = \gamma P_1^2 = \frac{(4\pi d_{\text{eff}})^2}{(n\lambda)^3} \cdot \frac{Lh}{\varepsilon_0} \cdot P_1^2, \quad (4.19)$$

where the conversion coefficient  $\gamma$  was inserted according to [16];  $d_{\text{eff}}$  is the nonlinear coefficient of the crystal. The experimental values for the  $\text{KNbO}_3$ -crystal were  $\lambda = 845$  nm,  $n \approx 2.2$ ,  $L = 5$  mm,  $\varepsilon_0 = 8.85 \cdot 10^{-12}$  AsV $^{-1}$ m $^{-1}$ , and  $d_{\text{eff}} = -20.5$  pm/V (at 857 nm). The optimum conversion parameter  $h \approx 0.2$  is found from [16] when the confocal parameter  $b = 20$  mm is used, thus  $\xi = 0.25$  ( $B = \sigma = \mu = 0$ ).

In resonator enhanced frequency doubling [96, 127, 14], the efficiency of the nonlinear process is increased by placing the nonlinear crystal inside an optical buildup cavity with high reflectors for the fundamental wavelength. The optimal transmission coefficient (at this wavelength) for the input coupler is equal to the cycling losses inside the resonator

which are firstly due to the transmission of the other mirrors and secondly due to conversion into second harmonic radiation in the crystal.

The output of the dual mode Ti:sapphire laser contains two frequencies  $\omega_1$  and  $\omega_2$  separated by one FSR which is due to the standing-wave resonator design as described in 4.2. This setup is an excellent choice in cases where the output is intended to be frequency doubled. Both frequencies can be simultaneously resonant in the doubling resonator, if its FSR (or an integer multiple of it) matches the Ti:sapphire laser FSR. Therefore, one is not free in the choice of doubling resonator length, and its tuning is critical for highly efficient second harmonic generation (SHG). The output of the summing frequency process then contains three frequency components: photons with energies  $\hbar(\omega_1 + \omega_1)$ ,  $\hbar(\omega_2 + \omega_2)$ , and  $\hbar(\omega_1 + \omega_2)$  of which the last component is twice as strong in amplitude as each of the others. The intensity then scales as 1:4:1 which can be observed when the laser scans across the calcium resonance.

It's possible to check the buildup cavity length and hence its FSR: when the Ti:sapphire laser is tuned to its next resonator mode then the intensity coupled into the doubling resonator decreases unless the two resonators are well matched.

### 4.3.1 Locking the doubling cavity to the Ti:sapphire laser

The length of the frequency doubling cavity quickly fluctuates due to mechanical vibrations and slowly changes due to thermal drifts. In order to keep the cavity in resonance with the infrared radiation it is necessary to generate some kind of error signal that allows to control the resonator length via feedback. This can be achieved with the *Pound-Drever-Hall stabilization* [37]. To this end sidebands at 40 MHz are introduced to the infrared beam by an electro-optic modulator (EOM) which in this case is a LiNbO<sub>3</sub>-crystal<sup>15</sup>. Due to the high optical power density of more than 1 W/mm<sup>2</sup> of infrared light the crystal quickly loses its transparency. This effect is completely suppressed<sup>16</sup> by maintaining a crystal temperature of around 100 to 120°C. The relevant curing process might be increased electron mobility and therefore increased conductivity, that could adversely lead to electrolysis at radio frequency fields above 100 V/mm.

A fast photo diode observes the light which is reflected from the doubling cavity. The DC signal can be used to check the coupling efficiency into the cavity by scanning the cavity length and monitoring the reduced reflection on resonance. About 70% of the incident radiation should be coupled into the cavity on resonance. The AC signal is demodulated by mixing it with the original 40 MHz radio frequency signal. Before demodulation the phase of the two signals is adjusted to yield a purely dispersive output signal. This error signal controls the cavity length piezo via an active feedback circuit.

### 4.3.2 Environment for the nonlinear crystal KNbO<sub>3</sub>

The phase matching temperature in KNbO<sub>3</sub> for 423 nm is found at around -18°C, well below the freezing point. Any residual water vapor in the atmosphere around the crystal

<sup>15</sup>see C.1 and C.3; crystal is heated to  $\approx 100^\circ\text{C}$  by a  $15\Omega$  resistor applying 12.2V/0.8A

<sup>16</sup>private communication with J.-P. Meyn (Kaiserslautern), S. Schiller (Düsseldorf)

would condense immediately and cover the crystal and its Peltier-cooled container with a thick layer of ice. Even small water drops on the crystal faces would be sufficient to disturb the light passage, therefore one has to supply a very dry atmosphere. We decided to use the already predried pressurized air from the building's in-house gas supply and use the cooling and drying effect of the expansion to atmospheric pressure. So the idea is that a gas at high pressure is actively cooled, and water condenses down to the humidity at that high pressure. Afterwards the air is expanded to a lower pressure near 1 bar — atmospheric pressure. The water content in the processed air will be smaller than in room air by a factor given by the difference in the involved pressures.

The atmospheric humidity is approximately  $17 \text{ g/m}^3$ , the saturation humidity at room temperature. The desired dry air flow into the doubling resonator enclosure is about  $4 \text{ l/min}$  or  $7 \times 10^{-7} \text{ m}^3/\text{s}$  at 1 bar. The evaporation energy of water at room temperature is  $Q(\text{H}_2\text{O})=2080 \text{ kJ/kg}$ . Thus we find the required cooling power  $P = 17 \text{ g/m}^3 \cdot 6.7 \times 10^{-7} \text{ m}^3/\text{s} \cdot 2080 \text{ J/kg} = 2.4 \text{ Watt}$  which is delivered by a  $30 \times 30 \text{ mm}^2$  peltier element to a round copper container. The condensed water can be removed by gravity through a suitable valve. To further suppress crystal contamination the dried air is then passed through a plastic bottle filled with dry silica grains which also dampens vibrations from the high pressure gas system. The method described was found to be sufficient to prohibit any condensation on the cold surfaces. The success can also be monitored by observing the color of some silica gel crystals that have been placed inside the doubling cavity housing<sup>17</sup>.

The crystal can be damaged by quick temperature changes. The recommended<sup>18</sup> max. temperature change of  $1^\circ\text{C}/\text{min}$  was assumed to be overly cautious, but we never exceeded a limit of about  $3^\circ\text{C}/\text{min}$  on average.

### 4.3.3 Improved sum frequency generation using an LBO crystal

The maximum power of 423 nm radiation achieved with the  $\text{KNbO}_3$  system was about 150 mW. This turns out to be a fundamental limit since strong thermal lensing in the doubling crystal prohibits further increases in output power even at much increased pump power levels. When the doubling cavity comes into resonance, a pump power dependent thermal lens emerges in the crystal. This quickly destroys the mode matching condition, so additional pump power is simply reflected at the input coupler of the doubling cavity. Switching to a different nonlinear material was necessary: lithium tetraborate ( $\text{Li}_2\text{B}_2\text{O}_4$  or LBO) has a much lower single pass efficiency than  $\text{KNbO}_3$ , but this can be overcome by closing the enhancement cavity with mirrors of higher reflectivity and thus increasing the effective number of passes. The damage threshold of LBO is sufficiently high, and thermal effects are much less dominant than in  $\text{KNbO}_3$ . A photograph of the buildup cavity resonator is shown in figure 4.11.

LBO can be angle tuned, which is called Type I phase matching. Temperature stabilization is not necessary, but small resistors<sup>19</sup> constantly heat the crystal to approx.  $40^\circ\text{C}$

---

<sup>17</sup>The color changes from blue to red in the case of a wet atmosphere. The process can be reversed by heat treatment.

<sup>18</sup>F. Riehle, PTB Braunschweig, private communication

<sup>19</sup>  $5 \text{ V}$  over  $24 \Omega \parallel 24 \Omega \rightarrow 400 \text{ mA}$

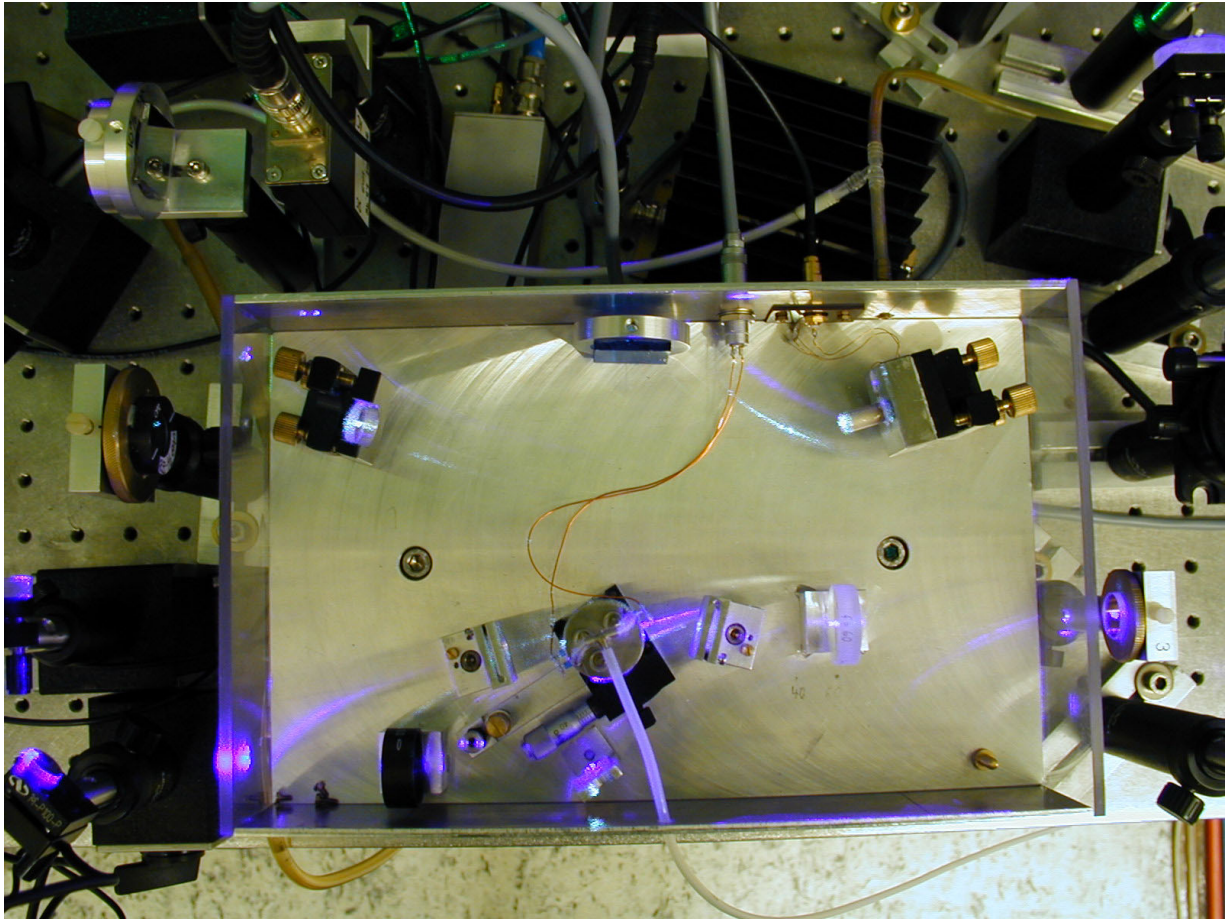


**Figure 4.11:** Photograph of the frequency doubling ring resonator for the LBO crystal. The distance of table holes (25 mm) can be used as a dimension reference.

to avoid crystal deterioration due to its slightly hygroscopic nature. The index of refraction in the nonlinear crystal depends on the laser wavelength and the orientation of the polarization relative to the LBO crystal axis, see table 4.6.

The phase matching angles  $\theta = 90^\circ$  and  $\phi = 27.9^\circ$  are found as follows: The fundamental wave is polarized in the  $z$ -direction. The second harmonic beam in the  $xy$ -plane has to be polarized such that the effective index of refraction  $n_{\text{eff}}$  matches the fundamental index

845 nm	$n_x = 1.5685$	$n_y = 1.595$	$n_z = 1.6099$
423 nm	$n_x = 1.5871$	$n_y = 1.6163$	$n_z = 1.6316$

**Table 4.6:** Anisotropy of the refractive indices of the nonlinear crystal LBO



of refraction. This is possible since  $n_x(423 \text{ nm}) < n_z(845 \text{ nm}) < n_y(423 \text{ nm})$  and then

$$\begin{aligned} \frac{\sin^2 \phi}{n_x^2} + \frac{\cos^2 \phi}{n_y^2} &= \frac{1}{n_{\text{eff}}^2} \\ \Rightarrow \sin \phi &= \frac{n_x}{n_{\text{eff}}} \sqrt{\frac{n_{\text{eff}}^2 - n_y^2}{n_x^2 - n_y^2}} \\ \Rightarrow \phi &= 27.9^\circ. \end{aligned} \quad (4.20)$$

The crystal is mounted on a rotation and a tilting stage to optimize the crystal orientation relative to the incident fundamental beam. The required angular resolution for the crystal rotation stage is determined by the following condition: the velocity  $v$  of light in a medium depends on the wavelength. Two wavelengths are resonant in the doubling cavity as long as the path length difference  $\Delta s$  in the crystal is much smaller than the wavelength:

$$\Delta s = \Delta v t = \Delta v L/c \stackrel{!}{\ll} \lambda \quad (4.21)$$

$$\Rightarrow \Delta n \ll \frac{\lambda}{L} \stackrel{\text{here}}{=} 6' = 1.7 \text{ mrad}, \quad (4.22)$$

where  $L$  is the crystal length and  $\Delta n = \Delta v/c = (v_1 - v_2)/c$  is the difference in refractive indices.

Due to destructive interference a minimum of the nonlinear process occurs for  $\Delta n \cdot L_{\text{LBO}} = \lambda_{423\text{nm}}$ , where  $\Delta n = n_{423\text{nm}} - n_{844\text{nm}}$ . This corresponds to a horizontal angle of  $\phi_h = 0.05 \text{ rad} \hat{=} 2.9^\circ$  and a vertical angle of  $\phi_v = 0.0015 \text{ rad} \hat{=} 0.09^\circ$ . These angles can be avoided by suitable tuning of the rotation and tilting stage.

Previous experiments<sup>20</sup> with LBO have shown that AR coatings on LBO are easily damaged by high light intensities. Therefore, we use a  $3 \times 3 \times 15 \text{ mm}^3$  LBO crystal with parallel Brewster ends. The crystal is oriented such that the fundamental beam enters and leaves the crystal without losses under the Brewster angle of  $58.2^\circ$ . However, the harmonic beam at 423 nm is polarized perpendicularly to the fundamental beam and is thus partially reflected at the exit face. To make use of this light — which otherwise would be lost — one side face is polished, and a small piece of AR-coated glass is attached with index-matching fluid<sup>21</sup>. About 40 mW are now additionally extracted can be used for spectroscopy.

The second harmonic power at the main output is usually 300 mW at 1.5 W fundamental power without notable limitation by thermal effects inside the crystal. As already mentioned in the beginning of this section only 2/3 of the output intensity is available for the experiment since the remaining 100 mW are contained in the two lower intensity side-modes.

### 4.3.4 Frequency shifting

The combined laser system of Ti:sapphire and nonlinear frequency doubling crystal can provide light of one specific frequency near the 423 nm calcium line to the experiment.

<sup>20</sup>P. Schmidt, Konstanz University, private communication

<sup>21</sup>optical couplant Dow Corning Q2-3067



However, the wavelength of the slower and the trap beams are slightly different since the optimum detuning for the trap beams is one natural linewidth of 35 MHz, but the slower is designed for 270 MHz detuning from the trap beams. The laser wavelength is set and locked to the detuning that optimizes the number of trapped atoms. A combination of a  $\lambda/2$ -plate and a polarizing beamsplitter diverts about 50% of the power in the trap beams into a second beam that is shifted in frequency by an *acousto-optic modulator* (AOM)<sup>22</sup>. The highest diffraction efficiency of about 85% was found at 21 to 23 dBm radio frequency (RF) power. The efficiency does not depend on the input polarization.

### 4.3.5 Stabilization of the 423 nm radiation to the calcium line

The output of the Ti:sapphire laser can be stabilized to a resonator as described above, see section 4.2.5. This might be sufficient if no particular wavelength must be delivered. In the case of laser cooling, however, we always have to adjust the laser wavelength with respect to the atomic transitions, and for that we need an atomic frequency reference.

In alkali experiments small transparent glass cells are used that contain small amounts of the metal of interest. Its vapor pressure at room temperature is sufficient to perform saturation spectroscopy [33, pp. 301–310] and thus to establish an atomic frequency reference. In calcium the situation is more difficult: in order to get any atomic absorption in the gas phase calcium has to be heated considerably to temperatures beyond the operating values of glass cells. Also, in alkali glass cells the deposited material on the laser entrance windows can easily be heated away with moderate temperatures below 100°C. In contrast, in calcium experiments the deposition of material on the windows poses considerable problems, see also page 36.

To provide the required calcium atoms for a reference absorption spectroscopy we built a small steel vacuum chamber which will be called *calcium cell* in the following<sup>23</sup>. About 2 g of metallic calcium are heated at one end of the cell by direct heating of the vacuum wall using a heater wire<sup>24</sup> wrapped into machined grooves in the steel wall. Atoms are evaporated into a cloud and form a mildly collimated beam by flying through a 30 cm long tube into a double vacuum cross, the observation region. The laser is now sent multiple times through the two viewports on the horizontal ports to cross the atomic beam to thus produce as much fluorescence as possible, which is observed at the top port by an amplified photodiode, see figure 4.12. At a DC heater current of 4.5 A (14 V) and about 16 mW optical power at 423 nm in the spectroscopy laser output (300 mW at main output) the diode delivers a 60 mV absorption signal into 1 M $\Omega$  and shows only few mV noise, so  $S/N \approx 25$ .

The atomic beam proceeds into a final vacuum-tee: at the lower port a high vacuum elbow valve allows to connect to a turbo pump, and a small 2 l/s ion pump<sup>25</sup> on the top port maintains the high vacuum after pump-down and bake-out. The pressure  $P$  [torr] in the cell can be monitored via the ion pump current  $I_i$  [A]: in a log-log-plot the relation between them is linear in the range from  $10^{-6}$  up to  $10^{-3}$  A and scales as  $P = 10^{\log I_i + b}$

<sup>22</sup>AOM ATM-2701A1 by IntraAction, Illinois. The designed center shift is 270 MHz.

<sup>23</sup>Alternatively a heat pipe design with inductive heating could be used [82].

<sup>24</sup>Philips Thermocoax 1NcI10/22cm, single stranded

<sup>25</sup>pressure/torr  $\approx 6 \cdot 10^{-8} \times \text{current}/\mu\text{A}$

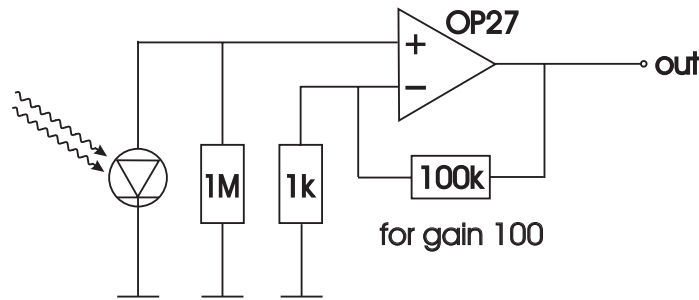


**Figure 4.12:** Detection and amplification of fluorescence at the calcium cell

with  $b \simeq 1.1675$ . Without heating the reservoir the ion pump current is below the lower detection limit of  $0.1 \mu\text{A}$ , the vacuum being better than  $10^{-8}$  torr. When the cell is heated to the operating temperature<sup>26</sup> of  $600^\circ\text{C}$  the current increases to several  $\mu\text{A}$ , thus the pressure in the cell is then slightly above  $10^{-7}$  torr, mainly due to increased outgassing from the hot vacuum walls and from impurities in the calcium material. The hot calcium gas atoms themselves will stick immediately to any cold surface and are not pumped by the ion pump, therefore they do not influence the current or the measured pressure.

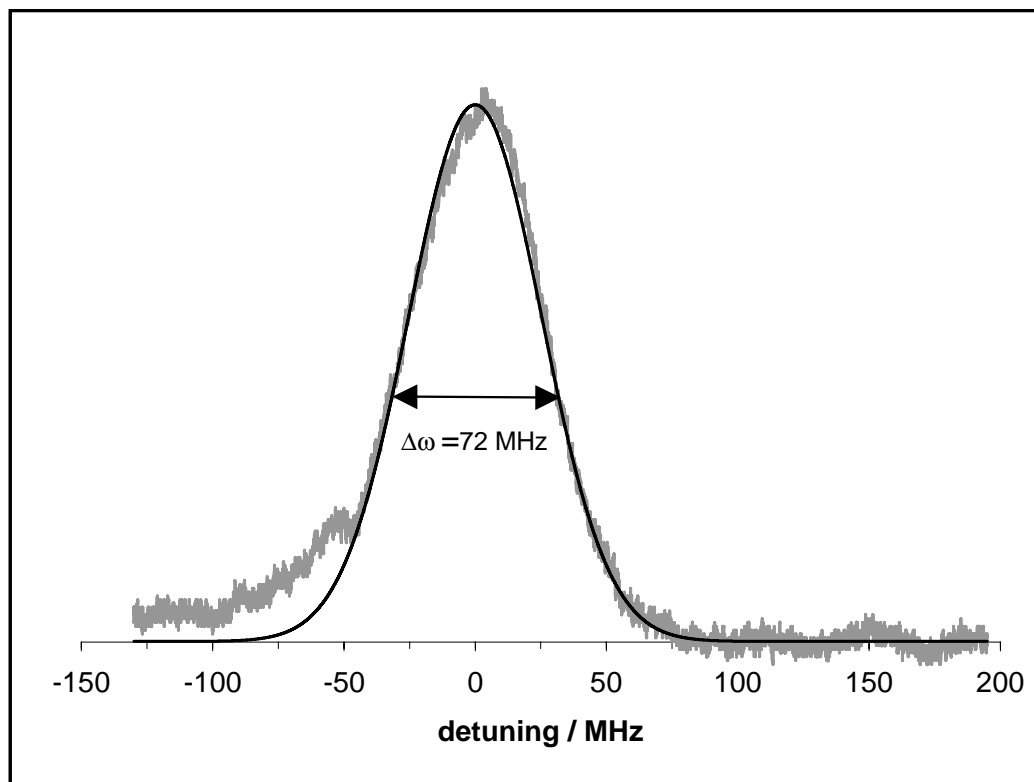


**Figure 4.13:** The broad calcium line at  $423 \text{ nm}$  can be easily found using the small atomic beam cell; here  $S/N=30$ , and the fitted Doppler curve has a FWHM of about  $72 \text{ MHz}$

<sup>26</sup>measured with thermo element Thermocoax FKI10/25 (Inconel)

One can find the atomic resonance by shining the 423 nm light perpendicularly through the small atomic beam, scanning across the atomic resonance and recording the blue fluorescence. This yields a spectrum where the resonance has a width of 71.5 MHz due to the transverse atomic velocity of several m/s in the thermal beam, see figure 4.13. The frequency axis is calibrated by scanning simultaneously across an etalon<sup>27</sup> with known FSR and finesse.

By scanning the Ti:sapphire laser frequency and adjusting the offset of the reference resonator cavity piezo (see 4.2.5) it is possible to achieve a coincidence of resonances in the calcium cell absorption signal (see figure 4.13) and the reference resonator signal. An electronic offset allows to shift the baseline to cross the resonance signal at the desired locking point on the signal slope and thus presents an error signal to the feedback. This locking technique is called *side-of-fringe lock*. It is necessary to lock the laser to a freely adjustable signal like that of the reference resonator instead of directly to the atomic absorption signal since only then it is possible to lock the laser further off resonance than half a linewidth.

## 4.4 A solid state laser for 2 $\mu\text{m}$ radiation

Experimental physics demands every now and then to find entirely new ways to cope with challenges posed by nature. In atomic physics spectroscopically interesting atomic lines have always fuelled the development of new lasers. Commercial enterprises naturally focus their attention to some key wavelength areas as apparent in the semiconductor lasers that are available throughout the visible and near-infrared up to 1000 nm and also for the telecom bands around 1300 and 1500 nm. One of the spectral regions beside the well-travelled roads is the range above 1.7  $\mu\text{m}$  up to several microns. Only very recently some companies and research institutes started characterizing material systems suitable for single mode diode lasers in this spectral region. This was the reason for us to develop our own solid state laser using thulium doped yttrium aluminium garnet (Tm:YAG) as an active medium. The material is particularly suited for a three-level laser emitting at 2  $\mu\text{m}$  since it exhibits self-quenching as illustrated in figure 4.14. The upper laser level  $^3\text{F}_4$  is populated through the phonon-assisted self-quenching process  $^3\text{H}_4 + ^3\text{H}_6 \rightarrow ^3\text{F}_4 + ^3\text{F}_4$  [114]. The quenching efficiency increases with higher Tm<sup>3+</sup> concentration (here 6%). The pump wavelength is 786 nm which can be delivered at high power by a standard Ti:sapphire laser. In future versions high-power semiconductor lasers can be used as pump sources due to the convenient pump wavelength.

We designed a compact Tm:YAG laser tunable from 1940 nm to 2030 nm. The wavelength is adjusted with two intracavity etalons. The output is a nonastigmatic circular single transverse mode Gaussian beam comprised of two longitudinal modes separated by a free spectral range of 1 GHz. A maximum of 80 mW of infrared power has been achieved with an 800 mW Ti:sapphire pump laser at 786 nm. The laser can be tuned rapidly by 4 GHz, and its emission linewidth is less than 1 MHz. A detailed description is given in [99], and the adjustment procedure is described in C.2. The design is similar to the Ti:sapphire

---

<sup>27</sup>here FSR=  $1.5 \pm 0.5$  GHz, finesse  $F = 144 \pm 3$

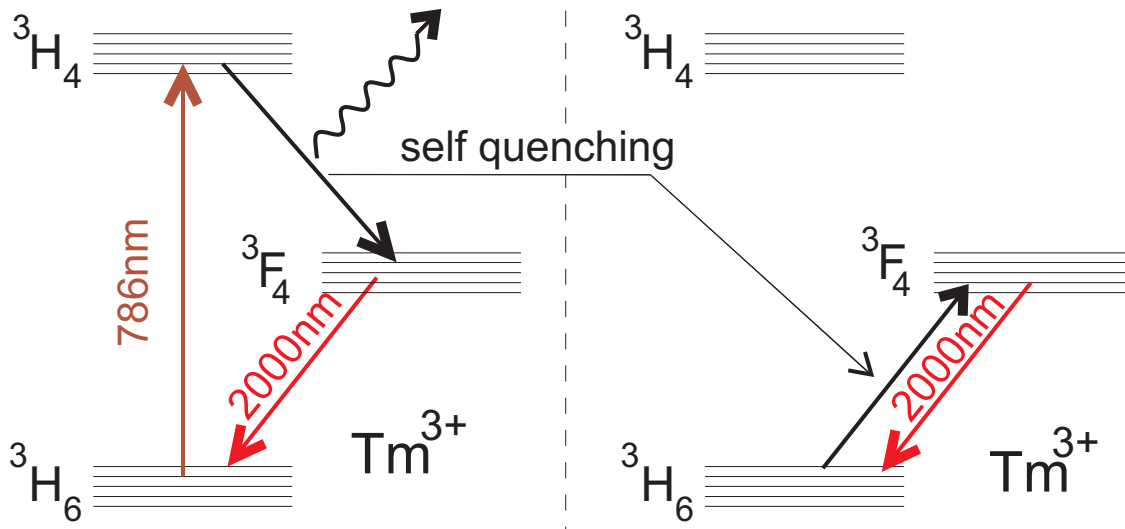


Figure 4.14: *Tm:YAG term scheme*

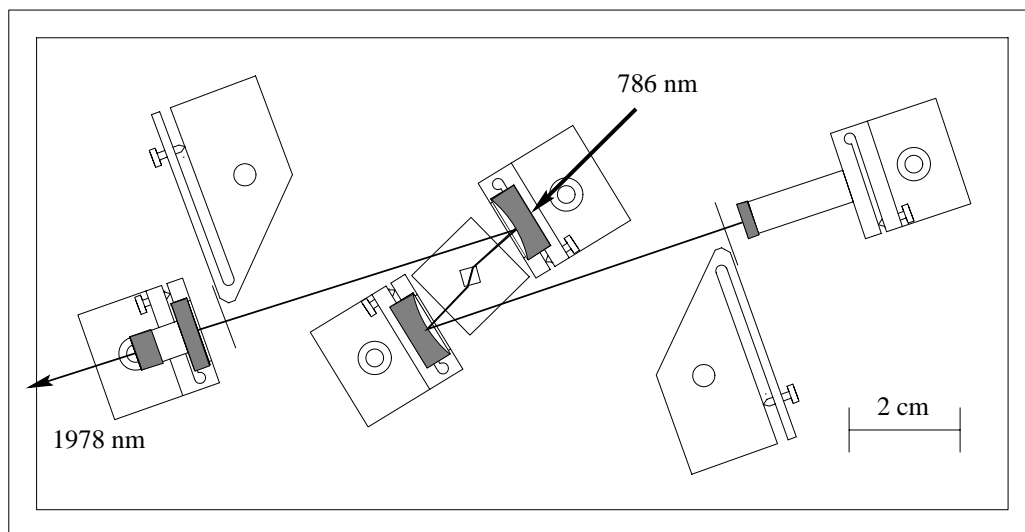
laser (see section 4.2 and [128]): a miniature standing wave resonator with several wavelength selective intracavity elements resulting in dual mode operation and high passive stability, see 4.16 for a photograph of the resonator.

The transverse mode spectrum is determined by the pump mode and laser mode overlap and the pump laser transverse modes. The pump wavelength has to be  $785.5 \text{ nm} \pm 1 \text{ nm}$  since the thulium absorption is restricted to this extraordinarily small range. For these two reasons it is advisable, if not mandatory, to use a high-quality pump laser such as a Ti:sapphire laser that also offers sufficient power. Therefore, our Tm:YAG-laser is pumped by a Ti:sapphire laser as described in section 4.2 which itself is again pumped by a Verdi laser. Using 5 W at 532 nm results in 850 mW at 785.5 nm which in turn yields about 50 mW at the desired calcium wavelength of 1978 nm, see figure 4.18. The wavelength

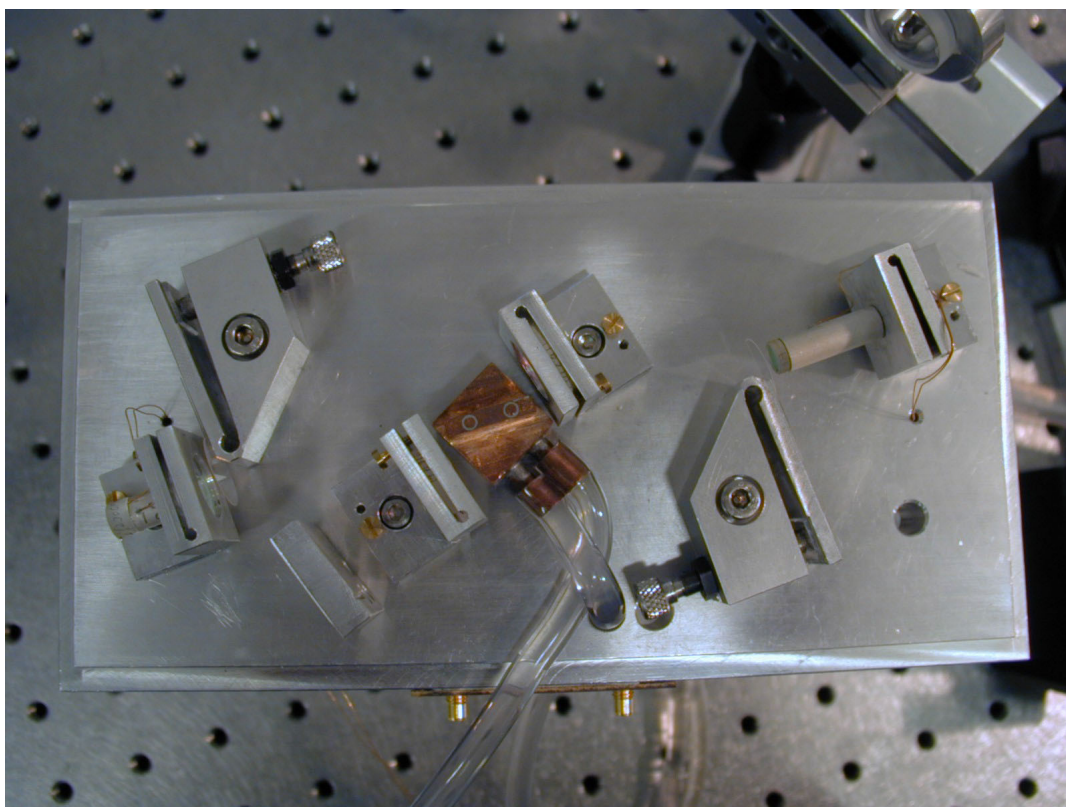
tuning element	FSR	tuning range
resonator	1 GHz	0.01 nm
outcoupling etalon	25 GHz	0.3 nm
Infrasil etalon (single)	1 THz	10 nm
Infrasil etalons (pair)		$\sim 100 \text{ nm}$

Table 4.7: *FSR and tuning range of the wavelength selective elements in the Tm:YAG resonator*

selective elements are listed in table 4.7. To scan the laser wavelength continuously a voltage ramp is applied to a piezo carrying one cavity end mirror which allows to scan one  $\text{FSR} \approx 1 \text{ GHz}$ . To span a wider scan range a corresponding voltage ramp is applied to the second piezo at the outcoupling etalon (similar to figure 4.6). The slope and the polarity of the ramps have to be adjusted carefully to avoid mode hops throughout the scan.



**Figure 4.15:** Machine shop drawing of the Tm:YAG resonator



**Figure 4.16:** Photograph of the Tm:YAG-resonator. The distance of table holes (25 mm) can be used as a dimension reference.

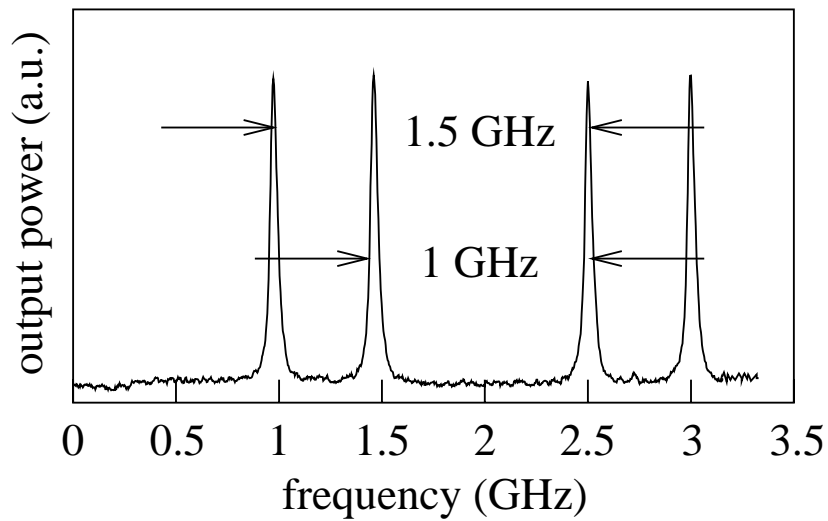


**Figure 4.17:** Demonstration of the Tm:YAG's dual-mode behavior (FSR 1 GHz) in a transmission scan using a Fabry-Perot etalon with a free spectral range of 1.5 GHz.

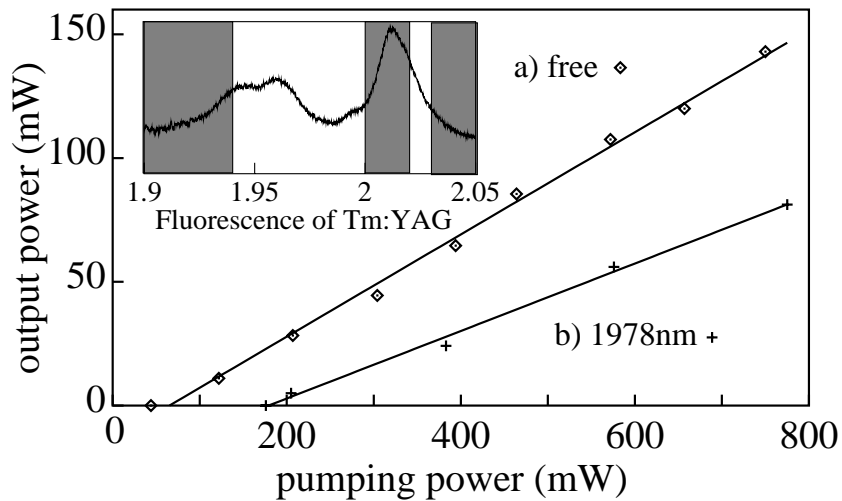


**Figure 4.18:** Output power of the Tm:YAG laser versus pump power. In a) the laser runs freely at 2014 nm (at the fluorescence maximum), in b) the etalons restrict its emission to the desired 1978 nm, and the inset shows the natural Tm:YAG fluorescence. The etalons can force the laser to run single mode only in the white spectral areas of the inset plot.

One of the laser end-mirrors is a high-reflector, but some light is still transmitted. This light is partly sent to the *wave meter* (see appendix C.3) to determine the laser wavelength and partly used to analyze the laser spectrum by looking at the transmission through an etalon. The main laser output can be analyzed and stabilized by a saturation spectroscopy setup as described in section 4.6 of this chapter.

The index of refraction of Tm:YAG is 1.803 at  $\lambda = 1978$  nm and 1.825 at the pump wavelength of  $\lambda = 785$  nm. A first version of the laser used a 3 mm long crystal with 6% Tm-doping which was placed in the resonator at Brewster angle relative to the pump beam resulting in an effective length of 3.43 mm. The second version of the crystal received a Brewster cut and has an effective length of 10 mm. More data on the geometrical dimensions and the beam waists of the resonator are given in appendix C.1.

## Mode matching

The mode matching condition is that the pump beam and the laser mode must overlap in the crystal, which can be expressed as  $w_0(2\mu\text{m}) = w_0(785 \text{ nm})$ . The starting point is the 2  $\mu\text{m}$  beam parameter. The beam parameters

- for 2  $\mu\text{m}$  in the crystal are
 
$$b_t = 10.8 \text{ mm} \quad w_{0t} = 58.3 \mu\text{m}$$

$$b_s = 3.8 \text{ mm} \quad w_{0s} = 34.6 \mu\text{m}$$
- for 785 nm in the crystal are then
 
$$w_{0t} = 58.3 \mu\text{m} \Rightarrow b_t = 27.2 \text{ mm}$$

$$w_{0s} = 34.6 \mu\text{m} \Rightarrow b_s = 9.58 \text{ mm}$$
- for 785 nm behind the crystal are
 
$$b_t = 4.7 \text{ mm} \quad l = 10.5 \text{ mm}$$

$$b_s = 5.3 \text{ mm} \quad l = 11.2 \text{ mm}$$
- for 785 nm behind the incoupling mirror are<sup>28</sup>

$$b_t = 2.94 \quad l = -8.38 \text{ mm}$$

$$b_s = 3.23 \quad l = -8.83 \text{ mm}$$

Here  $l$  is the distance between the respective point of reference and the focus. The Tm:YAG resonator has nearly no ellipticity or astigmatism in branch II in contrast to the Ti:sapphire resonator ( $b_t = 62.5$  mm,  $b_s = 44.3$  mm). The mode matching is realized with an uncoated  $f = 80$  mm achromate.

---

<sup>28</sup>These are the values that have to be matched by the pump laser.

## 4.5 The diode laser for optical pumping at 430 nm

This section describes how to contribute light at 430 nm to the experiment while its application will be discussed in 6.5.2. The 430 nm system consists of the following parts: a grating stabilized diode laser in Littrow configuration<sup>29</sup> operating at 860 nm, a frequency doubler, a polarization spectroscopy setup, and two active feedback loops. One feedback circuit locks the doubling cavity length to the diode laser by a Pound-Drever-Hall lock and the second loop locks the laser grating and thus the diode laser frequency to the atomic transition in calcium. The design of the grating stabilized diode laser was developed in the group of T.W. Hänsch [103].

### 4.5.1 Littrow configuration

The Littrow configuration is a setup to force a multi-mode laser diode to concentrate its emission to a single wavelength — to run *single-mode* [33, pp.176]. The collimated output beam of the laser diode is sent onto a holographic *sinusoidal grating* [33, p.76]. The zero order beam is diffracted into the same angle like reflection from a mirror, and some light is diffracted into higher orders. The angle of incidence is now adjusted, so that the first order diffraction is directly returned into the laser diode. The wavelength that fulfills the diffraction condition

$$z \lambda = g(\sin \alpha + \sin \beta)$$

receives a large amplification, and therefore the laser runs single-mode at the prescribed wavelength ( $z$ : diffraction order,  $g$ : grating constant,  $\alpha$ : angle of incidence,  $\beta$ : angle of  $z^{\text{th}}$  order diffraction). The actual output beam of the external cavity stabilized diode laser is the zeroth order or reflected beam which is desired to leave the grating at  $45^\circ$ , thus for the 860 nm laser a grating with 1600 lines per mm was used.

The laser emits 50 mW of single-mode radiation at 860 nm, which is sent through two optical diodes<sup>30</sup> to suppress feedback. An anamorphic prism pair gives the elliptical beam a round shape, and finally about 33 mW are coupled into an optical buildup cavity that contains a nonlinear crystal.

### 4.5.2 Frequency doubler

Like in the production of 423 nm light the nonlinear process of SHG is again exploited, but here the original KNbO<sub>3</sub>-crystal is used instead of an LBO crystal. KNbO<sub>3</sub> is a good choice in this case since only a small intensity from a diode laser is sent through the crystal, far from the 1600 mW as supplied by the Ti:sapphire laser to the LBO. The light reflected from the cavity is monitored by a fast photo diode and partially sent to a lambda meter to determine the laser wavelength. The photo diode is part of a Pound-Drever-Hall lock as illustrated in figure 4.19. The required sidebands for this FM-modulation technique [12] are added to the laser output by modulation of the laser diode current. An active temperature stabilization keeps the crystal temperature within less than 10 mK from the

---

<sup>29</sup>see also section 4.7

<sup>30</sup>Faraday isolators by Electro Optics Technology (EOT) and Gsänger, 30 dB each



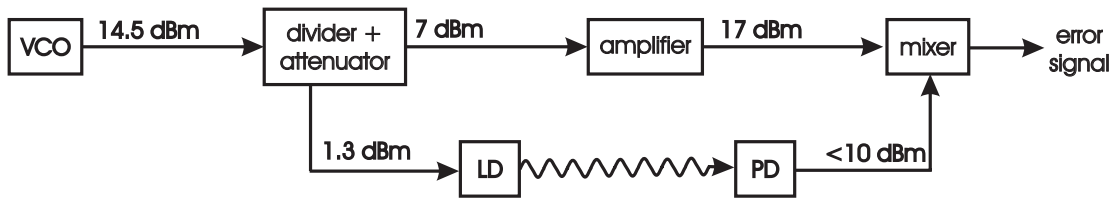


**Figure 4.19:** Pound-Drever-Hall lock, keeping the  $\text{KNbO}_3$  doubling cavity in resonance with the 860 nm diode laser

phase matching temperature of about 27°C. The output power at 430 nm typically ranges from 5 to 6 mW.

## 4.6 Spectroscopy of calcium in gas discharge lamps

The wavelengths of all lasers in our experiment can be determined by a *lambda-meter* (see appendix C.3). However, in order to set the wavelengths to their precise values and to keep the lasers locked at these wavelengths an atomic reference is necessary. One possibility is to do spectroscopy on a small thermal beam as described in section 4.3.5 for the 423 nm laser. Unfortunately the concentration of metastable calcium atoms in  $^3\text{P}_2$  as needed for the transitions at 1978 nm and 430 nm is far too low in a thermal beam to detect their resonance fluorescence. Another approach uses a hollow cathode lamp and is called *optogalvanic spectroscopy* [67, 8].

Hollow cathode lamps are commercially available for all elements. Their cathode consists of the material under investigation which partially evaporates in the discharge and fluoresces due to the excitation by collisions with electrons. The gas discharge is enabled by a background buffer gas like neon or argon. Our calcium lamp provides a calibrated intensity of the strongest transition at 423 nm. In reverse, the lamp can be used to do spectroscopy on the evaporated calcium atoms by shining in a laser scanned in wavelength around the atomic resonance and recording the lamp's impedance change due to the altered polarization on resonance, see figure C.7. Due to the low signal level the application of a lock-in amplifier is required, and therefore the laser beam intensity is modulated with a mechanical chopper<sup>31</sup>. As a result, the calcium lines at 423 nm and 1978 nm can be found, as well as even narrower lines as shown in table 4.8. Since the calcium line at 1978 nm has

wavemeter reading	transition	$\gamma$	$P_{\text{laser}}$
1950.5740 nm	$^3\text{P}_1-^3\text{D}_1$	24.9 kHz	21 mW
1986.2194 nm	$^3\text{P}_2-^3\text{D}_2$	14.12 kHz	13 mW

**Table 4.8:** Examples of narrow, far infrared calcium lines observed with the hollow cathode lamp (lock-in sensitivity 500  $\mu\text{V}$ ).

a width of 60 kHz it is necessary to achieve a narrower spectroscopy signal to lock the laser

<sup>31</sup>Opto-mechanical chopper Thorlabs MC1000; TTL input or output, 20–1000 Hz (10 slot blade), 30–1500 Hz (15 slot blade), 60–3000 Hz (30 slot blade)

to the atomic transition. This can be achieved with Doppler free saturation spectroscopy. For this purpose we built our own calcium discharge lamp which features

- optical access through two opposing windows
- high adjustable calcium partial pressure due to heated reservoir<sup>32</sup>
- population of the metastable state (and all others) by an electric discharge with neon buffer gas<sup>33</sup>

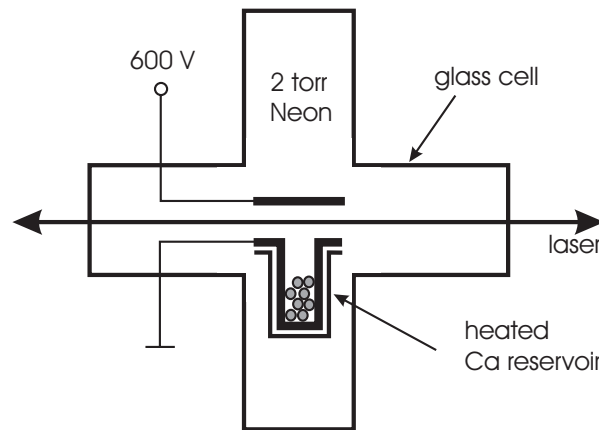


**Figure 4.20:** *Schematic of the calcium discharge lamp*

Figure 4.20 shows a schematic of the lamp. Using this lamp in a polarization spectroscopy setup (see figure 4.21, and [33, pp. 301–310]) allows to lock the Tm:YAG laser to the 1978 nm calcium line. A nearly identical setup around the same lamp locks the 430 nm light to the respective atomic transition: this spectroscopy signal is given as an error signal to a feedback circuit that turns the diode laser grating to keep the wavelength on resonance with the atomic line. Not shown in the graph are the magnetic field coils on the glass cell axis that allow to remove the Zeeman degeneracy to shift the error signal slightly away from resonance. The obtained saturation signal is described in figure 7.1.

In order to find out whether the calcium reservoir has been sufficiently heated one can apply the 430 nm laser to check the concentration of metastable atoms via the blue fluorescence. The presence of scanned 430 nm light only slightly distorts the  $2\mu$ -saturation spectroscopy signal and vice versa. The effect vanishes once the lasers are locked. Also, when a sufficiently high calcium vapor pressure is reached the color of the discharge changes from its original orange (due to neon) to a hue of violet because of the additional blue fluorescence stemming from collisionally excited atoms which decay radiatively from  $^1P_1$  back to the ground state emitting 423 nm photons.

In a second version of the lamp<sup>34</sup> several improvements have been realized:

<sup>32</sup>stainless steel container inside a ceramic cylinder with machined grooves accepting a  $\varnothing 0.25$  mm tantalum wire, see figure C.2 for oven characteristics

<sup>33</sup>current  $\approx 10$  mA at 600 V

<sup>34</sup>operating parameters: max. 2 A at  $\approx 15$  Vdc, discharge voltage min. 250 V, typ. 500 V

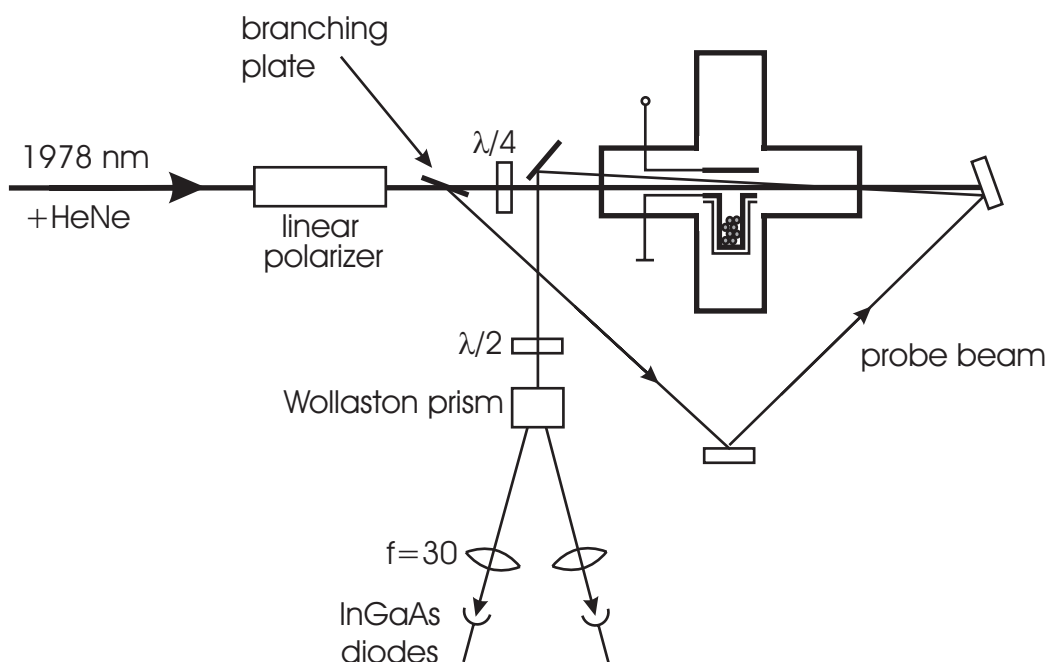


**Figure 4.21:** Saturation spectroscopy setup for the 1978 nm line

1. Minimizing the electrode distance (now less than 20 mm) allows to use a low sparking potential of only 200 V.
2. The oven exit is closer to the laser beam than before, yielding an equivalent effective calcium pressure at a lower oven temperature.
3. A larger glass cell diameter in the oven vicinity ( $\varnothing$  25 mm  $\rightarrow$   $\varnothing$  50 mm) results in less heating and therefore less stress of the wall.

## 4.7 A stabilized diode laser for 657 nm

This laser system with its stabilization to a ultrahigh-finesse resonator is characterized in great detail in [107, 108, 104]. It also attracted commercial interest: the industry magazine Laser Focus World published an article on the laser [121].

### 4.7.1 Components

The emission source is a grating<sup>35</sup> stabilized external cavity diode laser [103] like the laser for 860 nm described on page 64. A photograph of the diode laser setup is shown in figure 4.22: the large angled mount in the center of the picture carries the holographic *grating*, the laser diode is located in the larger vertical block on the right, and between them, a smaller block contains a collimating lens. These three elements are attached to a horizontal mount

<sup>35</sup>optimum grating (657 nm): 2153 lines/mm; commercially available: 2200 lines/mm, Carl-Zeiss, Jena

which rests on a peltier element. This allows in combination with a temperature sensor (not shown) to stabilize the temperature of the whole setup to within less than 10 mK.

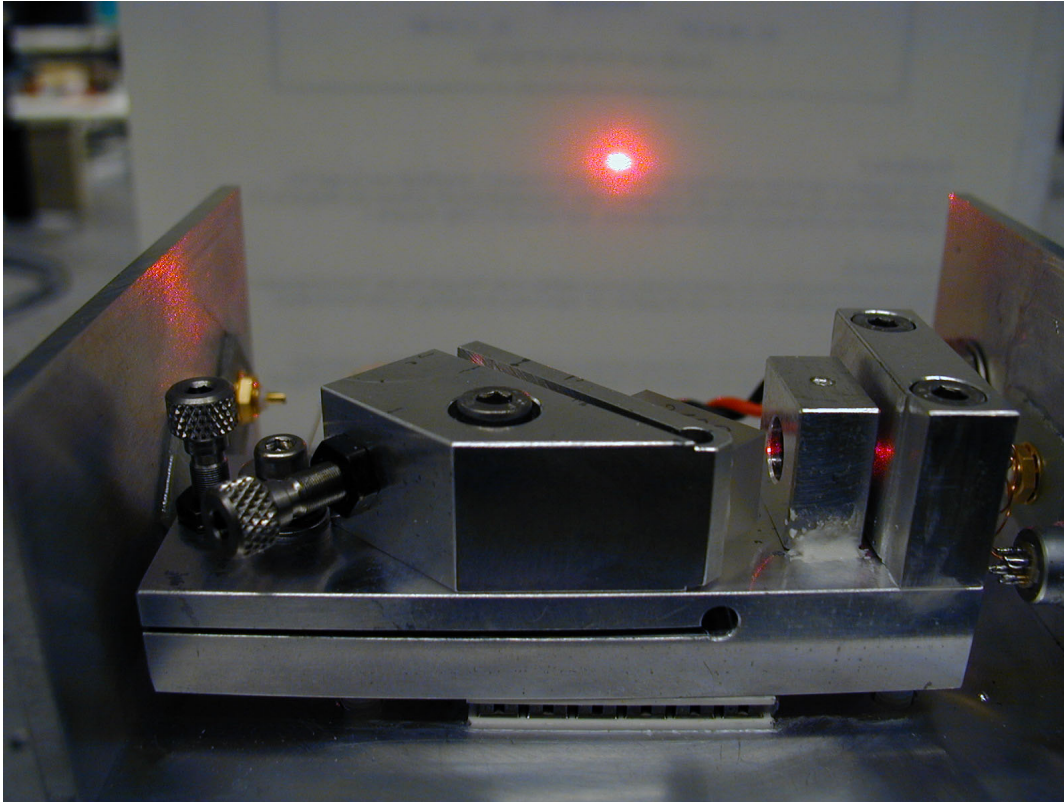


**Figure 4.22:** *Photograph of the diode laser setup (approx. scale 1:1).*

A part of the output beam is split off and sent to a stabilization setup that incorporates an ultrahigh finesse resonator and feedback electronics, see figure 4.23. The laser is stabilized by the Pound-Drever-Hall method (see page 53) using an EOM which adds low modulation index sidebands at 40 MHz away from the carrier to the laser beam. An AOM is double-passed to allow for arbitrary frequency shifts of the main laser output relative to the resonances of the stabilizing resonator. This ultrahigh-finesse resonator is made up of two super-mirrors<sup>36</sup> that were optically contacted under clean-room conditions<sup>37</sup> to a cylindrical spacer of ultra-low-expansion (ULE) glass.

## 4.7.2 Output mode

The beam diameter is measured with a beam scanner (see section 4.2) and also using a combination of a power meter with a razor blade that scans across the beam and thus cuts away a defined portion of the passing intensity. Since the laser beam has a Gaussian

<sup>36</sup>rest-reflection 1 ppm

<sup>37</sup>We appreciate that suitable facilities were made available to us by the Wiesendanger Group, Inst. for Applied Physics, Hamburg.

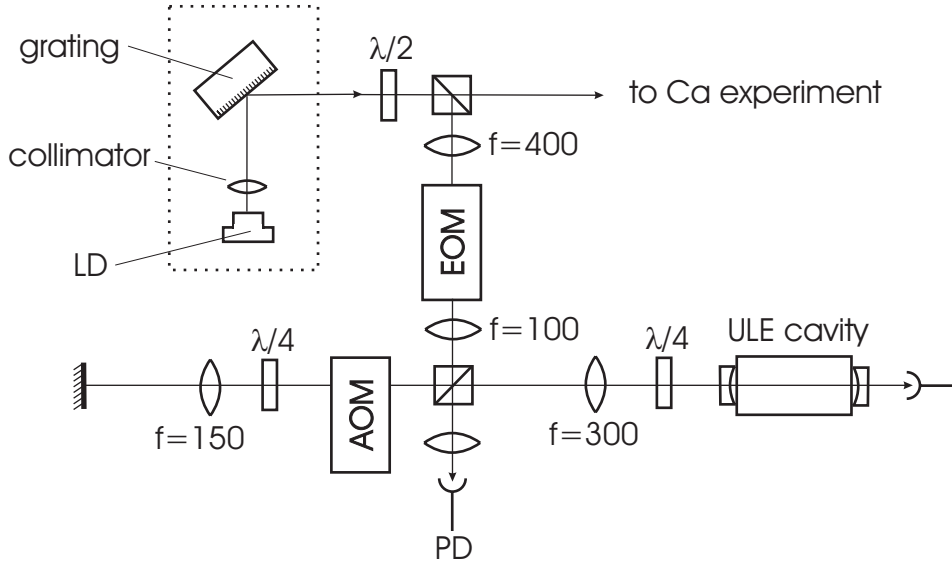


**Figure 4.23:** Optical components of the 657 nm laser system including stabilization

intensity distribution

$$I(x, y) = I_0 e^{-\frac{2(x^2+y^2)}{w^2}}$$

the measured light intensities behind the blade depend on the blade position  $x$  as

$$M(x) = \int_{-\infty}^x \int_{-\infty}^{\infty} I(x, y) dy dx = I_0' \int_{-\infty}^x e^{-2t^2/w^2} dt.$$

When the data is fitted with the Gaussian error integral

$$\Phi(x) = \frac{1}{\sqrt{2\pi}} \int_{-\infty}^x e^{-t^2/2} dt \approx \frac{1}{\sigma \sqrt{2\pi}} \int_{-\infty}^x e^{-t^2/(2\sigma^2)} dt$$

the beam width is found from  $w = 2\sigma$ .

### 4.7.3 Spectroscopy of the atomic transition

Commonly one expects to pre-stabilize a laser and then to lock it to the respective atomic line. In the case of the 657 nm laser both tasks are of higher complexity as usual since the intercombination line has a natural linewidth of only 0.4 kHz. Nevertheless, the Bergquist group stabilized with great efforts visible lasers to subhertz linewidths [126].

The red laser at 657 nm will be crucial for resolved sideband cooling as described in the last chapter. We applied it to calcium once to resolve the intercombination line: the GS-trap was loaded, the red laser slowly scanned, and its effect on the GS-population was monitored by recording the fluorescence at 423 nm. Chopping the red laser and using a lock-in amplifier we were able to find the strongly Zeeman and Doppler broadened line.

The lock-in signal<sup>38</sup> is shown in figure 4.24. Comparison with a synchronously recorded Fabry-Perot spectrum<sup>39</sup> calibrates the frequency axis, so that we find on average a calcium resonance width of 36 MHz. This large value compared to the natural linewidth results from the Doppler width of the ensemble at a temperature of a few milliKelvin and from the varying Zeeman shifts, as we couldn't switch off the magnetic field gradient at that time. During the experiment the 657 nm laser was only prestabilized but not locked to the high finesse cavity which still ensures a laser stability in the range of a few hundred kHz.

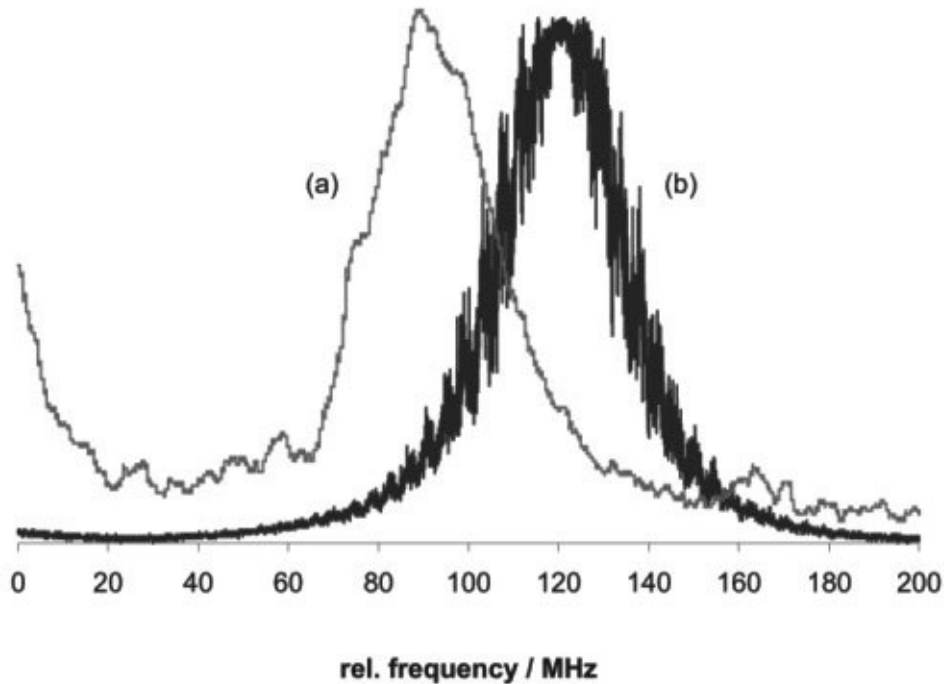


**Figure 4.24:** (a) PMT / lock-in amplifier signal of 423 nm fluorescence from the GS-trap while scanning the 657 nm laser across the intercombination line; the width of the resonance is 36 MHz. Trace (b) shows the simultaneous scan across an etalon with known finesse and FSR

<sup>38</sup>pre time constant 10 ms, post none

<sup>39</sup>etalon #7: FSR= 2009 ± 13 MHz, finesse  $F = 54 \pm 4$

## 4.8 Detectors

*... one should trust more in observation  
than in reasoning, in the latter only and at all,  
if it is in accordance with the observations.*  
Aristoteles<sup>40</sup>

Photo detectors are the eyes of experimental physicists. In our experiment we make use of various detectors to observe light in the range from 400 up to 2000 nm. Table 4.9 gives a general comparison for several detectors of electro-magnetic radiation, while table C.13 specifies dimensions and operating parameters for the two most sensitive infrared detectors in the experiment.

Photomultiplier	160 nm — 1.0 $\mu\text{m}$
Silizium-PD	180 nm — 1.1 $\mu\text{m}$
InGaAs-PD	800 nm — 1.7 $\mu\text{m}$
PbS photo-electric cell	700 nm — 3 $\mu\text{m}$
PbSe	1 $\mu\text{m}$ — 5 $\mu\text{m}$
Pyroelectric, thermopile	200 nm — 40 $\mu\text{m}$

**Table 4.9:** *Spectral ranges of detectors*

### Detection of 657 nm light

The fluorescence light from the trap region is imaged onto a photomultiplier tube<sup>41</sup> by a series of three lenses and a mirror and filtered by two dielectric edge filters (see C.9) to strip rest light outside a range of  $\pm 10$  nm around 657 nm.

The detector time constant is analyzed in the following experiment: a laser beam at 657 nm is chopped at 400 Hz by a mechanical chopper in the focus of a 1:1-telescope ( $f = 40$  mm lenses) and then sent into the vacuum chamber in such a fashion as to scatter off its walls. No calcium atoms are in the chamber to interfere with the detection test. The time required by the chopper to switch the light intensity on and off is below 100  $\mu\text{s}$ , as a fast photo diode<sup>42</sup> confirms. The PMT signal on the scope<sup>43</sup> is shown in figure 4.25 for 1000 V and 1300 V PMT supply voltage. The PMT signal decay time constant is well below 1 ms, shorter than the decay time of the calcium line at 657 nm.

### Detection of 423 nm light

The blue fluorescence emanating from the GS-trap was observed at first with a fast amplified photodiode<sup>38</sup> which was later replaced by the PMT for the detection of 657 nm

<sup>40</sup>taken from “Belehrte Unwissenheit” I 11, p.17

<sup>41</sup>Hamamatsu R928, see D

<sup>42</sup>EG&G FFD-100, rise time 1 ns

<sup>43</sup>impedance 1  $\text{M}\Omega$

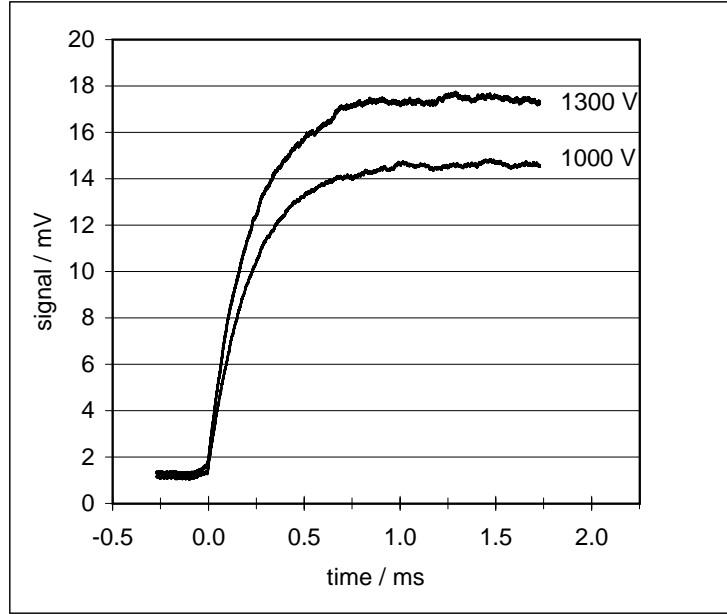


**Figure 4.25:** *PMT response to application of light at 657 nm for two multiplier voltages*

fluorescence. The red fluorescence of the GS-MOT is proportional to the blue fluorescence in steady-state, and thus a direct observation of 423 nm became redundant in this aspect.

However, to perform a time-of-flight (TOF) measurement with the light carpet method (see section 7.3.2), the detection of 423 nm returns as a prerequisite. This time the requirements are more stringent since the signal is very faint: a PMT<sup>44</sup> has to be used instead of a photo diode to increase the gain, and it has to be gated, e.g. the sensitivity has to be altered rapidly because during the trap loading the trapped atoms produce blue fluorescence photons at a high rate, whereas the ultracold atoms transferred from the metastable trap scatter only a small number of blue photons during their fall through the thin light carpet. The change in PMT gain is realized by gating the high voltage applied to the multiplier.

Two important values characterizing a PMT are the detection limit and the equivalent noise input (ENI) which are estimated for our tubes as

$$\text{Detection Limit} = \frac{\text{dark current}}{\text{rad. sens.}} = \frac{I_{\text{dark}}}{R} = \frac{3 \text{ nA}}{7.4 \cdot 10^5 \text{ A/W}} = 4 \cdot 10^{-15} \text{ W} \quad (4.23)$$

and

$$\begin{aligned} \text{ENI} &= \frac{1}{R} \sqrt{2q I_{\text{dark}} \mu \Delta f} \\ &= \frac{(2 \cdot 1.6 \cdot 10^{-19} \text{ C} \cdot 3 \text{ nA} \cdot 10^7 \cdot 1 \text{ Hz})^{1/2}}{7.4 \cdot 10^5 \text{ A/W}} = 1.3 \cdot 10^{-16} \text{ W}. \end{aligned} \quad (4.24)$$

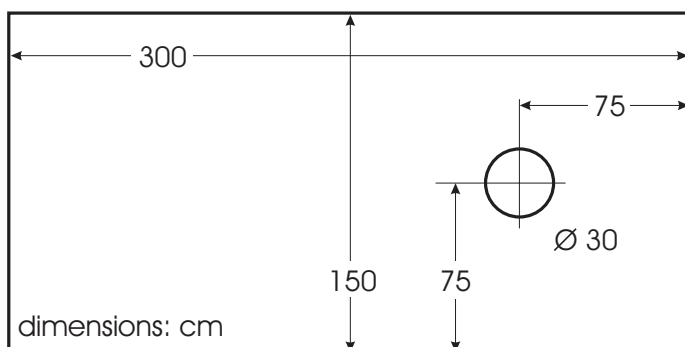
with the gain  $\mu$ . The value of the detection limit will be compared on page 107 to the expected fluorescence intensity in a time-of-flight measurement.

---

<sup>44</sup>also Hamamatsu R928



## 4.9 The optical table



The available space for optical components used in the experiment is limited by the optical table dimensions of 300 by 150 cm (20.2 cm thick). It features a large off-center hole of 30 cm diameter whose center is located at 75 cm from the edge.

This allows to place the vacuum system in the middle of the table and to directly connect to the pumps below without the need to lead vacuum connections around the table edges. This saves valuable table surface along the easily accessible edges. Another successful space conserving strategy is to place the pump laser heads of the VERDI laser systems (see section 4.2.3 and appendix D) on the bottom side of the table. The maximum allowed pulling force downwards perpendicular to the table is  $1.4 \cdot 10^6 \text{ N/m}^2$  according to the manufacturer Coherent. The weight of the laser head is 22.8 kg, and the footage is  $0.069 \text{ m}^2$ . The resulting downward force of  $3242 \text{ N/m}^2 \ll 10^6 \text{ N/m}^2$  is well below the maximum allowed value, and thus both Verdi's laser heads were bolted to the lower side of the table, and the light beams were sent onto the tabletop using a set of dielectric mirrors inside rigid square aluminum profiles attached to the short side of the table. The general height of the laser beams over the table surface is set to 15.4 cm in order to send some beams directly into the main vacuum chamber without any lifts.

# Chapter 5

## Deceleration of an atomic beam

*The force caused by radiation,  
particularly by light at or near the resonance frequencies of atomic transitions,  
originates from the momentum associated with light. ...  
Multiple absorptions can be used to produce a large total velocity change*  
[86, p.73]

After having described the more technical requirements of the vacuum and laser systems this chapter will bring us closer to the physics of the experiment — laser cooling. The first cooling stage or *precooling* is given in this experiment by slowing down a thermal beam of hot atoms by counterpropagating laser light.

### 5.1 How to slow atoms using laser light

A photon possesses a momentum of  $\mathbf{p} = \hbar \mathbf{k}$ . The absolute value of  $p$  is  $h/\lambda$ , where  $\lambda$  is the wavelength of the laser. In principle, laser cooling uses the fact that all photons in a laser beam shining on atoms have a similar  $\mathbf{k}$ -vector, e.g. they all come from the same direction, whereas spontaneously scattered photons show a random distribution, since the spontaneous emission process is strictly isotropic. Once an atom absorbs a photon in a scattering event, it acquires a small change in momentum and during the emission again, but in a random direction. After many scattering events the momentum change of a single atom due to emissions averages out to zero, but the change due to absorptions will have added up substantially since all impinging photons come from the same direction. This results in an overall deceleration of the atom if the initial atomic propagation was opposite to the direction of the laser beam.

The acceleration  $a$  inside an atomic beam slower is given by the product of the momentum transfer onto an atom due to one absorbed photon  $\frac{\hbar k}{m}$ , the rate of excitation, and the probability of excitation which depends on the laser intensity  $I$  and detuning  $\delta$ . The probability of excitation scales as

$$\Pi_{\uparrow} = \frac{1}{2} \frac{S}{1+S} \quad (5.1)$$

where the saturation is

$$S = \frac{1}{2} \frac{\Omega^2}{\delta^2 + (\Gamma/2)^2}. \quad (5.2)$$

The Rabi frequency  $\Omega$  relates the laser intensity to the saturation intensity  $I_S$  as

$$S(\delta = 0) = 2 \left( \frac{\Omega}{\Gamma} \right)^2 \stackrel{\text{def}}{=} \frac{I}{I_S}. \quad (5.3)$$

The saturation intensity depends on the transition wavelength and the excited state lifetime – for the main  $^{40}\text{Ca}$  line at 423 nm it is

$$I_S = \frac{\pi \hbar c}{3\lambda^3 \tau} = 59.9 \frac{\text{mW}}{\text{cm}^2}. \quad (5.4)$$

The maximum probability of excitation is found when the laser is tuned to resonance, and thus  $\delta = 0$ . The maximum possible rate of excitation is  $\Gamma/2$  since no more than half the population can be transferred into the excited state. The highest possible acceleration is therefore

$$a_{\text{max}} = \frac{\hbar k}{m} \cdot \frac{\Gamma}{2} \cdot \frac{I/I_S}{1 + I/I_S}, \quad (5.5)$$

where the applied wavelength  $\lambda$  appears in the wavevector  $k = \frac{2\pi}{\lambda}$ ,  $\Gamma$  is the linewidth of the transition, and  $m$  the atomic mass. The power scattered by an atom in the laser beam is

$$P = \hbar\omega_L \Gamma \Pi_{\uparrow} = \hbar\omega_L \frac{\Gamma}{2} \frac{\Omega^2/2}{\delta^2 + \Omega^2/2 + (\Gamma/2)^2}, \quad (5.6)$$

which is the energy of one scattered photon times the scattering rate given by the spontaneous emission lifetime times the probability of a scattering event given in eqn. (5.1). The velocity of an atom travelling down the slower is

$$v(t) = v_i - at \quad (5.7)$$

if we assume a constant deceleration  $a$ . The distance travelled is then

$$s(t) = v_i t - \frac{1}{2} at^2. \quad (5.8)$$

This can be summed up in the relation

$$\frac{v}{v_i} = \left( 1 - \frac{s}{s_i} \right)^{1/2}. \quad (5.9)$$

The necessary distance  $s$  to slow atoms to zero velocity is calculated as

$$v(t) = 0 \quad \Rightarrow \quad t = \frac{v_i}{a} \quad (5.10)$$

$$\text{therefore } s = \frac{v_i^2}{2a}. \quad (5.11)$$

When the atoms are decelerating they are tuned out of resonance with the slowing laser. To cancel this Doppler effect one can chirp the laser frequency or change the transition

frequency within the atoms, which can be achieved using the Zeeman effect. An applied magnetic field will shift both involved levels of the transition used, therefore the difference in these shifts has to cancel the Doppler shift at every moment during the slowing process:

$$k v = \Delta g \Delta m \frac{\mu_B}{\hbar} B. \quad (5.12)$$

For the 423 nm line in calcium the g-factor  $g = 1$  and  $\Delta m = 1$ ,  $\mu_B$  is the Bohr magneton, and  $B$  the magnetic field. Again, two possible strategies arise — either the whole magnetic field is adjusted in time to fit the decreasing velocity of only one bunch of atoms, or the magnetic field is tailored in space such that all decelerating atoms always experience just the suitable magnetic field along the slowing path. This is true if the magnetic field shows the same dependence on slowing distance as the velocity in equation (5.9). The initial magnetic field should be

$$B_i = \frac{k v_i}{\mu_B / \hbar} = 2 \times 10^3 \text{ Gauss} \quad (5.13)$$

for an initial velocity  $v_i = 1200$  m/s. The lineshift due to the magnetic field is

$$\delta\omega = \pm \frac{\mu_B B}{\hbar} = 1.4 \times 10^{10} \frac{\text{Hz}}{\text{Tesla}} B \quad (5.14)$$

where 1 Tesla =  $10^4$  Gauss and  $+(-)$  is valid for  $\sigma_+$ -light ( $\sigma_-$ -light). At a constant deceleration  $a$  the required magnetic field along the slowing axis and z-direction is

$$B(z) = B_0 \sqrt{1 - 2az/v_0^2} - B_{\text{offset}}. \quad (5.15)$$

Typical values at  $v_0 = 1000$  m/s and  $B_0 = 0.17$  Tesla are:

$$\begin{aligned} \text{maximum deceleration} \quad a_{\text{max}} &= \frac{\hbar\omega}{2mc\tau} = 2.5 \cdot 10^6 \text{ m/s}^2 \\ \text{minimum total slowing time} \quad t_{\text{min}} &= \frac{v_0}{a_{\text{max}}} = 0.4 \text{ ms} \\ \text{minimum slower length} \quad L_{\text{min}} &= \frac{1}{2} v_0 t_{\text{min}} = 20 \text{ cm} \end{aligned}$$

## 5.2 Transverse heating

The Zeeman slower decreases atomic velocities only in the one dimension along the slower axis. The momentum changes due to the spontaneous emissions average to zero as we said, but they lead to diffusion and therefore to an increased transverse temperature of the atomic beam. We analyze this effect by following a single atom along its way through the slower.

The travelled distance in the slower until the atom gets into resonance with the slowing laser is given by

$$s = s_0 \left( 1 - \left( \frac{v_i}{v_0} \right)^2 \right), \quad (5.16)$$

where  $s_0$  is the length of the slower,  $v_i$  the initial atomic velocity, and  $v_0$  the designed maximum velocity that can be slowed. For a constant deceleration  $a$  the total time spent inside the slower is

$$t_i = \frac{s_i}{v_i} + \frac{v_i}{a}. \quad (5.17)$$

With the initial transverse velocity  $v_{T,i}$  and the ratio  $\alpha_i = v_{T,i}/v_i$  the transverse excursion  $\delta x_i$  is limited by the radius of the vacuum tubing  $r$  as

$$\alpha_i s_0 < \delta x_i < \alpha_i 2s_0 < r \quad (5.18)$$

$$\text{or } \alpha_i < \frac{r}{2s_0}. \quad (5.19)$$

Due to spontaneous emission the transverse heating is given for the isotropic case by

$$\delta v_T \approx \sqrt{\frac{N}{3}} v_z, \quad (5.20)$$

where  $N$  is the number of absorption / emission cycles. For the present case of dipole radiation the dependance slightly changes to

$$\delta v_T \approx \sqrt{\frac{2}{5}} N v_z. \quad (5.21)$$

Since on the order of 30000 cycles are necessary to bring the atoms close to rest, the total amount of transverse heating is

$$\delta v_T \approx 2.2 \text{ m/s}, \quad (5.22)$$

which is to be compared to the capture velocity<sup>1</sup> of the trap  $v_c = 14.6 \text{ m/s}$  and the minimum attainable longitudinal temperature in precooling on the main transition, see table 6.1.

### 5.3 Calculation of the current distribution for the Zeeman slower field

The magnetic field on the axis of the solenoid was calculated analytically while the off-axial properties were studied numerically. The magnetic field strength on the rotational symmetry axis at a distance  $z$  from a single loop of current  $I$  with radius  $r$  is given by

$$H(z) = -\frac{I}{2\pi} \int_S \frac{\mathbf{r} \times d\mathbf{r}}{r^3} = \frac{2\pi I r^2}{4\pi z^3}, \quad (5.23)$$

as long as  $r \ll z$ . The magnetic induction  $B$  follows with  $B = \mu_0 \mu H$  as

$$B(z) = \frac{\mu_0 I r^2}{2z^3}. \quad (5.24)$$

Biot-Savart's law allows to calculate the field of a current loop as

$$|d\mathbf{B}| = \frac{\mu_0}{4\pi} \cdot \frac{I |d\mathbf{l} \times \mathbf{r}/r|}{r^2} = \frac{\mu_0}{4\pi} \frac{I dl}{x^2 + R^2} \quad (5.25)$$

$$dB_x = dB \sin \theta = dB \frac{R}{\sqrt{x^2 + R^2}} = \frac{\mu_0}{4\pi} \cdot \frac{I dl}{x^2 + R^2} \cdot \frac{R}{\sqrt{x^2 + R^2}} \quad (5.26)$$

$$B_x = \oint dB_x = \frac{\mu_0}{4\pi} \cdot \frac{IR}{(x^2 + R^2)^{3/2}} \oint dl = \frac{\mu_0 IR^2}{2(x^2 + R^2)^{3/2}} \quad (5.27)$$

$$(5.28)$$

---

<sup>1</sup>see (6.18) on page 84

A solenoid with  $N$  turns can be decomposed into  $N$  loops next to each other:

$$B_x = \frac{\mu_0}{4\pi} 2\pi n I R^2 \int_{-a}^b \frac{dx}{(x^2 + R^2)^{3/2}} = \mu_0 n I \left[ \frac{b}{\sqrt{b^2 + R^2}} + \frac{a}{\sqrt{a^2 + R^2}} \right], \quad (5.29)$$

where  $n = N/(a + b)$  is the density of turns. After a coordinate change placing the origin at one end of the coil and thus  $b = L - x$ , where  $L$  is the length of the solenoid, the total field is

$$B_x(x) = \frac{\mu_0}{2} \frac{nI}{R} \left[ \frac{x}{\sqrt{(x/R)^2 + 1}} - \frac{x - L}{\sqrt{1 + \left(\frac{x-L}{R}\right)^2}} \right]. \quad (5.30)$$

The equation for the numerically derived solution using a computer program is then

$$B = B_0 \frac{a_1}{e} \sum_{i=1}^{12} \frac{1}{a_i} \left[ \frac{x}{1 + \sqrt{(x/a_i)^2 + 1}} - \frac{x - a[i]e}{\sqrt{1 + \left(\frac{x - a[i]e}{a_i}\right)^2}} \right], \quad (5.31)$$

where  $a_i$  are the radii and  $a[i]$  the lengths of the  $i$ -th layer of windings,  $B_0$  is the magnetic field in the center of a unit coil with radius 10 mm, and  $e$  is the wire thickness. The fit parameters finally used to build the slower are summarized in tables 5.1 and 5.2. In this fit the max. field per turn due to the first layer is 3.7855 Gauss, thus the current should be  $I = 2rB/\mu_0 = 7.8$  Ampere. The wire diameter is 1 mm and the total length of the wire for the slower coil is 148.9 m. Since the specific resistance is  $\rho = 0.0223 \Omega/\text{m}$ , the total resistance at room temperature is 3.32  $\Omega$ , and hence the required power and voltage are  $P = RI^2 = 204$  Watt at  $U = 25.9$  Volt.

layer-#	1	2	3	4	5	6	7	8	9	10	11	12
length	222	221	203	184	162	137	109	77	45	19	19	16
radius	13	14	15	16	17	18	19	20	21	22	23	24
position	13	14	15	16	17	18	19	20	21	22	23	24

**Table 5.1:** Fit parameters for the length and radius of the slower solenoid layers (in mm)

The fit already includes two additional magnet coils placed behind the exit of the slower: the first coil — the “outcoupling coil” — pulls the magnetic field at the slower exit below zero (reverses the field direction) to decouple the atoms from the laser field. The slowing process is thus aborted at a well defined final atomic velocity since it is not desired to bring atoms to a complete halt at the slower exit or to even accelerate them back towards the oven. The second coil — the “compensation” coil — is necessary to again reverse the axial field in order to bring the field to zero quickly. This avoids an influence of the previous coils on the magnetic field in the trap region. The  $z$ -axis is positive in the flight direction of the atoms and has its zero at the start of the slowing process which occurs at 31 mm behind the slower entrance.

	position z [mm]	radius [mm]	max. field [G]
slower	-31.0	13 – 24	850
outcoupler	220	29	-160
compensation	249	29	40

**Table 5.2:** *Fit parameters for the positions and strengths of the magnet coils*

## 5.4 Inductivity of the slower solenoid

The effect of an inductive load on an electrical network with voltage supply  $U$  can be analyzed with the differential equation for the voltages  $U - RI - L \frac{\delta I}{\delta t} = 0$ , where  $R$  is an ohmic load in parallel to an inductivity  $L$ . There are two solutions corresponding to switching the current on or off:  $I_{on}(t) = I_0 (1 - e^{-t/\tau})$  and  $I_{off}(t) = I_0 e^{-t/\tau}$ , where  $I_0 = U/R$  and  $\tau = L/R$ . The inductivity of a long cylindrical solenoid is calculated as follows: the voltage  $U$  depends on the number of turns and the change in magnetic flux through them as  $U = -N \frac{\delta \Phi}{\delta t}$ , and the magnetic flux is proportional to the current through the turns, thus  $\Phi = \mu A H = \mu A \frac{IN}{l}$ . The voltage  $U = -N \mu A \frac{N}{l} \frac{\delta I}{\delta t}$  is also expressed as  $U = -L \frac{\delta I}{\delta t}$  defining inductivity  $L$ , so that finally we arrive at  $L = \frac{\mu N^2 A}{l}$  where the inductivity is in Henry. For the specific case of  $l \approx 30$  cm,  $A = \pi(15\text{cm}^2)$ ,  $N \approx \frac{300 \cdot 15}{2}$ , and  $R = 3.3\Omega$ , using  $\mu = 4\pi 10^{-7}$  (Vs/Am), the resulting inductivity is  $L = 3.3 \cdot 10^{-4}$  Henry. The characteristic time constant  $\tau \approx 10^{-4}$  s. To stay below 1 ms it is necessary to keep  $R \geq 0.3\Omega$ .

## 5.5 Choosing the right power supply

To obtain the required magnetic field of 3.7855 Gauss per solenoid turn we calculated the required current  $I = 7.8$  A and voltage  $U = 25.9$  V assuming  $R = 3.32\Omega$ , but how about the required stability of these values? Fluctuations will influence the Zeeman shift due to the magnetic field change as seen in (5.12). To keep the atoms within one linewidth from resonance we demand  $\Delta\nu < \Gamma_{nat}$ , and with (5.14) we get

$$\Delta B < 34.6 \text{ MHz} \cdot \left[ \left( 1.4 \times 10^{10} \frac{\text{Hz}}{\text{Tesla}} \right) \cdot \left( 10^{-4} \frac{\text{Tesla}}{\text{Gauss}} \right) \right]^{-1} = 25 \text{ Gauss}. \quad (5.32)$$

With a maximum absolute value of the magnetic field in the slower of about  $10^3$  Gauss the largest allowed fluctuation of the voltage is then  $1000/25 = 2.5\%$  which is the required level of power supply stability. A suitable supply was found in Elektro-Automatik's model EA-PS 2016-100 (max. 10 A, 16 V). To boost the available voltage a fixed voltage 12V/100W power supply was added in series to the first. For the required 7.8 A a voltage of 37 V had to be applied under cooling with tap water.

## 5.6 Test of the experimentally realized Zeeman slower magnetic field

Before the turns of the slower solenoid were permanently fixed with glue<sup>2</sup> the magnetic field  $B_z$  was tested using a Teslameter with an axial Hall probe<sup>3</sup>. The measurement range was 0 to 20 mT, accuracy 0.01 mT, and the instrument was nulled at the slower exit vacuum flange when the current was switched off. The results for 2 A / 9 V without cooling are shown in figure 5.1. Since no cooling was possible at the time of measurement even the

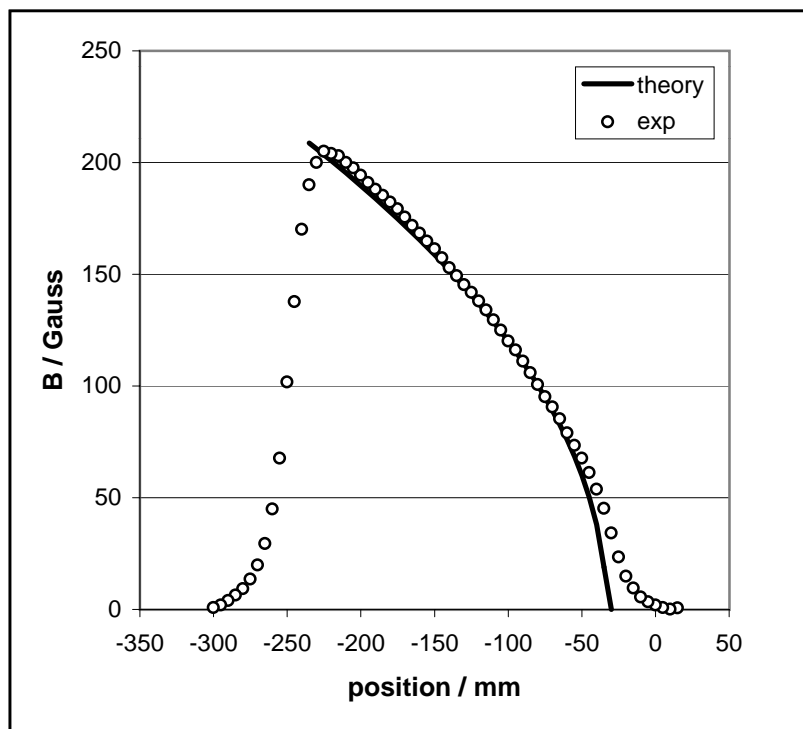


Figure 5.1: Axial magnetic slower field shape

low dissipated power of less than 20 Watt slowly increased the temperature of the solenoid and decreased the current such that the magnetic field at position  $z = -100$  mm decreased exponentially from 117 to 115 Gauss with a time constant of 6 minutes. This had no significant effect on the results since the total measurement time was less than one minute.

After installation of the Zeeman slower to the vacuum chamber it was attached to a tap water supply to keep it at room temperature under operation. The water is sent through a copper tube wrapped around the outer layer of the slower and through the inside of the slower, between two concentric tubes. The water flows between the vacuum tubing wall and a second, outer tube which carries the windings of the Zeeman slower magnet.

<sup>2</sup>WEPOX Gießharz GT7012 (two-component-glue) of Fa. Peters, 02152-2009-0,fax-70

<sup>3</sup>PHYWE (from student workshop) with probe heads 13610.93 and .01



# Chapter 6

## Trapping neutral atoms in magneto-optical traps

### 6.1 Principle of operation

The first experimental demonstration of a magneto-optical trap (MOT) for neutral atoms occurred in 1987 by Chu [100, 22]. Prior to this invention it was only possible to trap ionized atoms in electric fields. Laser cooling [51] was known for both ions and neutral atoms [23], but in order to tightly confine neutral atoms a spatially inhomogeneous force had to be created. Actually, according to the *optical Earnshaw-Theorem* a trap in three dimensions cannot be constructed using the radiation pressure of laser beam with spatially constant polarization. Nevertheless such a trap can be realized if a spatial dependence of the polarizability is introduced. This can be achieved by laser cooling with six red detuned laser beams in combination with a non-uniform magnetic field that creates the required spatial inhomogeneity.

The scattering force [28, 118, 86] of a single laser beam interacting with a cloud of neutral atoms is

$$F_{\text{scat}} = \hbar k \frac{\Gamma}{2} \frac{\Omega^2/2}{\delta^2 + \Omega^2 + \Gamma^2/4} \quad (6.1)$$

with the Rabi frequency  $\Omega$  and the detuning  $\delta = \omega - \omega_0$ . In a MOT one uses three pairs of counterpropagating laser beams with opposite circular polarization, e.g.,  $\sigma_+$  light from one and  $\sigma_-$  light from the opposite direction. The beams propagate on three orthogonal axes and intersect at the field minimum of a magnetic quadrupole field which is created by two coils in anti-Helmholtz configuration, see figure 6.1 (a). An atom approaching, e.g., from the left passes through the trap until the increasing Zeeman effect shifts it into resonance with the  $\sigma_-$  laser from the right, see figure 6.1 (b). Since the laser is red detuned by one linewidth resting atoms in the center of the trap do not interact with the laser. However, moving atoms are Doppler shifted into resonance due to their rest velocity and thus experience strong interaction leading to efficient cooling and trapping.

The radiation pressure imbalance and therefore the net force experienced by an atom in the combined magnetic and light field depends on the atomic velocity  $v$  and position  $z$

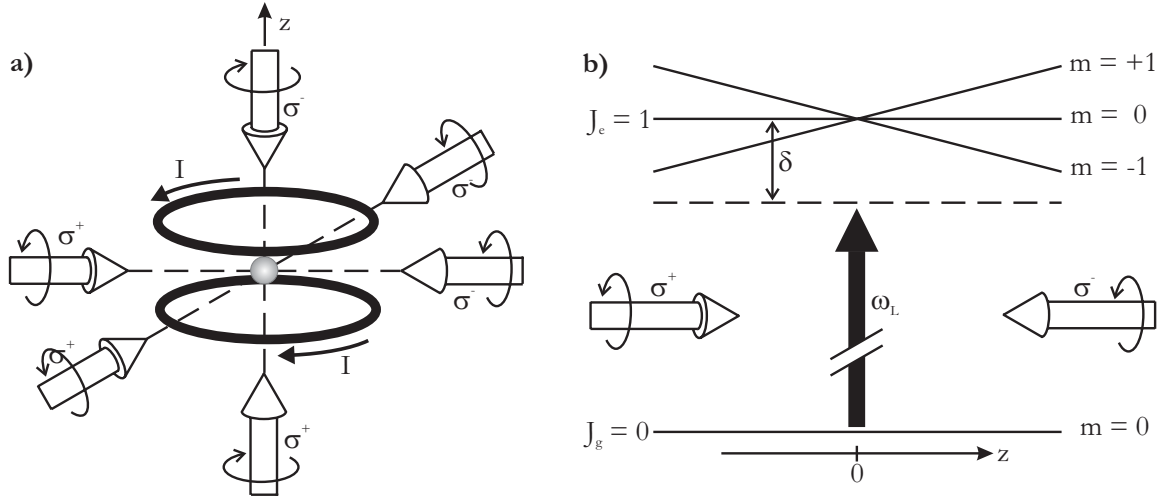


**Figure 6.1:** Operation scheme of a standard MOT: (a) shows the electric currents, that create the magnetic quadrupole field, and the laser beam directions and polarizations. (b) examines the excited state Zeeman shift of a two-level atom along one axis.

as

$$F = F_{\text{scat}} \left[ \delta = \omega - \omega_0 - kv - \frac{\mu B(z)}{\hbar} \right] - F_{\text{scat}} \left[ \delta = \omega - \omega_0 + kv + \frac{\mu B(z)}{\hbar} \right]. \quad (6.2)$$

In the trap center where  $\mu B = g\mu_B \frac{dB}{dz} z$  the force can be written as

$$F = -2 \left( kv + \frac{g\mu_B}{\hbar} \frac{dB}{dz} z \right) \frac{\partial F}{\partial \delta} \Big|_{z=0} = -\alpha v - \kappa z, \quad (6.3)$$

where  $\alpha$  is the damping constant and  $\kappa$  the spring constant of the trap. Solving this differential equation for displacements  $z(t)$  and velocities  $v = \dot{z}(t)$  results in  $z(t) = A \exp[-t/\tau]$  and  $\dot{z}(t) = -z/\tau$  with a characteristic damping time constant

$$\tau = \frac{\alpha}{\kappa} = \frac{\hbar k}{g\mu_B dB/dz} = 0.85 \text{ ms} \quad (6.4)$$

for calcium atoms in a magnetic field with a gradient of  $dB/dz = 20 \text{ G/cm}$  ( $\lambda = 423 \text{ nm}$  and  $g=1$ ). For comparison,  $\tau = 1.7 \text{ ms}$  for cesium atoms in a  $5 \text{ G/cm}$  gradient.

The force in the low velocity limit<sup>1</sup> is

$$F(v, z) = \frac{2\hbar k (2I/I_0) (2\delta/\Gamma) (kv + \beta z)}{(1 + (2\delta/\Gamma)^2)^2}, \quad (6.5)$$

and the full differential equation is

$$\ddot{z} + \gamma \dot{z} + \omega_{\text{trap}}^2 z = 0, \quad (6.6)$$

<sup>1</sup>see lecture by W. Phillips in [3]

where

$$\gamma = \frac{4\hbar k^2(I/I_0)(2\delta/\Gamma)}{M[1+(2\delta/\Gamma)^2]^2} \quad \text{and} \quad \omega_{\text{trap}}^2 = \frac{4\hbar k(I/I_0)(2\delta/\Gamma)\beta}{M[1+(2\delta/\Gamma)^2]^2}. \quad (6.7)$$

The atomic motion in a MOT is commonly strongly damped since  $\gamma^2/(4\omega_{\text{trap}}^2) \gg 1$ . The parameters  $\gamma$  and  $\omega_{\text{trap}}$  have a relative maximum at  $\Omega = \Gamma$  optimizing the laser intensity and at  $\delta = -\Gamma/2$  optimizing the laser detuning.

The damping force on atoms in a magneto-optical trap is huge as one can see from comparing the gravitational acceleration  $g$  to the acceleration due to the laser light. The power in each MOT beam of 11 mm diameter is about 30 mW, thus  $I = 29 \text{ mW/cm}^2$  and

$$S = \frac{I}{I_{\text{sat}}} \approx \frac{1}{2}. \quad (6.8)$$

According to equation (5.5) the max. acceleration in resonance will be

$$a_{\text{max,MOT}} = 8.54 \cdot 10^5 \frac{\text{m}}{\text{s}^2}. \quad (6.9)$$

## 6.2 MOT coils

As discussed, a suitable magnetic field is essential for any MOT. It is created by two magnet coils with counterpropagating electric current, which is called anti-Helmholtz configuration. The trap is located in the center of symmetry between the coils where the magnetic field vanishes. The field increases homogenously and approx. linearly from the trap center outwards. The field gradient in the trap center is

$$\left. \frac{dB}{dz} \right|_{z=0} = -\frac{3\mu I N}{2R^2} \cdot \left(\frac{4}{5}\right)^{5/2} = 1.0790 \frac{NI[\text{A}]}{R[\text{cm}]^2} \quad [\text{G/cm}] \quad (6.10)$$

for  $\Lambda = R$  and

$$\left. \frac{dB}{dz} \right|_{z=0} = 1.028 \frac{NI[\text{A}]}{R[\text{cm}]^2} \quad [\text{G/cm}] \quad (6.11)$$

for  $\Lambda = 1.25R$ , taking the derivative of equation 5.29 at  $z = 0$ . Here  $\Lambda$  is the separation of the two coils. Assuming  $R = 21 \dots 31 \text{ mm} \approx 26 \text{ mm}$ ,  $\Lambda \approx R$ , and a desired gradient of 20 G/cm one finds  $NI = 126 [\text{A}]$ .

Actually the field gradient at the trap is not isotropic — from Maxwell's equation  $\nabla \cdot B = 0$  we immediately deduce

$$\frac{dB_x}{dx} = \frac{dB_y}{dy} = -\frac{1}{2} \frac{dB_z}{dz}. \quad (6.12)$$

The inductivity has already been calculated for the Zeeman slower coil in 5.4. Here the inductivity  $L = \mu\mu_0 \frac{N^2}{l} A = 206 \text{ mH}$ , see table C.1 for dimensions.

## 6.3 Collection of atoms into the trap

### 6.3.1 Capture range

The maximum velocity up to which atoms can be captured in the trap is determined as follows: the trap laser beams are red detuned from the Bohr frequency at zero atomic velocity and zero magnetic field. The increasing magnetic field from the trap center outwards shifts atoms of decreasing velocity into resonance with laser. At a certain distance from the center the Zeeman effect shifts resting atoms into resonance. Beyond this distance, called capture radius  $R_C$ , no atoms interact with the light field. The capture range is the region of a sphere around the trap with the radius  $R_C$ . Atoms entering the capture region must have a velocity such that after passing the trap center they can be stopped before they reach the opposite side of the capture sphere. Therefore, in order to trap atoms their maximum Doppler shift is twice the Zeeman shift at the capture radius

$$k v_{\max} = 2 \cdot \beta R_C = \tilde{\delta} \tilde{\Gamma} \quad (6.13)$$

where  $\beta = dB/dz$ . We introduced the power-broadened linewidth  $\tilde{\Gamma} \equiv \Gamma \left(1 + 2 \left(\frac{\Omega}{\Gamma}\right)^2\right)^{1/2}$  and the weighted detuning  $\tilde{\delta} = \delta \left(\tilde{\Gamma}/2\right)^{-1}$ , where  $\Omega$  is the Rabi frequency as in equation (5.3). The second equation in (6.13) stems from the fact that the red detuning of the trap beams is set to one natural linewidth  $\Gamma$ . With (6.13) and (5.5) the required stopping length  $s_{\max}$  for the fastest atoms to be trapped is then

$$s_{\max} = \frac{v_{\max}^2}{2a} = \frac{\left(\tilde{\Gamma}/k\right)^2 \tilde{\delta}^2}{4\omega_{\text{rec}} \Gamma/k \left(\Omega/\tilde{\Gamma}\right)^2} = \frac{1}{4k} \frac{\tilde{\Gamma}^2}{\Gamma\omega_{\text{rec}}} \left(\frac{\tilde{\Gamma}}{\Omega}\right)^2 \tilde{\delta}^2. \quad (6.14)$$

Demanding  $s_{\max} \leq 2 R_C$  leads to a limitation for the field gradient

$$\beta \leq \beta_{\max} \equiv 2 k \omega_{\text{rec}} \frac{1}{\tilde{\delta}} \frac{\Gamma}{\tilde{\Gamma}} \left(\frac{\Omega}{\tilde{\Gamma}}\right)^2. \quad (6.15)$$

Using the calcium transition wavelength and assuming the optimum values  $\Omega = \Gamma$  and  $\delta = -\Gamma/2$  results in  $\tilde{\Gamma} = \sqrt{3}\Gamma$ ,  $\tilde{\delta} = 1/\sqrt{3}$ , and finally  $R_C = 12.4 \text{ cm}/\beta$  with  $\beta$  in Gauss/cm. With our current field gradient of 20 G/cm we find  $R_C = 6.2 \text{ mm}$ . The maximum possible acceleration which occurs at  $\Omega = \Gamma$  and  $\delta = -\Gamma/2$  is

$$a_{\max} = \frac{\hbar k \Gamma}{m} \frac{1}{4}, \quad (6.16)$$

and for the 423 nm calcium line it has the value of  $a_{\max} = 1.28 \cdot 10^6 \text{ m/s}^2$ . Since

$$\frac{dv}{dz} = \frac{1}{v} \frac{dv}{dt} = \frac{g \mu_B}{\hbar k} \frac{dB}{dz} \quad (6.17)$$

we find the capture velocity  $v_c$  using  $v = \frac{g \mu_B}{\hbar k} \frac{dB}{dz} z$  at  $z = R_c$  as

$$v_c^2 = a_{\max} R_c \quad (6.18)$$

or from (6.13) as  $v_c = \tilde{\delta} \tilde{\Gamma}/(2k)$ . With  $\Omega = \Gamma$  and  $\delta = -\Gamma/2$  it simplifies to  $v_c = \Gamma/k$ .

Several limitations restrict the cooling processes in a MOT. In Doppler cooling theory [113] a lower limit for the temperature is given since the excited state population cannot exceed 50% of the trapped atoms:

$$T_D = \frac{\hbar \Gamma}{2 k_B} \quad (6.19)$$

where  $k_B$  is the Boltzmann constant. Another fundamental limit is the recoil temperature  $T_R$ : if the momentum transfer due to an absorption of a photon brings an atom to a complete halt, the unavoidable spontaneous emission and its momentum kick of  $\Delta p = \hbar k$  leave the atom with a final velocity of at least  $\hbar k/m$  which corresponds to an energy of  $E_R = (\hbar k)^2/(2m)$  and a temperature of

$$T_R = \frac{(\hbar k)^2}{m k_B}. \quad (6.20)$$

The numerical values of the trapping parameters for both traps are summarized in table 6.1. It's important to note that the two traps connect well since the final temperature in the GS-trap matches the capture velocity of the metastable trap. The recoil limit is

	transition	$\lambda_{\text{vac}}$	$\Gamma$	$I_{\text{sat}}$		
ground-state trap	$^1\text{S}_0 \rightarrow ^1\text{P}_1$	423 nm	34.6 MHz	59.9 mW/cm <sup>2</sup>		
metastable trap	$^3\text{P}_2 \rightarrow ^3\text{D}_3$	1978 nm	57.2 kHz	0.9 $\mu\text{W}/\text{cm}^2$		
	transition	$v_c$	$v_D$	$T_D$	$T_R$	
ground-state trap	$^1\text{S}_0 \rightarrow ^1\text{P}_1$	14.6 m/s	42 cm/s	0.8 mK	2.7 $\mu\text{K}$	
metastable trap	$^3\text{P}_2 \rightarrow ^3\text{D}_3$	11.3 cm/s	1.7 cm/s	1.4 $\mu\text{K}$	122 nK	

**Table 6.1:** *Trapping parameters for the ground-state and metastable MOT: capture velocity  $v_c = \Gamma/k$ , Doppler limit velocity  $v_D = \sqrt{\hbar \Gamma/(2m)}$ , Doppler temperature  $T_D = \hbar \Gamma/(2k_B)$ , and recoil temperature  $T_R = (\hbar k)^2/(m k_B)$ . See table A.5 for more detail on transition wavelengths.*

lower than the Doppler limit for both transitions, so that it cannot be reached according to Doppler theory. However, for traps with hyperfine structure in the ground state as in the case of the metastable trap sub-Doppler cooling mechanisms allow to transcend the Doppler limit and thus to approach the recoil limit. The underlying principles of the so-called *Sisyphus cooling* were theoretically modelled in 1989 by Cohen-Tannoudji [31] although experimentally they had already been observed one year earlier by Lett et al. [80]; for a detailed description see [27, 86].

Applying sub-Doppler theory<sup>2</sup> yields expressions for the capture velocity, temperature,

<sup>2</sup>A. Hemmerich, private communication

and mean velocity:

$$\begin{aligned}
 v_c &= \frac{2}{9} \cdot \frac{\Gamma}{k} \left( \frac{\Omega}{\tilde{\Gamma}} \right)^2 \frac{1}{\tilde{\delta}^2 + 1} \\
 k_B T &= \frac{\hbar \Gamma}{8} \left[ \left( \frac{\tilde{\delta} \tilde{\Gamma}}{2\Gamma} \right) + \left( \frac{\tilde{\delta} \tilde{\Gamma}}{2\Gamma} \right)^{-1} \right] \left( \frac{\Omega}{\tilde{\Gamma}} \right)^2 \frac{1}{\tilde{\delta}^2 + 1} \\
 \bar{v} &= \frac{2}{k} \sqrt{\omega_{\text{rec}} k_B T / \hbar}
 \end{aligned}$$

### 6.3.2 The atomic beam and gravitation

The precooled atoms from the Zeeman slower necessarily travel some distance until they reach the trap. During this passage gravitation accelerates the atoms perpendicularly to their propagation, and thus the atoms are dispersed vertically since the atomic beam is oriented parallel to the table surface. After travelling a distance  $s$  the atoms are distributed vertically depending on their initial horizontal velocities  $v$ . Assuming ballistic propagation (without cooling or collisions) and zero initial vertical velocity, their downward excursion is

$$h = \frac{1}{2} g \left( \frac{s}{v} \right)^2 \quad (6.21)$$

The fastest atoms in the beam that can possibly be captured in the MOT have to satisfy  $v < v_c$  where  $v_c = 14.5$  m/s is the capture velocity of the GS-trap. Before they reach the trap, these atoms fall  $h_c \approx 1$  mm during  $s = 20$  cm of free flight<sup>3</sup>. The slowest atoms that can be trapped must exceed  $v_{\text{long}} = 5$  m/s since slower atoms do not enter the interaction region with the trap lasers.

Where do we find *most* of the atoms after the free flight of  $s = 20$  cm? The velocity distribution in the atomic beam [102] is

$$\Gamma(v) dv = \Gamma_0 \cdot \frac{2}{c} \left( \frac{v}{v_0} \right)^3 e^{-\left(\frac{v}{v_0}\right)^2} dv = \Gamma_0 \cdot \frac{1}{h_0} \left( \frac{h_0}{h} \right)^3 e^{-\left(\frac{h_0}{h}\right)^2} dh \quad (6.22)$$

with  $h_0 = \frac{1}{2} g (s/v_0)^2$ , where  $v_0$  is the most probable velocity. We can find the maximum of the distribution and therefore the vertical position where the maximum number of atoms is found at  $h = h_0/3$ . For  $v_0 > 10$  m/s this leads to a negligible vertical displacement of less than 1 mm, but already for  $v_0 = 2$  m/s we are left with a significant  $h \approx 17$  mm!

## 6.4 MOT description

In the steady-state any atomic trap can be sufficiently characterized by the following quantities: number  $N$  of trapped particles, particle density  $n$  or trap volume  $V$ , and temperature  $T$  of the atomic cloud. Density and temperature can be combined in the phase space density  $\rho$ . Various factors influence these quantities in a MOT, most prominently the Rabi

---

<sup>3</sup>This is approx. the distance between the trap and the point where the Zeeman slowing process ends.

frequency and the detuning of the laser, but also the magnetic field gradient and the laser beam diameter. The background vacuum pressure limits the trap lifetime as well as more subtle trap loss mechanisms like heating by inelastic collisions or transitions into untrapped energy levels.

### 6.4.1 Calibration of the trapped particle number detection

The number of trapped atoms in a MOT is usually determined by the fluorescence on the cooling cycle transition. This is possible for the ground-state (GS) trap at 423 nm but no longer true for the metastable trap as we will see later. The 423 nm fluorescence is detected by an amplified photodiode which presents a voltage that has to be related to the number of trapped atoms. The voltage response<sup>4</sup> of the diode is calibrated by a known light intensity<sup>5</sup>.

Not all the fluorescence light from the trap — which radiates into  $4\pi$  solid angle — enters the photo diode: the open solid angle at the observation port is  $\Omega_F = 0.0381$  with  $\varnothing = 13$  mm usable window diameter and a distance of 59 mm between trap center and window. Another restriction is the lens mount diameter of 23 mm at 77 mm from the trap resulting in  $\Omega_F = 0.0381$ , but  $\Omega_F < \Omega_L$ , so the relative light intensity through the lens aperture is  $I/I_0 = \Omega_F/4\pi = 3.034 \cdot 10^{-3}$ , where  $I_0$  is the total fluorescence intensity radiated from the trap. Additional losses are introduced by the window ( $10 \pm 1\%$ ) and the collection lenses ( $14.5 \pm 1\%$ ), thus the light intensity at the photodiode is  $I_{PD} = I_0 \cdot 2.335 \cdot 10^{-3}$ . Using the diode voltage response we find that 1 Volt corresponds to 1.47 mW of trap fluorescence<sup>6</sup> into  $4\pi$ .

The trap fluorescence light power  $P$  can be related to the number  $N(^1P_1)$  of excited trapped atoms by an equation for the rate of fluorescence events:

$$\frac{P}{\hbar\omega} = N(^1P_1) \Gamma. \quad (6.23)$$

The number of trapped atoms in the ground state  $^1S_0$  is greater by the excitation probability as explained in (5.1):

$$\frac{P}{\hbar\omega} = N(^1S_0) \frac{1}{2} \frac{S}{1+S} \Gamma. \quad (6.24)$$

A typical experimental result is a PD signal of 1.5 Volt at an oven temperature of 700°C applying  $U = 29.2$  VAC to the heater wire. This result was obtained at a laser power of 90 mW into the three MOT beams and 50 mW into the slower and molasses beams. The total intensity is twice as high since the MOT is established by retroreflecting the three initial beams. The saturation parameter  $S$  as defined in (5.2) at the trap detuning is  $S(\delta = -\Gamma/2) = \frac{1}{2} (I/I_S)$ . With laser beam diameters of 10 mm and (5.4) the saturation

---

<sup>4</sup>12 Volt per  $0.85 \mu\text{W}$  for diode version 08/1999;  $5.5 \mu\text{W/V}$  (at  $R=1 \text{ M}\Omega$ ) and  $55 \mu\text{W/V}$  (at  $R=100 \text{ k}\Omega$ ) for diode version 11/1999

<sup>5</sup>calibrated reference: powermeter Laser Mate Q (Coherent)

<sup>6</sup> $3.034 \cdot 10^{-5} \text{ W}$  with diode version 08/1999

parameter is  $S \approx 1/2$ . The number of trapped atoms is then

$$\begin{aligned} N(^1S_0) &= \frac{1+S}{S} \cdot \frac{P \lambda}{\pi c \hbar \Gamma} \\ &= 3 \cdot (1.5 \text{ V}) \frac{1.47 \cdot 10^{-3} \text{ W}}{\text{V}} \cdot \frac{423 \text{ nm}}{\pi c \hbar} \cdot (2\pi \cdot 34 \text{ MHz})^{-1} = 1.3 \cdot 10^8. \end{aligned} \quad (6.25)$$

To conclude, typical populations of the ground and excited state of the ground-state trap are

$N(^1P_1)$	$=$	$2.2 \cdot 10^7$
$N(^1S_0)$	$=$	$1.3 \cdot 10^8$

## 6.4.2 Trap loss models and rate equations in equilibrium

### Linear trap loss model

In a simple linear loss model for the trap population we find at equilibrium  $\dot{N} = R - N/\tau = 0$  and therefore simply  $N = R\tau$  where  $R$  is the constant trap loading rate due to the Zeeman slower and  $\tau$  is the experimentally accessible lifetime of the trap. In a vapor loaded MOT  $\tau$  only depends on the background density and temperature via

$$\tau = \frac{1}{n \bar{v} \sigma} \quad (6.26)$$

where  $\bar{v} = 2v_p/\sqrt{\pi}$ ,  $v_p = \sqrt{2k_b T/m}$  is the most probable velocity of the Maxwell-Boltzmann distribution, and

$$n(v) = \frac{4n_0}{\sqrt{\pi}v_p^3} v^2 \exp(-v^2/v_p^2). \quad (6.27)$$

The loading rate is

$$R = \frac{S}{4} \int_0^{v_c} n(v) v dv \quad (6.28)$$

where  $S$  is the trap surface. For  $v_c \ll v_p$  one finds

$$R \approx \frac{S n_0}{\sqrt{\pi}} \frac{v_c^4}{4 v_p^3} \quad \text{and} \quad N = \frac{1}{8} \left( \frac{v_c}{v_p} \right)^4 \frac{S}{\sigma}. \quad (6.29)$$

### Rate equations

The situation is more complicated in our experiment for several reasons: the trap is loaded by a Zeeman slower which already supplies a precooled atomic beam in contrast to the classical thermal velocity distribution in a vapor trap. The transition of excited  $^1P_1$  atoms into the triplet states presents an additional trap loss rate, and one can suspect that a high density in the trap leads to inelastic collisions and thus to increased losses.

Figure 6.2 illustrates the energy levels and transitions discussed in the following rate model.  $R$  is the loading rate into the GS-trap,  $\Gamma_{ij}$  are the transition rates from level  $i \rightarrow j$ , and  $N_k$  are the level populations.



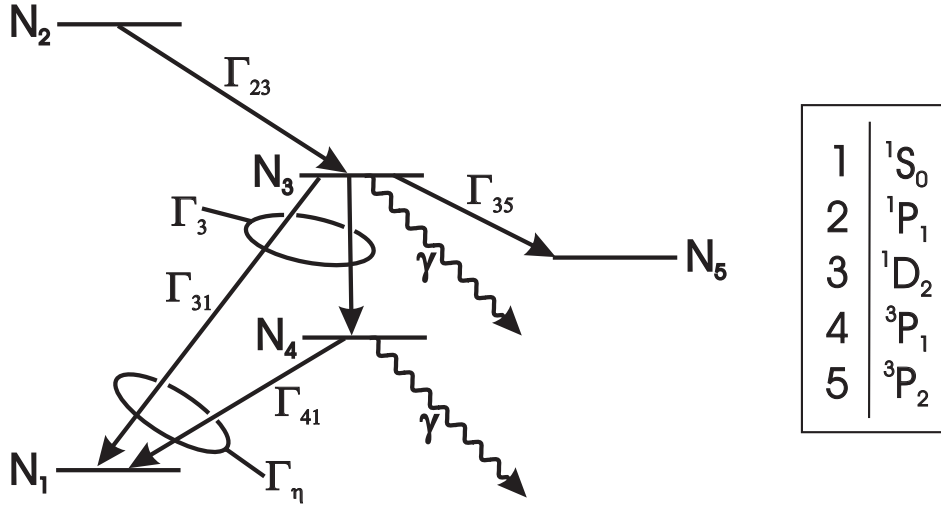


**Figure 6.2:** Energy level diagram with populations and transitions used in rate equations; energies not drawn to scale

k	1	2	3	4	5
assoc. level	$^1S_0$	$^1P_1$	$^1D_2$	$^3P_1$	$^3P_2$

i	2	3	4	2	3	3
j	1	1	1	3	4	5
$\Gamma_{ij}/s^{-1}$	$2.18 \cdot 10^8$	40	2100	2180	300	96

It is assumed that the strong trap laser radiation at 423 nm constantly excites atoms from the GS into  $^1P_1$ , and therefore  $N_2 = \varepsilon N_1$ . The coupled differential equations for the populations are

$$\begin{aligned}
 \dot{N}_1 + \dot{N}_2 &= R - (N_1 + N_2)\gamma + \Gamma_\eta N_3 - \Gamma_{23} N_2 \\
 \dot{N}_3 &= \Gamma_{23} N_2 - (\Gamma_3 + \Gamma_{35} + \gamma) N_3 \\
 \dot{N}_4 &= \Gamma_{34} N_3 - (\Gamma_{41} + \gamma + W) N_4 + W N_1
 \end{aligned}$$

Elimination of  $N_2$  leads to

$$\begin{aligned}
 \dot{N}_1 &= \frac{1}{\varepsilon + 1} (R + \Gamma_\eta N_3) - \left( \gamma + \Gamma_{23} \frac{\varepsilon}{\varepsilon + 1} \right) N_1 \\
 \dot{N}_3 &= \varepsilon \Gamma_{23} N_1 - (\Gamma_{35} + \Gamma_3 + \gamma) N_3
 \end{aligned}$$

For brevity we use the substitution  $\Gamma_3 = \Gamma_{31} + \Gamma_{34}$ .  $\Gamma_\eta$  is the  $^1S_0$ -population change due to transitions from  $^1D_2$  and  $^3P_1$ . Atoms are not trapped while they are in  $^1D_2$  or  $^3P_1$ . During that time they might leave the trap laser beam region. Therefore, not all atoms decaying from these levels contribute to the trap population, and in general we have to allow  $\Gamma_3 \neq \Gamma_\eta$ .

$\gamma$  is the loss rate due to collisions or transitions into other levels than under investigation.  $W$  is the excitation rate due to the 657 nm laser. Terms including  $W$  are only relevant

when that laser is applied and shall be neglected for the moment. The rate equations can be summarized in

$$\frac{d}{dt} \begin{pmatrix} N_1 \\ N_3 \end{pmatrix} = \begin{pmatrix} -(\gamma + \Gamma_{23} \frac{\varepsilon}{\varepsilon+1}) & \frac{\Gamma_\eta}{\varepsilon+1} \\ \varepsilon \Gamma_{23} & -(\Gamma_{35} + \Gamma_3 + \gamma) \end{pmatrix} \begin{pmatrix} N_1 \\ N_3 \end{pmatrix} + \begin{pmatrix} R \\ 0 \end{pmatrix}. \quad (6.30)$$

The characteristic decay rates of the trap population are the matrix' eigenvalues

$$\lambda_{\pm} = -\frac{1}{2} (p \Gamma_{23} + 2\gamma + \Gamma_3 + \Gamma_{35}) \pm \frac{1}{2} \{ [(p \Gamma_{23}) - (\Gamma_3 + \Gamma_{35})]^2 + 4p \Gamma_{23} \Gamma_\eta \}^{1/2} \quad (6.31)$$

where we used the excitation probability

$$p = \frac{\varepsilon}{\varepsilon + 1} = \frac{N_2}{N_1 + N_2}. \quad (6.32)$$

In the steady state  $\dot{N}_1 = \dot{N}_2 = \dot{N}_3 = 0$ , and thus

$$N_3 = \frac{p \Gamma_{23} \cdot R}{p \Gamma_{23} (\Gamma_{35} + \Gamma_3 - \Gamma_\eta) + \gamma (\Gamma_{35} + \Gamma_3)} \quad (6.33)$$

$$N_1 + N_2 = \frac{(\Gamma_{35} + \Gamma_3) R}{p \Gamma_{23} (\Gamma_{35} + \Gamma_3 - \Gamma_\eta) + \gamma (\Gamma_{35} + \Gamma_3)}. \quad (6.34)$$

The trap loading is terminated by switching off the slowing laser. This results in  $R = 0$ , and neglecting  $\gamma$  we can analyze two special cases:

- $\Gamma_\eta = 0$  :  $\lambda_{\pm} = - \begin{cases} p \Gamma_{23} + \gamma \\ \Gamma_{35} + \Gamma_3 + \gamma \end{cases} = \begin{cases} 363 \text{ s}^{-1} \\ 436 \text{ s}^{-1} \end{cases} \hat{=} \begin{cases} 2.8 \text{ ms} \\ 2.3 \text{ ms} \end{cases}$
- $\Gamma_\eta = \Gamma_{35} + \Gamma_3, p = 1/6$  :  $\lambda_{\pm} = \begin{cases} 753 \text{ s}^{-1} \\ 47 \text{ s}^{-1} \end{cases} \hat{=} \begin{cases} 1.3 \text{ ms} \\ 21.3 \text{ ms} \end{cases}$

The decay of  $N_1$  occurs at both respective time constants (+ and - solution). Metastable  $^3\text{P}_2$  atoms are produced at a rate

$$\tilde{R} = N_3 \cdot \Gamma_{35} = N_2 \frac{\Gamma_{23} \Gamma_{35}}{\Gamma_3 + \Gamma_{35}} = N_2 \cdot 480 \text{ s}^{-1}. \quad (6.35)$$

In the limit of small collisional losses  $\gamma \ll 1$  we can write

$$N_2 \doteq \frac{R}{\Gamma_{23}} \cdot \frac{\Gamma_3 + \Gamma_{35}}{\Gamma_3 + \Gamma_{35} - \Gamma_\eta} \quad (6.36)$$

$$\text{and } \tilde{R} = R \frac{\Gamma_{35}}{\Gamma_3 + \Gamma_{35} - \Gamma_\eta} = \begin{cases} 0.22 R & : \Gamma_\eta = 0 \\ R & : \Gamma_\eta = \Gamma_3 \equiv \Gamma_{\eta, \max} \end{cases} \quad (6.37)$$

The decay constants in preliminary experiments were about a factor of two smaller than  $\lambda_{\pm}^{-1}(\Gamma_{\eta, \max}) = 21.3 \text{ ms}$  and thus showed that some atoms were lost because they left the trapping beams before they decayed back to the GS. To optimize this recycling of atoms we increased the laser beam diameter  $D$  until full recycling was achieved at  $D \approx 13 \text{ mm}$ , and the decay time reached  $\tau = 21 \text{ ms}$ . Under these conditions **the steady-state loading rate**

**of the metastable level is equal to the GS-trap loading rate from the Zeeman slower.** 22% of the atoms that fall from  $^1P_1$  into  $^1D_2$  will proceed to the metastable state, and the remaining 78% return via  $^3P_1$  to the ground state [47].

It is of highest importance to the implementation of the MAO scheme to supply a high flux of precooled atoms into the metastable state. So how can we find the achieved loading rate into the metastable state? It can be deduced by recalling (6.35): the population  $N_2$  of the excited state  $^1P_1$  can be measured by observing the power  $P$  of fluorescence radiated by the trap:

$$N_2 = \frac{P}{\hbar\omega\Gamma} = 4 \cdot 10^7 \quad (6.38)$$

The resulting measured **loading rate of the metastable state** is then

$$\boxed{\tilde{R} = 2 \cdot 10^{10} \text{ s}^{-1}} \quad (6.39)$$

This is not necessarily the loading rate of the metastable trap as we shall see on page 108. Another value that can be calculated from the fluorescence measurement is the number of trapped atoms in the ground state. With a saturation parameter of  $S = 1/2$  we find a ground state population of

$$N(^1S_0) = 2 \cdot 10^8 \text{ atoms.} \quad (6.40)$$

### Nonlinear trap losses

At high trap densities nonlinear losses get important in the analysis of the trap population dynamics. The linear loss model has to be extended to include a term proportional to the square of the density to study losses due to collisions among trapped particles:

$$\dot{N}(t) = R - \Gamma N(t) - \beta \int n^2(r) d^3r. \quad (6.41)$$

The ansatz for the solution of the differential equation for trap decay ( $R = 0$ ) is

$$N(t) = N_0 e^{-\Gamma t} \Phi(t)$$

since exponential decay is still expected but altered by some unknown function  $\Phi(t)$ . Applying (6.41) yields  $\Phi'(t) = \Phi^2(t) \cdot f(t)$  where  $f(t) = -\beta N_0 e^{-\Gamma t}$ . We define

$$g(t) \equiv \exp \left\{ - \int_{t_0}^t f(s) \Phi(s) ds \right\}$$

which has the property  $g''(t) = \frac{f'(t)}{f(t)} g'(t)$ . With  $f = \alpha_1 e^{-\Gamma t} + \alpha_2$  and  $f' = \alpha_0 e^{-\Gamma t}$  we get

$$\Phi = \frac{1}{\alpha_3 e^{-\Gamma t}} \left( \alpha_4 - \frac{\alpha_0 e^{-\Gamma t}}{\alpha_1 e^{-\Gamma t} + \alpha_2} \right). \quad (6.42)$$

$\alpha_4 = 0$  since  $\Phi$  has to be finite for  $t \rightarrow \infty$  and thus  $\Phi = (A e^{-\Gamma t} + B)^{-1}$  with  $A = \alpha_1 \alpha_3 / \alpha_0 = -\beta N_0 / \Gamma$ . Since  $N(t=0) = N_0$  and therefore  $\Phi(0) = 1$ , we find  $B = 1 + \beta N_0 / \Gamma$  and finally

$$N(t) = N_0 \frac{e^{-\Gamma t}}{1 + \frac{\beta N_0}{\Gamma} - \frac{\beta N_0}{\Gamma} e^{-\Gamma t}} \quad (6.43)$$

where  $N_0 = n_0 (\sqrt{\pi}a)^3$  denotes the steady state population and

$$n_0 = \sqrt{\frac{2\Gamma^2}{\beta^2} + \frac{8R}{\beta} (\sqrt{2\pi}a)^3} - \frac{\sqrt{8}\Gamma}{2\beta} \quad (6.44)$$

is the corresponding steady state peak density in the trap. We introduce the ratio of the quadratic losses to the total losses

$$\xi = \frac{\beta n_0}{\beta n_0 + \sqrt{8}\Gamma} = \frac{\gamma - \Gamma}{\gamma + \Gamma} \quad \xi \in [0, 1] \quad (6.45)$$

where  $\gamma = \Gamma + 2\beta N_0 = \sqrt{(\Gamma/2)^2 + R\beta} = \Gamma \frac{1+\xi}{1-\xi}$ . With  $\xi$  we can write (6.43) as

$$\frac{N(t)}{N_0} = \frac{e^{-\Gamma t}}{1 + \frac{\xi}{1-\xi} (1 - e^{-\Gamma t})} \quad (6.46)$$

Inelastic collisions only play a role at large trap densities but never at the beginning of the trap loading, and thus  $\dot{N}(0) = R$ . As long as the density is still low the loading solution is simply  $N(t) = N_0(1 - e^{-\Gamma t})$  with  $N_0 = R/\Gamma$ . For all densities the trap loading is described by

$$\frac{N(t)}{N_0} = \frac{1 - e^{-\gamma t}}{1 + \xi e^{-\gamma t}} \quad \text{or} \quad 1 - \frac{N(t)}{N_0} = \frac{e^{-\gamma t}}{\frac{1}{1+\xi} + \frac{\xi}{1+\xi} e^{-\gamma t}} \quad (6.47)$$

An experimental observation of nonlinear trap losses is possible for the GS-MOT by artificially increasing the density in the trap. This can be achieved by quickly repumping  $^1\text{D}_2$  atoms back to the ground state before they can decay to the triplet states thus closing this trap loss channel [92]. A diode laser at 671 nm pumps the atoms on a strong transition from  $^1\text{D}_2$  to  $5^1\text{P}_1$  from where they can decay to the ground state  $^1\text{S}_0$ . The effect on the trap loading and decay times is shown in figure 6.3.

In this case, we observe a more than three-fold increase of the trap decay time to 72 ms and a twofold increased 423 nm fluorescence level. Moreover, the decay acquires a clearly non-exponential character yielding a slight curvature in the logarithmic representation in figure 6.3(a) (unfilled squares). We have also observed the loading process of the  $^1\text{S}_0$  MOT by suddenly turning on the Zeeman slower and recording the 423 nm fluorescence, see figure 6.3(b). It appears that in contrast to the observations regarding the trap decay there is only a very small increase of the loading time constant if we activate the 671 nm repumper. For linear loss the loading and decay should be purely exponential with the same time constant. These observations strongly indicate the presence of an additional density dependent loss channel occurring for the repumped GS-trap for which inelastic two-body collisions between cold  $4^1\text{S}_0$  and  $4^1\text{P}_1$  atoms could be responsible as supported by observations in strontium [120].

Using the above description of nonlinear trap decay we can interpret the experimental data: while the trap decay involves the linear loss rate  $\Gamma$ , loading occurs with an increased rate  $\gamma$ . The reason for this behavior is that the loading is abruptly terminated once the quadratic regime is reached leading to shorter loading times as compared to what is

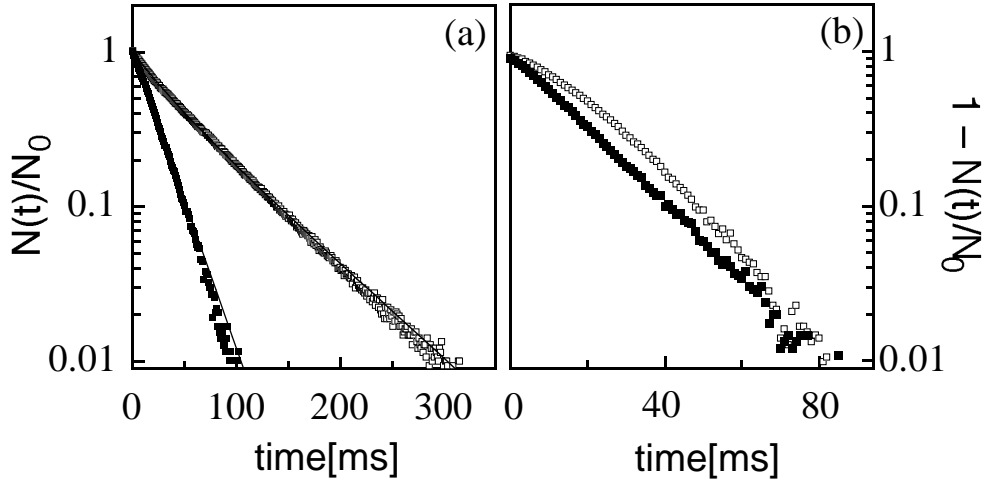


**Figure 6.3:** Trap decay (a) and loading (b) for regular operation (filled squares) and for the case when a repumping laser at 671 nm returns all atoms to the GS-trap, that have fallen into level  $^1D_2$  (open squares).

expected due to linear losses. In contrast to that, the linear loss time constant dominates the trap decay because the initial steady state density is never too far inside the quadratic loss regime, which is clearly observed in our experiments. The above solutions are used to fit the decay and loading data shown in figure 6.3. The parameter  $\xi$  is negligible without repumping ( $\xi < 0.001$ ) but increases to  $\xi = 0.32$  with repumping. Expression (6.45) shows that a diminishment of the linear loss rate  $\Gamma$  by a factor of 3.1 introduced by the 671 nm repumper yields the same increase in  $\xi$  as an enlargement of the capture rate  $R$  by a factor of  $(3.1)^2 \approx 10$ . We can thus conclude that an order of magnitude increase of the capture rate would yield a loss of about 32 % of the atoms due to inelastic collisions rather than a transfer to the desired metastable state. Therefore, only at rates above  $10^{11}$  atoms/s light-assisted two-body collisions can pose a fundamental limitation.

## 6.5 Metastable trap

### 6.5.1 Estimation of the infrared fluorescence

If we assume a trap population of  $N(^1P_1) = 2 \cdot 10^7$  atoms, then from (6.35) the loading rate into the metastable  $^3P_2$  level is  $\tilde{R} \simeq 10^{10} \text{ s}^{-1}$ . Since the Doppler velocity of the transferred atoms is  $v_D = 60 \text{ cm/s}$  we know that the atoms spend about 10 ms in the  $\varnothing=5 \text{ mm}$  infrared beam. If the infrared radiation saturates the trap transition  $^3P_2-^3D_3$  and thus 50% of the atoms are in the excited state, then  $N(^3D_3) = \frac{1}{2} (10 \text{ ms}) \cdot 10^{10} \text{ s}^{-1} = 4 \cdot 10^7$ , and these atoms fluoresce at a rate of  $12 \cdot 10^{12} \text{ photons/s}$  ( $\Gamma = 50 \text{ kHz}$ ). This corresponds to an optical power of  $1.2 \cdot 10^{-6} \text{ W}$  into  $4\pi$ . The detection is limited by the viewport solid angle, so a maximum of 1/300 of the total fluorescence can be collected. The  $2 \times 2 \text{ mm}^2$  lead-sulphide (PbS) photo-electric cell at 80 mm distance to the trap would have to detect the minute power of  $\approx 6 \cdot 10^{-11} \text{ W}$  if no additional collection optics was used.

To test the detector response, a chopped laser beam at 1978 nm is sent on the detector (A) directly and (B) through three 1%-absorbers. The results are (A) 14 Vpp at 26.5 mW and (B) 15 mVpp at 30 nW with good S/N-ratio. Slightly better performance was found for the  $10 \times 10 \text{ mm}^2$  PbS-detector: the lowest detectable intensity with  $S/N \approx 2$  is on the order of 1.5 nW, which is still more than one order of magnitude higher than the estimated fluorescence light at the detector.

In an experiment with the GS-trap we tried to find the atomic resonance at 1978 nm: running the GS-trap we produced metastable atoms and scanned the infrared laser over the expected resonance wavelength, which was adjusted to the wavemeter accuracy. The fluorescence detection sensitivity was increased by chopping the Zeeman slower at 20 Hz and detecting the 1978 nm light phase sensitive with the large PbS-detector and a lock-in amplifier (D). The infrared radiation was sent on two perpendicular axes into the trap, and the fluorescence was detected on the remaining axis perpendicular to the beams. Unfortunately, no evidence for a resonance could be found.

### 6.5.2 Detection of metastable atoms

Since direct detection of the metastable atoms by their fluorescence at 1978 nm seemed to be difficult if not impossible another method had to be found. If the metastable atoms could be transferred to a level decaying at a more convenient wavelength then that fluorescence would provide a measure for the atoms in the metastable state. In fact, the metastable atoms in  $4s4p \ ^3P_2$  can be excited to  $4p4p \ ^3P'_2$  using a strong transition at 430 nm which was already used for cooling by Maxwell's demon [10]. The excited atoms will preferentially decay back to the metastable state, but they will all decay to  $4s4p \ ^3P_1$  after four excitations on average. Since the transition rate is high<sup>7</sup> all atoms will be almost instantly transferred to  $^3P_1$ . From  $^3P_1$  they further decay to the ground state yielding red fluorescence at 657 nm that can be easily detected with a photomultiplier tube.

To check whether the optical pumping laser is on resonance, one needs to monitor the steady-state fluorescence at 657 nm of the ground-state trap. Applying the optical pumping laser at 430 nm increases the red fluorescence by up to 20 % as shown in figure 6.4, where the laser was pulsed at a period of 80 ms by a mechanical shutter.

An absorptive detection of metastable atoms with 430 nm light has failed due to the following reason: the absorption must not change the overall population, therefore optical pumping out of  $^3P_2$  has to be slower than the flight time losses from the cloud. With a production rate of metastables of  $R = 10^{10}$  atoms/sec into a  $\varnothing = 5$  mm cloud where atoms move at  $v \sim 2$  m/s the resulting minimum loss rate from the cloud due to motion is

$$\tau^{-1} = \frac{v}{d} = 200 \text{ s}^{-1}, \quad (6.48)$$

and the above restriction to the optical pumping rate can be written as

$$\tau^{-1} > \frac{1}{2} S \cdot \Gamma \quad (6.49)$$

---

<sup>7</sup>  $\Gamma \approx 2\pi \cdot 20 \text{ MHz}$

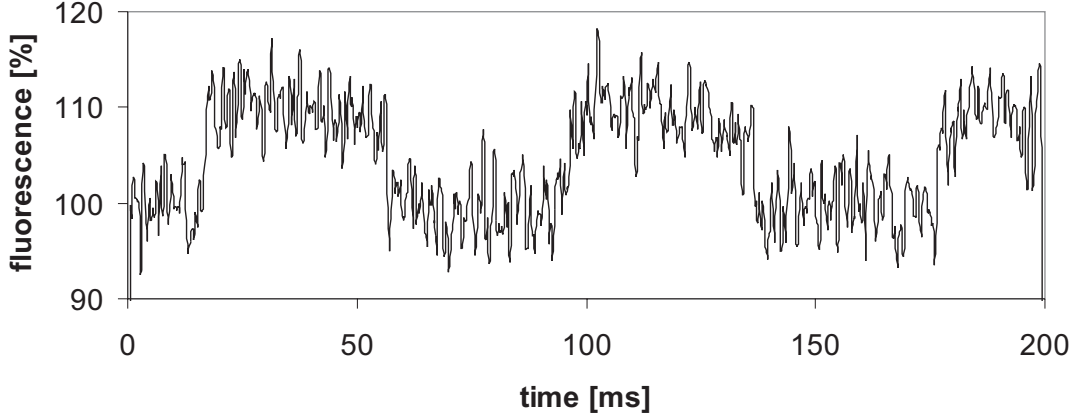


**Figure 6.4:** Applying the 430 nm laser raises the GS-trap steady-state fluorescence at 657 nm, and thus probes the population of the metastable state  $^3P_2$

The 430 nm line has a natural width of  $\Gamma \approx 20$  MHz, and thus only a very small saturation  $S$  is allowed in the absorption experiment which gets increasingly difficult at lower probe intensities. The difference detection of original and absorptively attenuated laser beam did not yield sufficient signal to noise ratio at the required low light levels.

### 6.5.3 Forces acting upon the trapped metastable atoms

In the metastable trap the atoms experience an acceleration due to light forces of

$$a_{\text{max,MOT}} = \frac{\hbar k}{m} \cdot \frac{\Gamma}{2} \cdot \frac{S}{1+S} = 890 \text{ m/s}^2 \quad (6.50)$$

similar to (5.5). Here  $S \gg 1$  and  $\hbar k/m = 4.5$  mm/s.

Contemporaneously the atoms are magnetically captured in the magnetic field of the MOT. The Larmor frequency  $\omega$  changes as

$$\frac{d\omega}{dx} = g \cdot m \cdot \frac{d\omega}{dB} \cdot \frac{dB}{dx} = 80 \text{ MHz/cm} \quad (6.51)$$

since  $\frac{d\omega}{dB} = 1.4$  MHz/G, the magnetic field gradient is 20 G/cm, and  $g = 3/2$  for metastable atoms in the  $^3P_2$  ( $m = 2$ ) state, see A.1. Finally, the acceleration due to the magnetic field gradient is

$$a_{\text{mag}} = \frac{F}{m} = \frac{1}{m} \frac{dE}{dr} = \frac{\hbar}{m} \frac{d\omega}{dx} = 75 \text{ m/s}^2. \quad (6.52)$$

The magnetic potential is weak compared to the Doppler force but cannot be neglected in certain situations as, e.g., described in 7.3.1.

# Chapter 7

## Results

### 7.1 Preparatory measurements

In order to fully operate the intended experiment a number of subsystems have to be separately characterized and optimized, which is described in this section.

#### Infrared laser

The Tm:YAG laser is locked to the atomic resonance at 1978 nm by generating a saturation spectroscopy signal as an error signal for the feedback loop. The absorption signal in

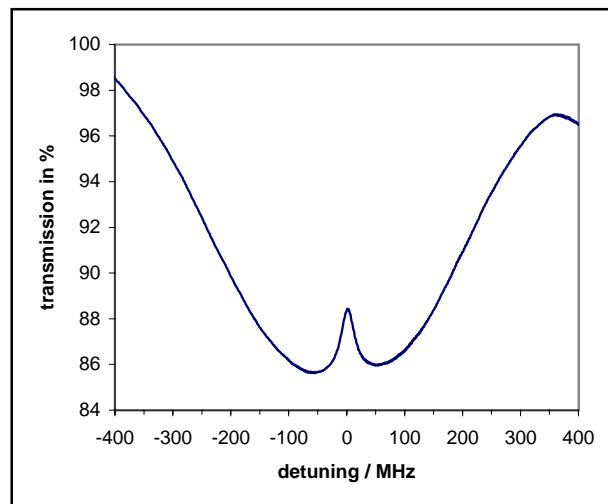


**Figure 7.1:** Saturation spectroscopy signal (100 averages) of the transition  $^3P_2$  to  $^3D_3$  at 1978 nm as recorded by one of the extended-InGaAs diodes. The linear absorption of 14% was found at a reservoir heater power of 70 W (20 V).

figure 7.1 exhibits a broad absorption profile due to the high temperature of the calcium atoms and a much narrower saturation dip in the center with a width of about 35 MHz. This width is due to the varying Stark shift caused by the strong electric field of the



discharge. Splitting the signal beam of the saturation setup into the two orthogonal polarizations with a Wollaston prism, recording the intensity of the two resulting beams with InGaAs photodiodes, and finally subtracting one electronic signal from the other removes the broad Doppler profile. The saturation dips recorded by the two diodes are centered at slightly different frequencies since the pump beam changes by optical pumping the polarization of the atomic cloud and thus the polarization of the medium changes while the probe beam crosses the resonance. The subtraction results in a dispersive signal centered at the transition frequency half way between the two separate saturation dips. This error signal is independent from laser intensity but suffers from polarization changes in the laser output. Therefore it is mandatory to provide a well-defined polarization to the saturation spectroscopy by placing a Glan-Thomson linear polarizer between the laser and the discharge lamp. The frequency scale of the abscissa is calibrated by scanning the laser simultaneously across an etalon with known FSR and fixed length, see figure 4.17. The temporal delay between the resonance peaks corresponds to

$$\Delta\nu = \text{FSR}(\text{Etalon}) - \text{FSR}(\text{Tm:YAG}) = 1.5 \text{ GHz} - 1021 \text{ MHz} \approx 500 \text{ MHz} \quad (7.1)$$

of the frequency scan.

## 7.2 Lifetime of the metastable MOT

The metastable trap operates on a closed cycle transition, atoms excited from  $^3P_2$  to  $^3D_3$  can only decay back to the metastable state. Nevertheless the lifetime of the metastable MOT is limited by several processes: collisions with hot background gas atoms certainly account so far for the most important loss channel since the vacuum at the trap location is only on the order of  $10^{-8}$  mbar when the atomic beam is switched on. But even under perfect vacuum conditions collisions among the trapped atoms themselves pose another limitation. Theoretical investigations into the expected collision cross-sections have just been initiated.

The measurement of the metastable trap lifetime is unfortunately not as straightforward as in the case of the ground-state trap, where it is given by the fluorescence decay time constant after interrupting the loading process by switching off the Zeeman slower beam. The fluorescence at  $2 \mu\text{m}$  cannot be observed directly as described in section 6.5. Instead the alternative route using optical pumping at  $430 \text{ nm}$  has to be chosen again.

The successive experimental steps are as follows: At first both traps are loaded for at least  $200 \text{ ms}$  by applying the Zeeman slower beam and the MOT beams at  $423 \text{ nm}$  and  $1978 \text{ nm}$ . At  $t = 0$  all blue beams are switched off while the  $2 \mu$  beams remain on — all atoms leave the trap region except for the metastable atoms that are trapped in the IR-MOT. After a variable delay time the optical pumping pulse at  $430 \text{ nm}$  is applied for a few ms, which transfers the metastable atoms to  $^3P_1$  from where they decay to the ground state under emission of  $657 \text{ nm}$  photons. Throughout the experiment a PMT monitors the red fluorescence, typical traces are given in figure 7.2.

The steady-state fluorescence is due to excited atoms from the GS-trap that do not return to the ground state directly but via  $^1D_2 - ^3P_1$ . The steady-state level is normalized to one. The height of the peak resulting from the optical pumping pulse corresponds to

the number of trapped metastable atoms. Increasing the delay time between termination of loading and optical pumping decreases the number of trapped atoms and thus the peak height. Mapping out the peak height for different delay times therefore allows to deduce the lifetime of the metastable trap of 260 ms, see figure 7.5(a). This lifetime is mainly limited by the poor vacuum of about  $10^{-8}$  mbar but possibly also by collisions between trapped atoms in the  $^3P_2$  and  $^3D_3$  states. These collisions will be examined in further experiments after loading an additional magneto-optical trap separated from the current main chamber by a differential pumping section.

Before moving on to the calculation of the number of trapped particles it has to be mentioned that great care has to be taken not to accidentally introduce additional trap losses during the time between termination of loading and detection which would shorten the lifetime. A major loss occurs if the optical pumping laser at 430 nm is not completely switched off as we can see by calculating the optical pumping rate  $\tilde{\Gamma}$  from  $^3P_2$  into  $^3P_1$  at two different intensities of 430 nm light. For both situations the available laser power is  $I_0(430 \text{ nm}) = 3 \text{ mW}$ ,  $I_s = 30 \text{ mW/cm}^2$ , beam area  $A = 0.5 \text{ cm}^2$ , and  $\Gamma = 2\pi \cdot 20 \text{ MHz} = 1.3 \cdot 10^8 \text{ Hz}$ .

$$\text{“ON”}: \quad I = I_0 \quad \tilde{\Gamma}_{\text{on}} = \frac{1}{2} \frac{I}{I_s} \Gamma \approx 10^7 \quad \Rightarrow \quad \tau = 100 \text{ ns}$$

$$\text{“OFF”}: \quad I = \frac{1}{5000} I_0 \quad \tilde{\Gamma}_{\text{off}} = \frac{1}{5000} \tilde{\Gamma}_{\text{on}} = 2 \cdot 10^3 \quad \Rightarrow \quad \tau = 500 \mu\text{s}$$

Even in this “OFF”-situation the metastable trap will be depleted within less than 1 ms! To completely switch off the 430 nm light the mechanical shutter was improved, moved as far away from the experiment as possible, and shielded to block stray light reflections into the chamber.

To calculate the absolute number of trapped metastable atoms from the red fluorescence signal we can use the rate equation terminology developed in 6.4.2 and figure 6.2. The steady-state fluorescence at 657 nm of the GS-trap is

$$\gamma_{\text{GS-MOT}}^{\text{red}} = \gamma_{24} = 3/4 \gamma_{12} = 3/4 \cdot N_1 \cdot \Gamma_{12}. \quad (7.2)$$

After loading the IR-MOT, a delay time and optical pumping at 430 nm, the rate of red fluorescence will be  $\gamma^{\text{red}} = N_3 \cdot \Gamma_{40}$  since  $\Gamma_{34} \gg \Gamma_{40}$ . The peak-to-MOT-level ratio is then

$$\rho = \frac{\gamma^{\text{red}}}{\gamma_{\text{GS-MOT}}^{\text{red}}} = \frac{N_3 \Gamma_{40}}{3/4 \cdot N_1 \Gamma_{12}} \simeq \frac{4}{3} \cdot \frac{N_3}{N_1} \quad (7.3)$$

With  $N_1 = 2 \cdot 10^7$  and e.g.  $\rho = 7.7$  we find that the number of trapped metastable atoms is  $N_3 \approx 10^8$ .

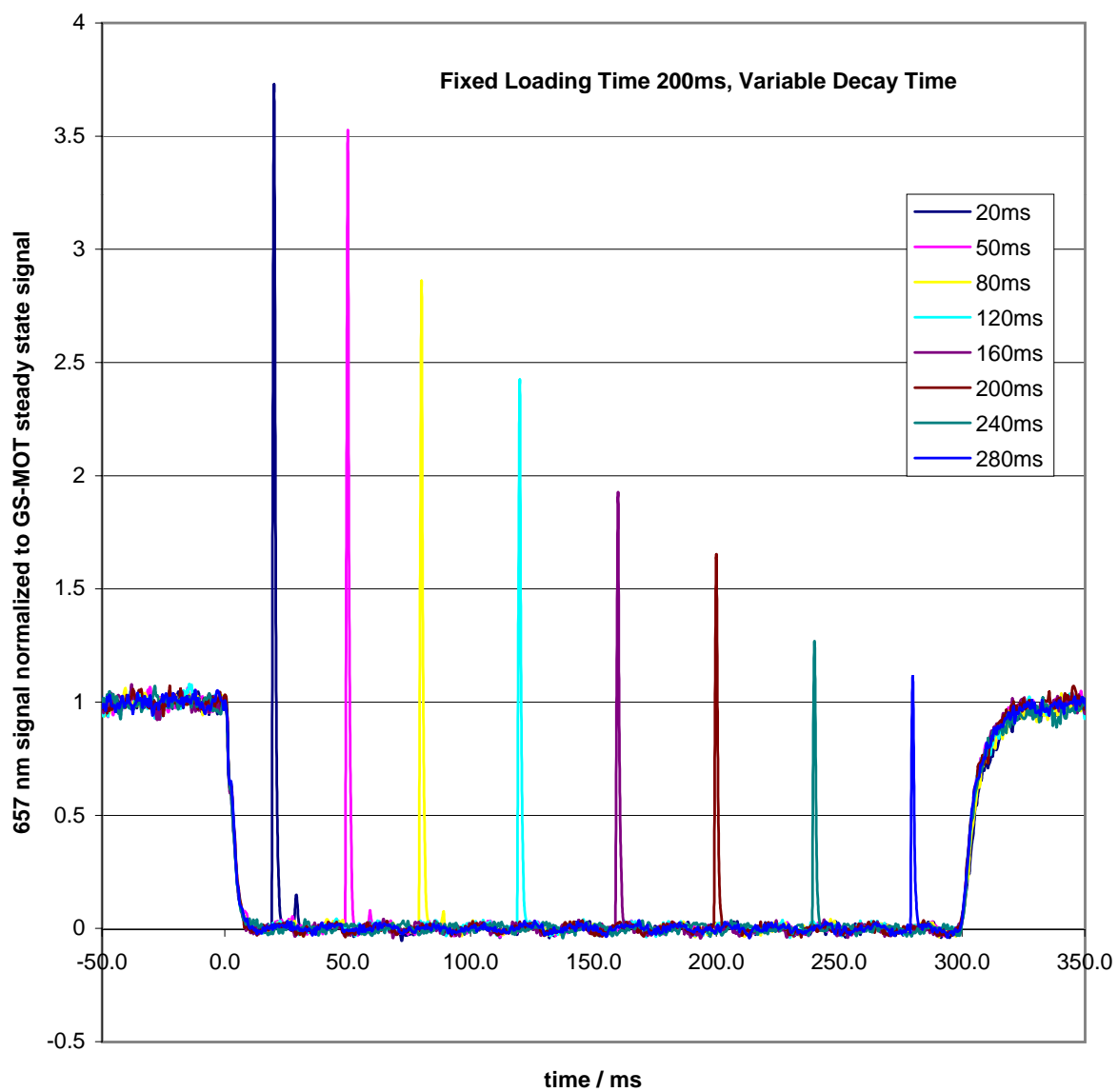


**Figure 7.2:** Longer delay times after the termination of loading lead to loss of trapped metastable atoms, hence the decreasing fluorescence peaks map out the lifetime of the metastable trap

### 7.3 Temperature of the metastable atoms

Temperature is only well defined in thermal equilibrium, where the atomic velocity follows a Maxwell-Boltzmann distribution as given in equation (3.8). To measure this temperature one can use several approaches, more or less falling into one of the following two categories: spectroscopy of the Doppler width of a narrow line or a time-of-flight measurement. In the latter the trapping forces are removed and after a variable duration of free expansion the atomic ensemble is probed for the remaining number of atoms. We performed two different time-of-flight measurements that are described below.

#### 7.3.1 Time-of-flight experiment — recapture method

To remove the trapping forces we could block the MOT-beams but this seems more trivial than it is: even at an attenuation of 200 by a simple mechanical shutter the infrared transition is still saturated ( $S \gg 1$ ) and some atoms still experience trapping forces.

To consider which atoms can be trapped at this lower light intensity we note that the width of the deceleration range due to the Doppler force decreases with light intensity, but only at  $S < 1$  the peak value of the force starts to decrease. Thus the atoms still experience a strong Doppler cooling force but this interaction is confined to a thin shell of width  $\Delta s \propto \tilde{\Gamma}$  at a distance  $s$  from the trap center, as shown in figure 7.3. The magnetic field of the

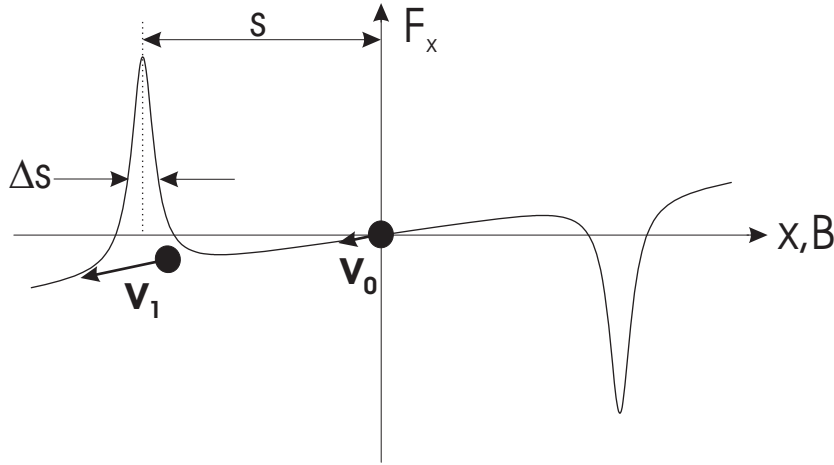


**Figure 7.3:** Resting atoms in the trap center are accelerated due to the magnetic field gradient. If the MOT light at 1978 nm is only attenuated but not switched off completely the atoms will still experience a Doppler force however restricted to a thin region. This explains deviations from the expected free expansion decay.

MOT and gravity accelerate resting atoms in the trap center until they reach the Doppler cooling shell. If they start with  $v_0 \approx 0$  they will accelerate to  $v_1 = \sqrt{2 s a_{\text{mag}}} = 0.5$  m/s using  $s = 2$  mm and equation (6.52). The maximum velocity that can be captured during passage through the Doppler cooling shell is  $v_2 = \sqrt{2 a_{\text{max,MOT}} \Delta s} = 1$  m/s where we used

$$\Delta s = \frac{\tilde{\Gamma}}{d\omega/dx} \approx \frac{5 \text{ MHz}}{80 \text{ MHz/cm}} \approx \frac{1}{2} \text{ mm} \quad (7.4)$$

and equation (6.50). Since the calculated velocities  $v_1$  and  $v_2$  are similar it is likely that even low light intensities will alter the free expansion behavior and thus distort the results.

Instead of blocking the infrared MOT beams we can use a different approach: transferring the atoms into the untrapped ground state effectively removes the trapping potential. After some duration of free expansion and free fall under gravity atoms can be recaptured by applying the blue GS-MOT as long as they are still in the capture volume of this trap. The experiment is similar to the lifetime measurement only that additionally the 423 nm MOT beams have to be turned on at some variable time delay after the optical pumping pulse. The timing of the applied light pulses and the resulting fluorescence at 657 nm is shown in figure 7.4.

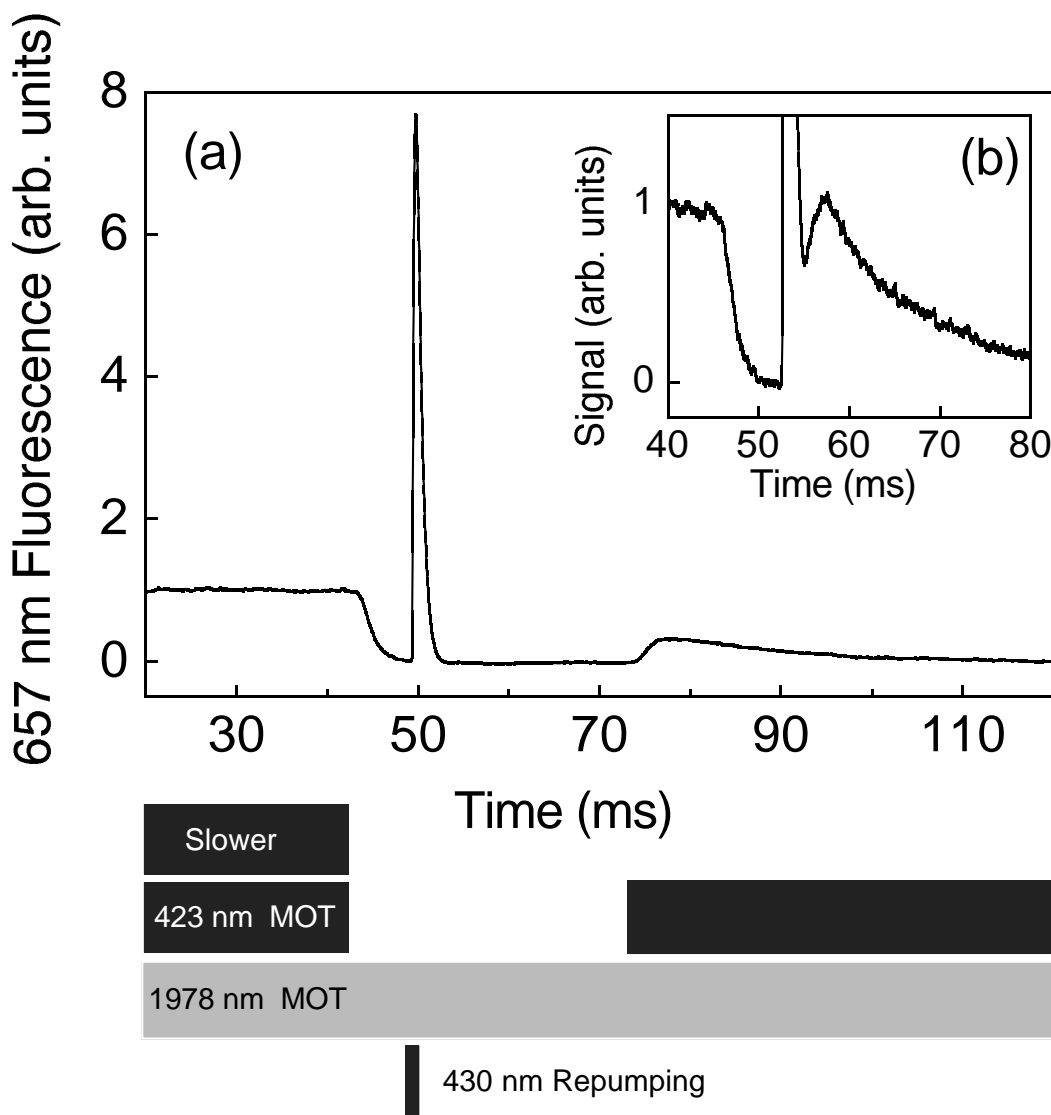


**Figure 7.4:** Pulse sequence and fluorescence signal (a) of the recapture experiment. Insert (b) demonstrates that for short delay times the recaptured population can exceed the steady-state GS-trap population, reflecting the greater number of atoms in the metastable trap.

To gain a theoretical model for the cloud expansion and recapture we describe the temporal evolution of the atomic cloud, see also [104, pp.80]: The spatial location of an atoms varies as  $x(t) = x_0 + vt$ . With a Gaussian velocity distribution  $f(v) = \exp(-mv^2/2kT)$  we find the spatial distribution

$$f(x, t) = e^{-\frac{m}{2kTt^2} (x-x_0)^2} \quad (7.5)$$

The distribution has an initial non-zero radius  $\sigma_0$  and thus

$$f(x, t = 0) = e^{-\left(\frac{x_0}{\sigma_0}\right)^2} \quad (7.6)$$

The number of atoms within a certain volume at a given time  $t$  is

$$F(x, t) = \int dx_0 e^{-\frac{m}{2kTt^2} (x-x_0)^2 - \left(\frac{x_0}{\sigma_0}\right)^2} \quad (7.7)$$

$$= \int dz \sigma_0 e^{-\alpha (x'-z)^2 - z^2} \quad (7.8)$$

$$\approx e^{-\frac{\alpha}{\alpha+1} (x')^2} \left[ \int dz e^{-(\alpha+1) \left(z - \frac{\alpha}{\alpha+1} x'\right)^2} \right] \quad (7.9)$$

$$\approx e^{-\frac{\alpha}{\alpha+1} \frac{1}{\sigma_0^2} x^2} = e^{-\left(\frac{x}{\sigma(t)}\right)^2} \quad (7.10)$$

where the substitutions  $z = x_0/\sigma_0$ ,  $x' = x/\sigma_0$ ,  $\alpha = \frac{m\sigma_0^2}{2kTt^2}$ , and  $\sigma^2(t) = \sigma_0^2 + 2kTt^2/m$  have been used [18].

Finally the number of atoms in the recapture volume is

$$N(t) = \frac{4}{\sigma^3 \sqrt{\pi}} \int_0^R dr r^2 e^{-(r/\sigma)^2} = \frac{4}{\sqrt{\pi}} \int_0^{R/\sigma} dx x^2 e^{-x^2} \quad (7.11)$$

So far we described the evolution of a single cloud. In the experiment however we need to take into account that the atoms in the metastable trap have to be described by two clouds with different temperatures and spatial dimensions.

The GS-trap and the metastable trap are located at the same position and therefore experience the same magnetic field gradient. The optimum field gradient<sup>1</sup> for the GS-MOT is on the order of 60 G/cm, but for the metastable trap it is below 1 G/cm. As a compromise, we use a gradient of 15 G/cm. To increase the capture range of the metastable trap in this steep gradient it is necessary to strongly saturate the cooling transition by a factor of about 7800 as we found experimentally. Only then a sufficient number of atoms can be captured, but unfortunately this also increases the Doppler temperature from 3.1  $\mu$ K to 170  $\mu$ K since the power-broadened linewidth  $\Gamma' = \Gamma \cdot \sqrt{1 + I/I_{\text{sat}}} = 5$  MHz is large compared to the natural linewidth  $\Gamma = 57$  kHz.

We know that sub-Doppler temperatures are to be expected in the metastable trap because of additional polarization gradient cooling, see page 85. Due to the steep gradient this is only true for a central core in the trap (about 2 mm diameter). Therefore we need to assume to find two distinct ensembles in the trap, a small core of sub-Doppler cold atoms

---

<sup>1</sup>to maximize the capture range and still reach a temperature near the Doppler limit

in the  $\mu\text{K}$ -range and a surrounding halo of hot atoms at temperatures of several hundred  $\mu\text{K}$ .

The temperature of the hot atoms will certainly end up close to the Doppler limit, which is here determined by the high laser intensity. But how about the cold atoms — what is the theoretically expected final temperature under the given circumstances of high trap laser power? In the regime of a detuning large compared to the natural linewidth several approximations apply in the analysis of the steady-state temperature [86]. Most of the heating in this situation is due to diffusion of the fluctuating dipole force. For the  $\sigma^+ - \sigma^-$  MOT polarization configuration with  $\delta \approx \Gamma_{\text{sat}}$  the temperature due to polarization gradient cooling is approximately

$$k_B T = \frac{\hbar \Omega^2}{10 |\delta|} = \frac{\hbar \Gamma}{20} \sqrt{\frac{I}{I_S}}. \quad (7.12)$$

For a high saturation of  $10^4$  this gives  $T_{\text{PGC}} = 17 \mu\text{K}$  as an expectation value for the temperature of the cold atomic fraction.

In figure 7.5 the recapture data is shown together with a fitted curve using the model of two clouds of different initial radius and temperature falling under gravity. The fifth fitting parameter is the ratio of the number of hot to cold atoms.

The dashed curves in (b) show that changing the fit temperature of the cold atom fraction by  $\pm 10 \text{ K}$  creates an obvious mismatch with the data thus strengthening the relevance of the fit parameters. The fit temperatures are valid for the atoms in the ground state.

The optical pumping transition at 430 nm connects the  $^3\text{P}_2$  and  $^3\text{P}_1$  states to a higher lying  $^3\text{P}_2$  ( $4p^2$ ) state with a line strengths ratio of 3:1. Thus, in the optical pumping of  $^3\text{P}_2$  atoms into  $^3\text{P}_1$  on average 4 photons are absorbed from the 430 nm laser beam and, together with a 657 nm photon, spontaneously emitted. This leads to a temperature increase of  $3.8 \mu\text{K}$  and a center of mass velocity change of  $9 \text{ cm/s}$ . In a time interval of 20 ms this amounts to a 1.8 mm horizontal displacement of the atomic cloud, together with a vertical displacement of 2 mm due to gravity. These effects have not been taken into account in our model such that our temperature estimations are to be referred to as upper bounds.

The value  $T_c = 22.7 \mu\text{K}$  found for the recaptured ground-state atoms indicates an upper bound of  $19 \mu\text{K}$  for the temperature of the cold fraction in the metastable trap [49].

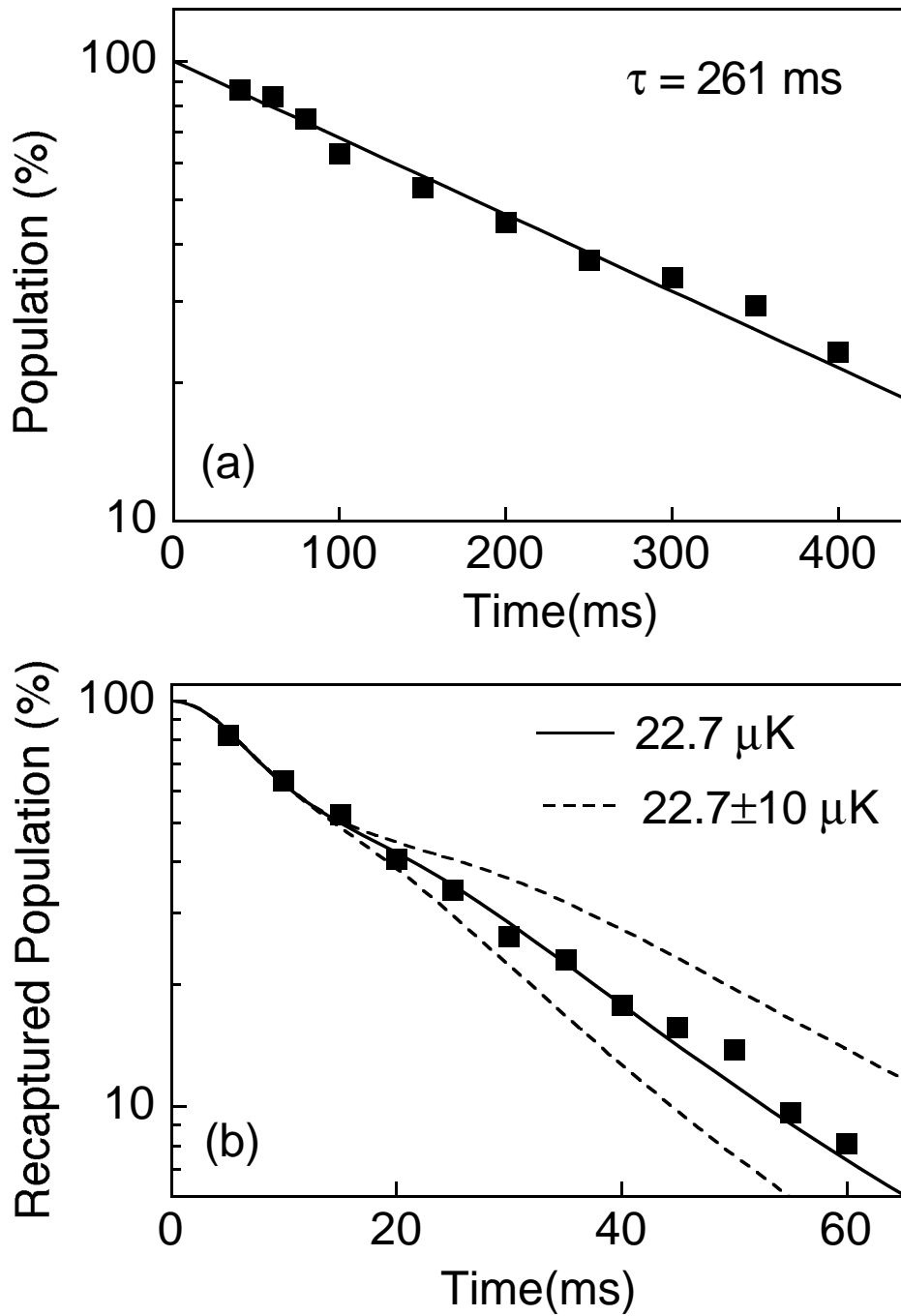


**Figure 7.5:** Experimental results (squares) and fitted curves for (a) the lifetime and (b) the temperature of the metastable atoms in the IR-MOT. Temperature fit parameters: for the cold cloud  $T_c = 22.7 \mu\text{K}$ ,  $\varnothing_c = 2$  mm; for the hot cloud  $T_h = 409 \mu\text{K}$ ,  $\varnothing_h = 6$  mm; hot-to-cold atom number ratio = 2.2



### 7.3.2 Time-of-flight experiment — light carpet method

The first time-of-flight experiment relied on recapturing atoms in the GS-MOT so that the size of the 423 nm MOT beams limits the analyzable free expansion times. To enable the observation of longer flight times we provide an additional probe laser as far below the trap center as geometrically possible<sup>2</sup>. This laser is stretched out horizontally to form a thin sheet of light resonant with the  $^1S_0 - ^1P_1$  transition of atoms at zero transverse velocity.

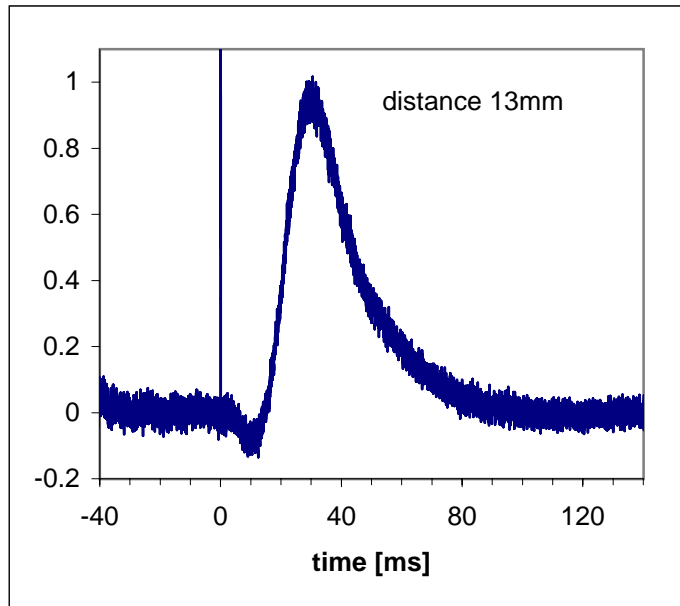


**Figure 7.6:** *Time-of-flight measurement using a sheet of resonant light as a probe beam*

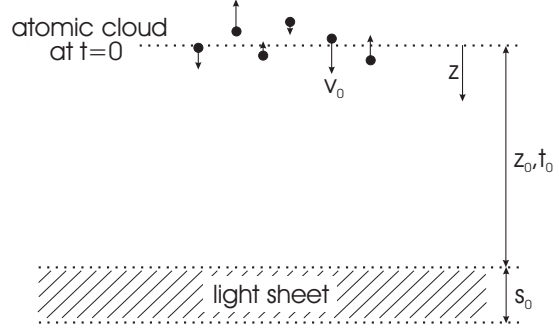
The fluorescence of atoms falling through the light sheet is collected by a PMT through the bottom viewport, the PMT sitting behind a  $2 \mu\text{m}$  mirror. The sensitivity of the PMT has to be gated since the blue fluorescence of the GS-MOT during the loading phase is many orders of magnitude stronger than the weak light from excitations in the light sheet.

Using a light sheet ensures that all atoms from the trap are detected after the free flight: assuming an initial velocity of  $v = 5 \text{ cm/s}$  for the cold atoms we find a maximum downward velocity of  $v_g = g \cdot t$ . Even after falling through 5 cm the transverse excursion of the fastest atoms is limited to 5 mm, easily covered by the light sheet. The time-of-flight signal is shown in figure 7.6.

<sup>2</sup>The size of the horizontal viewport allows for a distance of about 15 mm.

### Interpretation of the experimental results

To understand the time-of-flight signal we need to describe the time dependent probability to excite falling atoms within the volume illuminated by the resonant light sheet. The geometry of the setup is sketched on the right. The problem is reduced to the  $z$ -direction since the light sheet is sufficiently wide to detect all falling atoms.



At what time  $t_0$  does an atoms reach the light sheet? We assume a Gaussian distribution  $P(z_i) = A \exp \left[ - \left( \frac{z_i}{\Delta z/2} \right)^2 \right]$  of the atomic location at  $t = 0$ . The atoms are accelerated by gravity, thus  $v(t) = v_0 + g t$  and  $z_0 - z_i = v_0 t_0 + \frac{1}{2} g t_0^2$ . The time to reach the light sheet is

$$t_0 = -\frac{v_0}{g} \pm \frac{1}{g} \sqrt{v_0^2 + 2 g z_0}. \quad (7.13)$$

The distribution of initial velocities  $v_0$  is also Gaussian, thus

$$P(v_0) = \frac{2}{\Delta v} \sqrt{\frac{\ln 2}{\pi}} \exp \left[ - \left( \frac{v_0}{\Delta v/2} \right)^2 \right] \quad (7.14)$$

where  $v'_0 = 0$  is the center of the distribution.  $P(v)$  is normalized as  $\int_{-\infty}^{\infty} P(v_0) dv_0 = 1$ . According to the equipartition theorem the initial width of the velocity distribution is  $\Delta v_0 = \sqrt{\frac{kT}{m}}$  for a one-dimensional problem. The atomic arrival probability at  $z = z_0$  at time  $t$  is

$$P(z_0, t) = P\left(v_0 = \frac{z_0 - z_i}{t} - \frac{1}{2} g t\right) = \frac{2}{\Delta v_0} \sqrt{\frac{\ln 2}{\pi}} \exp \left[ - \left( \frac{\frac{z_0 - z_i}{t} - \frac{1}{2} g t}{\Delta v_0/2} \right)^2 \right]. \quad (7.15)$$

This probability has a maximum at  $t_{\max} = \sqrt{\frac{2z_0}{g}}$ . Since the fluorescence signal is proportional to the integral over all atoms within the light sheet, e.g. all atoms within  $z_0 \leq z \leq z_0 + s_0$ , we need to calculate

$$P_c(t) = \int_{z_0}^{z_0+s_0} P\left(v_0 = \frac{z_0 - z_i}{t} - \frac{1}{2} g t\right) \cdot P\left(z_i = z - v_0 t - \frac{1}{2} g t^2\right) dz. \quad (7.16)$$

Simulations using this description have shown that the model can reproduce the experimental data. However for the current temperatures above 20  $\mu\text{K}$  the temperature fit is ambiguous due to the large number of required fit parameters. The situation is different for submicrokelvin temperatures, where this model is expected to yield a unique and well-defined fit to the experimental data.

### Symmetrical setup of the light sheet

The light sheet beam is applied symmetrically in two opposite directions by reflecting it back in the same shape with suitable collimation. The necessity for this setup can be seen from the following argument: if atoms fall through a resonant light field which is applied only from one side, then the transverse momentum transfer will quickly accelerate the atoms and shift them out of the observation region and thus the attained level of fluorescence is greatly reduced.

To quantify this effect we estimate the expected rate of fluorescence and compare the situations of single-sided and symmetrical light sheet setup. If a light carpet of 10 mm width and 1 mm height is located 10 mm below the trap and the trapped atomic cloud is approximately spherical then its center of mass acquires a speed of 44 cm/s due to acceleration by gravity until it reaches the light carpet. On average the passage of an atom through the carpet requires 2 ms. If the atoms were not transversely accelerated by photon recoils, then they could scatter the following number of photons during this time:

$$\Gamma' \cdot t_{\text{light}} = \Gamma \Pi_{\uparrow} t_{\text{light}} = \frac{1}{2} \frac{S}{1+S} \Gamma t_{\text{light}} = 1.8 \cdot 10^5. \quad (7.17)$$

Here we assume a laser power of 20 mW and thus  $S = 3$ . In any case, they will fall out of this process on average after  $10^5$  excitations because they branch into the  $^1D_2$  state.

In the single-sided illumination the center of gravity of the atomic cloud is shifted sideways by 5 mm after  $\Gamma \cdot t = [2 \Gamma m (5 \text{ mm}/(\hbar k))]^{1/2} \approx 10^4$  excitations. Only for comparison - if the atoms did not get shifted out of resonance, then the center of mass of the cloud would be shifted sideways by  $\frac{1}{2} \frac{\hbar k}{m} \Gamma t_{\text{light}} = 13.3$  m!

Yet even before any of the above can happen the atoms are Doppler shifted out of resonance: the atomic velocity reaches  $k v = \tilde{\Gamma} \Rightarrow v = 29.6$  m/s after  $v/\Delta v \approx 1250$  excitations, where  $\Delta v$  is the recoil velocity due to a single photon.

A comparison of fluorescence rates<sup>3</sup> for the single-sided ( $F_1$ ) and symmetrical ( $F_2$ ) illumination with  $S_1 = 3$  (see above) and  $S_2 = 2 S_1$  yields a factor of about

$$\frac{F_2}{F_1} = \frac{10^5}{1254} \cdot \frac{S_2}{1+S_2} \cdot \frac{1+S_1}{S_1} = 90 \quad (7.18)$$

improvement if the light sheet is applied symmetrically from both sides to the falling atoms. The fluorescence intensity of about  $h \nu \cdot 10^4/(2 \text{ ms}) = 2.3 \cdot 10^{-12}$  W is then well within the detection efficiency of the PMT, see equation (4.23) on page 72.

---

<sup>3</sup> $F = \Gamma \Pi_{\uparrow} = \frac{\Gamma}{2} \frac{S}{1+S}$

# Chapter 8

## Perspectives

*Since this has been done, what remains  
that could be done and has never been done before?*

Nikolaus von Kues<sup>1</sup>

### 8.1 Near-future improvements

From the gained knowledge through progressing with the experiment several aspects have been identified in which the performance of the experimental setup can be improved to yield a higher flux of ever colder calcium atoms. The higher the flux and the colder the atoms that can be supplied to the metastable state, the closer is an experimental realization of the MAO scheme which is the guiding motivation for the entire project as described in the introductory chapter.

#### Loading rate

As we discussed in detail in section 6.4.2, the loading rate of the ground-state trap can be further increased by at least a factor of ten before nonlinear trap losses due to two-body collisions limit the density in the trap. Higher trap loading rates can be reached by increasing the atomic flux from the oven, the Zeeman slower length and maximum slowable velocity, and the MOT capture range (larger beams and steeper magnetic field gradient).

#### Transfer rate

The theoretical rate of transfer from the GS-trap to the metastable level is  $2 \cdot 10^{10}$  atoms/s for a trapped ground-state population of  $2 \cdot 10^8$  atoms as shown in equations (6.35) and (6.39). However, the experimental result for the transfer rate into the metastable trap is only  $1.2 \cdot 10^9$  atoms/s as one can deduce from the number of trapped metastable atoms in steady-state which was measured being  $2 \cdot 10^8$  atoms. This loading rate corresponds to only 6% of the transfer into the metastable state which shows that atoms are lost during the

---

<sup>1</sup>“de pace fidei” / “Der Friede im Glauben”, Vienna edition, p.715: god asking upon the promise of eternal life

transfer. This happens if atoms spend too much time in the untrapped state  $^1D_2$ . When they finally decay to  $^3P_2$ , they can have moved beyond the spatial range covered by the trap laser beams where they are lost for the experiment.

## Temperature limit

As discussed on page 102 the infrared transition has to be strongly saturated to gain a sufficient capture range which leads to a considerably higher Doppler limit. Due to the high field gradient only some fraction of the atoms in the cloud will reach sub-Doppler temperatures by polarization gradient cooling (PGC).

There are two remedies to this situation: a solution which can be realized quite quickly is to run the experiment in a pulsed mode, switching from optimized loading conditions to trap parameters more suited for lowest temperatures. The second, more extensive possibility would demand for a transfer of the cold metastable atoms from the original trap to a different location. This offers the chance to recapture them in a second metastable trap at an optimized lower field gradient using a smaller laser intensity and detuning which results in a lower Doppler limit. In this trap the condition for polarization gradient cooling could be fulfilled for all atoms, and thus a single fraction of sub-Doppler cold atoms should be obtained. The transfer of cold atoms is a well-established technique [81].

In detail the “quick” solution works as follows: after loading the traps, all but the infrared beams for the metastable trap are blocked. The magnetic field gradient is ramped down, and proportionally the trap laser detuning and intensity are decreased. This lowers the atomic temperature while only few atoms are lost, unlike in evaporative cooling. Finally, the atoms can be extracted from the metastable state, returned to the ground state, and analyzed for their temperature. In this situation the small rest magnetic field could also be switched off quickly enough to allow to determine the temperature not only by the time-of-flight method but also through measurement of the Doppler width of the intercombination line at 657 nm.

The second option would imply a reconstruction of the vacuum system, adding another chamber on top of the existing main chamber. As a top window in the existing chamber already a commercial viewport on a CF16 flange is used in difference to the other ports, where indium seals have been applied. Therefore, changes to the existing system are only necessary if additional features are required, but a new chamber can be attached by simple removal of the top window.

Some requirements for the extension chamber and resulting improvements over the conditions in the main chamber are

- improved vacuum pressure relative to main chamber by differential pumping and additional vacuum pumps in the region of the connection tubing
- improved optical access for various quantum-optical experiments by use of a glass cell
- complete suppression of atomic excitations by blue photons. This might necessitate a curved connection between the chambers to avoid a line-of-sight between the two trap

locations. The atoms would then be sent to the remote trap on a slightly parabolic ballistic trajectory.

Regardless which option is chosen, in both cases temperatures below the unsaturated Doppler limit are to be expected, thus submicrokelvin temperatures should be reached.

## 8.2 Light shift trap

Apart from a high flux of cold atoms into the reservoir state the MAO scheme also demands for a trapping potential for atoms in the ground state. Magnetic traps are ruled out since the ground state of calcium is non-magnetic ( $S = 0, L = 0$ ), but an optical trap can be used. There are different trap geometries of increasing complexity, but all of them employ the basic physical concept of interactions between atoms and light fields that lead to spatially varying potentials or *light shifts*.

### 8.2.1 The physical phenomenon

When an atom is placed into a strong laser field the atomic energy levels experience an a.c. Stark shift which can be well understood in the *dressed atom picture*. The separate description of atomic and electromagnetic field states is combined into a common description by a change of the base vector manifold. In the atomic description the effect can be described by an energy shift due to the light shift potential

$$U(\mathbf{r}) = \frac{1}{2} S(\mathbf{r}) \hbar \delta \quad (8.1)$$

which is valid for low saturation  $S(\mathbf{r}) \ll 1$ . It depends on the laser intensity and on the detuning from the atomic resonance. The saturation can be written as

$$S(\mathbf{r}) = \frac{\Omega_n^2(\mathbf{r})/2}{\delta^2 + \Gamma^2/4} \approx \frac{\Omega_n^2(\mathbf{r})}{2\delta^2} \quad (8.2)$$

where we use an approximation for far off-resonant radiation. For the frequency shift we can then write

$$\Delta = \frac{\Omega_n^2}{4\delta} = \left(\frac{\Omega_n}{\Gamma}\right) \left(\frac{\Gamma}{4\delta}\right) = \frac{1}{2} \frac{I}{I_S} \frac{\Gamma^2}{4\delta} \quad (8.3)$$

which is called the *light shift*. The natural linewidth  $\Gamma$  and the oscillator strength  $O$  of an atomic line depend on the transitions dipole matrix element  $\mu$  like

$$\Gamma \sim \omega^3 |\mu|^2 \quad \text{and} \quad O \sim \omega |\mu|^2. \quad (8.4)$$

The light shift can thus be written in terms of  $\mu$  as

$$\Delta = \xi \frac{I |\mu|^2}{\delta}. \quad (8.5)$$

The dipole matrix elements for calcium transitions can be found in [74] noting that  $\mu^2 = \lambda_f g_f$ . The constant  $\xi$  is then found equating (8.3) and (8.5):

$$\xi = \frac{1}{8} \frac{\Gamma^2}{I_S} \frac{1}{\lambda_0 g_0} = 1.328 \cdot 10^{19} \frac{\text{s}}{\text{kg m}} \quad (8.6)$$

where we used  $\lambda_0 = 422.7918 \text{ nm}$ ,  $\Gamma = 2\pi \cdot 34.63 \text{ MHz}$ ,  $\log(g_0) = 0.243$ , and  $I_S = 60.22 \text{ mW/cm}^2$ . Since the matrix elements of all possible transitions from a level contribute to its light shift, the total light shift is finally given by

$$\Delta(\lambda) = \frac{\Gamma^2}{8} \cdot \frac{I}{I_S} \cdot \sum_i^{\text{all lines}} \frac{g_i}{g_{423\text{nm}}} \frac{1}{2\pi c} \left( \frac{1}{\lambda} - \frac{1}{\lambda_i} \right)^{-1}. \quad (8.7)$$

### 8.2.2 Dipole trap

The realization of a light shift or dipole trap [46, 26] is comparatively simple but usually requires a strong laser. It relies on the effect that a force acts upon the atom in a light field which depends on the real part of the complex atomic polarization [52]. The polarization depends on the electric field and on the polarizability  $\alpha$ , which itself depends on the electric field:

$$\mathbf{P} = \epsilon_0 \alpha(\mathbf{E}) \mathbf{E} \quad (8.8)$$

where the diagonalized complex  $3 \times 3$ -matrix for the polarization contains  $\alpha_{\nu\nu} = \alpha_\nu + i\beta_\nu$ . With the electric field written as

$$\mathbf{E}_\nu(r) = \frac{I_\nu}{\epsilon_0} e^{-i\Psi_\nu} \quad (8.9)$$

we can write the total force on a resting atom as

$$\mathbf{F} = -\frac{1}{2} \sum_{\nu=1}^3 \alpha_\nu \nabla I_\nu + \sum_{\nu=1}^3 \beta_\nu I_\nu \nabla \Psi_\nu. \quad (8.10)$$

The second term is the spontaneous or scattering force which is dissipative and thus can be used for cooling. We already used the spontaneous force in the description of radiation pressure in (5.5) and (6.1). The first term is the dipole force  $F_{\text{dip}}$  which is a conservative force that can be used to trap atoms; for a complete description see [86, p.31ff] and the review paper [113]. The dipole force for the case of a standing wave is given as

$$F_{\text{dip}} = \frac{2\hbar k \delta S \sin 2kz}{1 + 4S \cos^2 kz + (2\delta/\Gamma)^2} \quad (8.11)$$

where  $S$  is the saturation as in 5.2 and  $\delta$  is the detuning. For  $\delta < 0$  the force drives atoms to positions where the intensity has a maximum. Therefore, a trap can be realized with a focused laser beam where the focus exhibits an absolute maximum in intensity which falls off in any direction. Recent experiments have even demonstrated trapping of single atoms in dipole traps [40].

### 8.2.3 Cooling while trapping

Suppose the flux and temperature of cold atoms transferred into the metastable triplet state would be fully optimized and all other parts of the MAO scheme had been installed, but the Bose enhancement would not light up the atom laser as intended. In this situation an additional cooling step would be required to further decrease the temperature of the atomic ensemble in the dipole trap.

The dipole force is a conservative force and as such cannot be used for laser cooling<sup>2</sup>. Thus at first glance a temperature decrease seems to be impossible in a dipole trap. The trapped atoms can nevertheless be subjected to cooling processes.

One adequate cooling method is *resolved sideband cooling*: A laser is tuned near an atomic resonance to drive that transition. The wavelength of the laser is adjusted such that an atom on vibrational level  $\nu_{\text{initial}}$  performs a transition to an excited electronic state but loses one vibrational quantum during the excitation ( $\Delta\nu = -1$ ), see figure 8.1. In the subsequent transition back to the ground electronic state the atom can end up with the same ( $\nu_{\text{final}} = \nu_{\text{initial}}$ ) or a reduced number of vibrational quanta ( $\nu_{\text{final}} = \nu_{\text{initial}} - 1$ ). On average this leads to a temperature decrease as long as rethermalization by collisions is possible.

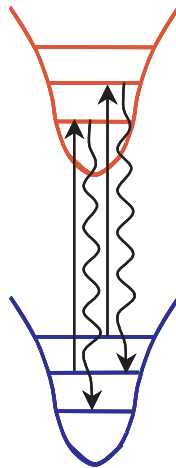


**Figure 8.1:** *Schematic of resolved sideband cooling in a dipole trap*

Several restrictions apply for successful cooling with this method, the two most important being

1. The two electronic levels involved in the cooling process should not experience a different light shift.
2. If the intention is to cool the ensemble into the lowest vibrational state, then the vibrational levels must be resolved. This implies that the laser linewidth should be small compared to the vibrational level spacing.

---

<sup>2</sup>The temperature of an atomic ensemble in a dipole trap can be defined by the population distribution over the various vibrational trap levels.



Actually, if the relative light shift of the two levels gets significantly larger than one linewidth  $\Gamma$ , Doppler cooling will break down, see figure 8.2.

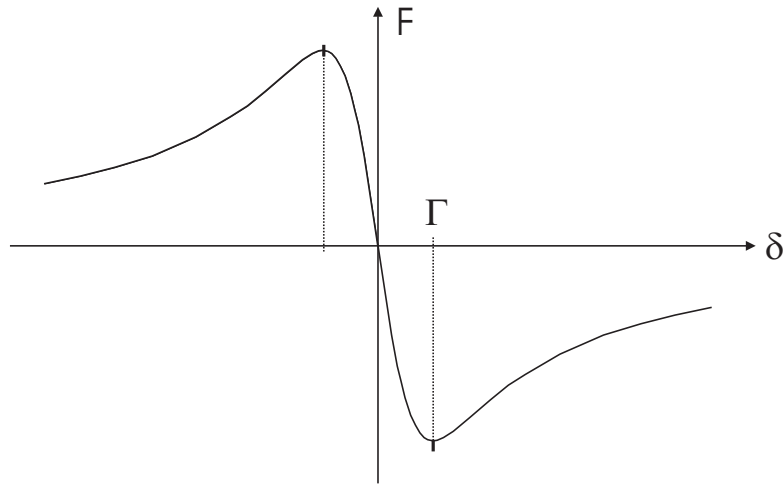


**Figure 8.2:** *Qualitative dependence of the Doppler cooling force on detuning*

In calcium the intercombination line at 657 nm is a suitable transition for resolved side-band cooling of cold trapped ground-state atoms. Using equation (8.7) one can calculate the light shifts of the levels  $^3P_1$  and  $^1S_0$  in a dipole trap at a given intensity and wavelength. Assuming a trap light power of 10 Watt in a beam waist of  $350 \mu\text{m}$  diameter, thus an intensity of  $10^8 \text{ W/m}^2$  we find that the respective light shifts are equal in sign and value for several wavelengths, but one crossing near 1064 nm is of special interest: commercially available Nd:YAG laser systems offer high power at this wavelength at a moderate price.

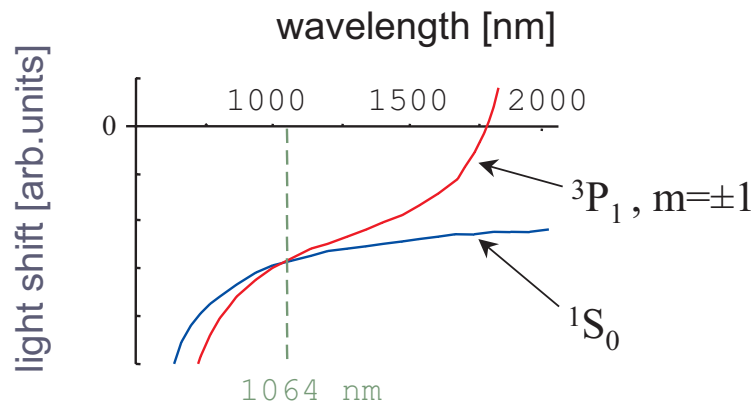


**Figure 8.3:** *Light shift of the levels  $^3P_1$  and  $^1S_0$  for circular polarization*

In summary, it is feasible to trap cold calcium atoms in a dipole trap at 1064 nm and then use resolved side-band cooling to reach even lower temperatures.

# Appendix A

## Calcium data

This chapter will bring together general information on calcium with element-specific data relevant to laser cooling. Calcium was discovered in 1808 by Sir Humphrey Davy / England. A nice overview on calcium is given in [122, p. B-11]:

The name calcium is derived from the Latin word *calx* for lime. (...) Calcium is a metallic element, fifth in abundance in the earth's crust, of which it forms more than 3%. It is an essential constituent of leaves, bones, teeth, and shells. Never found in nature uncombined, it occurs abundantly as *limestone* ( $\text{CaCO}_3$ ), *gypsum* ( $\text{CaSO}_4 \cdot 2\text{H}_2\text{O}$ ), and *fluorite* ( $\text{CaF}_2$ ); *apatite* is the fluorophosphate or chlorophosphate of calcium. The metal has a silvery color, is rather hard, and is prepared by electrolysis of the fused chloride to which calcium fluoride is added to lower the melting point. Chemically it is one of the earth-alkaline elements; it readily forms a white coating of nitride in air, reacts with water, burns with a yellow-red flame, forming largely the nitride. (...) The metal serves as a getter for residual gases in vacuum tubes.

Calcium changes its structure from  $\text{Ca}(\alpha)$  to  $\text{Ca}(\beta)$  at  $T = 673 \text{ K}$  [76]. The phase transition temperatures are given in table A.1 along with other properties of calcium. The nuclide

atomic weight	40.078 u
atomic number	20
melting point	$(839 \pm 2)^\circ\text{C}$
boiling point	$1484^\circ\text{C}$
heat of fusion	8.54 kJ/mol
specific gravity	1.55 g/cm <sup>3</sup> @ 20°C
specific heat	0.63 J/g K
thermal conductivity	2.00 W/cm K
valence	2

**Table A.1:** *Physical and chemical properties of calcium [122]*

<sup>40</sup>Ca has by far the highest natural abundance as shown in table A.2. All isotopes in the

nuclide	<sup>40</sup> Ca	<sup>42</sup> Ca	<sup>43</sup> Ca	<sup>44</sup> Ca	<sup>48</sup> Ca
abundance	96.97 %	0.64 %	0.145 %	2.06 %	0.18 %

**Table A.2:** Natural abundances above 0.1% of stable calcium isotopes [111].

table are bosonic (zero spin) except for <sup>43</sup>Ca (spin 7/2). Table A.3 lists the temperature dependance of the calcium vapor pressure, which needs to be known for the adjustment of the oven temperature and for atomic flux as well as oven lifetime calculations (pages 30 and 32), see equations (3.1) and (3.2) for intermediate temperature values.

<i>T</i> [°C]	406.6	461.5	526.2	603.3	698.3	800	983	1111	1207	1390
<i>p</i> <sub>vap</sub> [torr]	10 <sup>-5</sup>	10 <sup>-4</sup>	10 <sup>-3</sup>	10 <sup>-2</sup>	10 <sup>-1</sup>	1	10	40	100	400

**Table A.3:** Calcium vapor pressure vs. temperature. Data taken from [76, p. 12] for pressures below one torr, from [122, p. D-192] for higher pressures

## A.1 Landé *g*-factors

Knowledge of the Landé *g*-factors [29, p.87] is required to calculate e.g. the Larmor frequency  $\omega_L = g_J \mu_B B / \hbar$  due to the Zeeman effect and other quantities in atomic physics. The atomic magnetic moment is  $\boldsymbol{\mu} = -\mu_B \sum_i (g_l \mathbf{l}_i + g_s \mathbf{s}_i) = \mu_B (g_l \mathbf{L} + g_s \mathbf{S}) = -g_J \mu_B \mathbf{J}$ . The interaction term added to the Hamiltonian by the Zeeman effect due to an external magnetic field is  $H_B = -\boldsymbol{\mu} \cdot \mathbf{B}$ . The resulting energy shift is  $\Delta E = \langle nLSJm_J | H_B | nLSJm_J \rangle = g_J \mu_B m_J B$  where  $g_J$  is defined as

$$\begin{aligned}
 g_J &= g_l \left\{ \frac{J(J+1) + L(L+1) - S(S+1)}{2J(J+1)} \right\} + g_s \left\{ \frac{J(J+1) + S(S+1) - L(L+1)}{2J(J+1)} \right\} \\
 &\simeq \left\{ \frac{3J(J+1) + S(S+1) - L(L+1)}{2J(J+1)} \right\} \quad (\text{A.1})
 \end{aligned}$$

where  $g_l = g_s/2 = 1$  and  $J = L \oplus S$ . Taking into account the nuclear spin  $I$  with  $F = I \oplus J$  one defines

$$g_F = g_J \left\{ \frac{F(F+1) + J(J+1) - I(I+1)}{2F(F+1)} \right\} \quad (\text{A.2})$$

which is here simply  $g_F = g_J$  since  $I = 0$  in the bosonic isotope <sup>40</sup>Ca. For the singlet states in calcium the total spin cancels ( $S = 0$ ) and thus  $g_J = 1$ . The situation is different for the triplet states with  $S = 1$ . Table A.4 lists the *g*-factors for several levels of interest.

	$^1X_y$	$^3P_0$	$^3P_1$	$^3P_2$	$^3D_1$	$^3D_2$	$^3D_3$
		4s4p	4s4p	4s4p	4s3d	4s3d	4s3d
$S$	0	1	1	1	1	1	1
$L$	x	1	1	1	2	2	2
$J$	y	0	1	2	1	2	3
$g_J$	1	-	3/2	3/2	1/2	7/6	4/3

**Table A.4:** Landé  $g$ -factors  $g_J$  for  $^{40}\text{Ca}$  as defined in relation (A.1)

## A.2 Spectroscopic data

ground state	exc. state	$\lambda_{\text{vac}}/\text{nm}$	$\lambda_{\text{air}}/\text{nm}$	linewidth	$\log(g_f)$
$^1S_0$	$^1P_1$	422.7918	422.6728	34.63 MHz	0.243
	$^3P_1$	657.4595	657.2779	419.85 Hz	-4.290
	$^1D_2$	-	-	-	< -10
$^3P_0$	$^3D_1$	1931.4494	1930.9222	34.20 kHz	-1.443
$^3P_1$	$^3D_1$	1951.1064	1950.5739	24.91 kHz	-1.572
	$^3D_2$	1945.8293	1945.2982	45.17 kHz	-1.094
$^3P_2$	4p2 $^3P_2$	428.4216	428.3011	6.91 MHz	-0.224
	$^3D_1$	1992.2632	1991.7195	1037 Hz	-2.758
	$^3D_2$	1986.7614	1986.2192	14.12 kHz	-1.581
	$^3D_3$	1978.2170	1977.6771	57.18 kHz	-0.831
$^3P_1$	4p2 $^3P_2$	430.3738	430.2528	21.60 MHz	0.275
	$^1D_2$	1506.1214	1505.7099	11.38 Hz	-4.915
$^3P_2$	$^1D_2$	1530.5284	1530.1103	2.271 Hz	-5.601
$^1D_2$	$4^1P_1$	5547.3767	5545.8149	19.43 Hz	-3.772
$^1D_2$	$5^1P_1$	671.9536	671.7681	1.924 MHz	-0.610

**Table A.5:**  $^{40}\text{Ca}$  line data taken from [74] including the absorption oscillator strength  $g_f$  (see also [89] for oscillator strength values).

Oscillator strength values for calcium can also be found in [89]. Electric-dipole amplitudes for transitions between low-lying levels are calculated in [97]. The lifetimes of metastable earth-alkaline atoms are calculated in [34]: 38 min for  $\text{Mg}^*$ , 17 min for  $\text{Sr}^*$ , and 118 min for  $\text{Ca}^*$ . A list of spectral lines can be found in [115].

# Appendix B

## Useful numbers, equations and relations

### B.1 Physical constants, conversion factors, and material properties

u	$1.66055 \times 10^{-27}$	kg
	931.48	MeV
h	$6.626176 \times 10^{-34}$	Js
$\hbar$	$1.0546 \times 10^{-34}$	Js
$k_B$	$1.38066 \times 10^{-23}$	J K <sup>-1</sup>
$N_A$	$6.626176 \times 10^{-34}$	Js
e	$1.602192 \times 10^{-19}$	C
G	$6.626176 \times 10^{-34}$	Js
$\varepsilon_0$	$8.8542 \times 10^{-12}$	A s V <sup>-1</sup> m <sup>-1</sup>
$\mu_0 = \frac{1}{\varepsilon_0 c^2}$	$1.2566 \times 10^{-6}$	V s A <sup>-1</sup> m <sup>-1</sup>
$\mu_B = \frac{\hbar e}{2m}$	$9.27 \times 10^{-24}$	J T <sup>-1</sup>

**Table B.1:** *Physical constants*

P / dBm	P / mW	Voltage into 50 $\Omega$ / V
1	1	0.22
3	2	0.32
7	5	0.50
10	10	0.71

**Table B.2:** *Radio frequency power conversion*  $P[\text{dBm}] = 10 \log(P[\text{mW}])$

$\varnothing$ in mm	Cu	Cu/nickel	Cu/manganese
0.711	0.0434	1.23	1.05
1.219	0.0148	0.42	0.355
1.626	0.00831	0.235	0.20
1.000	0.02197	0.622	0.529
1.500	0.00976	0.42	0.355
2.000	0.00549	0.42	0.355

**Table B.3:** Specific resistivities  $\rho$  in  $\Omega/m$  at  $T = 20^\circ C$

Copper	8.9 g/cm <sup>3</sup>
Aluminum	2.7 g/cm <sup>3</sup>
Steel	7.8 g/cm <sup>3</sup>

**Table B.4:** Material densities

high reflector (HR)	max. 5 J/cm <sup>2</sup>
antireflector (AR)	ca. 20 J/cm <sup>2</sup>

**Table B.5:** Destruction threshold of dielectric coatings under 10 ns laser pulses (in-house coatings by Mr. Paeth, BK7 or quartz substrates).

locational accuracy	250 $\mu\text{m}$
runout off straight line	130 $\mu\text{m}$
out of round	130 $\mu\text{m}$
smallest drill size diameter	343 $\mu\text{m}$

**Table B.6:** Limitations in mechanical engineering: drilling holes in stainless steel

## B.2 Mathematical relations

free space propagation	$\begin{bmatrix} 1 & L/n \\ 0 & 1 \end{bmatrix}$
thin lens	$\begin{bmatrix} 1 & 0 \\ -1/f & 1 \end{bmatrix}$
spherical mirror	$\begin{bmatrix} 1 & 0 \\ -2/R & 1 \end{bmatrix}$

**Table B.7:** Ray transformation matrices for selected optical elements [70]

$R/\%$	99	98	97	95	90	80	50
$F$	313	156	103	61	30	14	4
$T_{\min}$	$2.5 \cdot 10^{-5}$	$10^{-4}$	$2.3 \cdot 10^{-4}$	$6.6 \cdot 10^{-4}$	$2.7 \cdot 10^{-3}$	$1.2 \cdot 10^{-2}$	$10^{-1}$

**Table B.8:** Characteristics of a confocal ( $L=R$ ) Fabry-Perot etalon with equal mirrors ( $R_1 = R_2$ ) for different mirror reflectivities: finesse  $F$  and minimum transmission  $T_{\min}$  as defined in (4.14) and (4.15).

The following is a list of frequently used relations from atomic and laser physics:  $S$  is the saturation parameter in general,  $S_0$  is the saturation at zero detuning,  $w_1$  is the Rabi frequency,  $\Pi_{\text{exc}}$  is the excitation probability for a two-level atom in a light field,  $\Gamma'$  is the power-broadened linewidth of the transition,  $\Delta$  is the light shift. Finally  $f_{ik}$ ,  $A_{ik}$ , and  $M_{ik}$  are the oscillator strength, the Einstein coefficient, and the electric dipole matrix element of a transition between two energy levels  $i$  and  $k$ .

$$\begin{aligned}
 \text{saturation parameter } S &= \frac{1}{2} \frac{w_1^2}{\delta^2 + (\Gamma/2)^2} \\
 \text{saturation at } \delta = 0 \quad S_0 &= 2 \left( \frac{w_1}{\Gamma} \right)^2 = \frac{I}{I_S} \\
 \text{excitation probability } \Pi_{\text{exc}} &= \frac{1}{2} \frac{S}{1 + S} \\
 \text{power-broadened linewidth } \Gamma' &= \Pi_{\text{exc}} \Gamma \\
 \text{light shift } \Delta &= \frac{w_1^2}{4\delta} \\
 \text{oscillator strength } f_{ik} &\propto \lambda |M_{ik}|^2 \\
 \text{Einstein coefficient } A_{ik} &\propto \lambda^3 |M_{ik}|^2
 \end{aligned}$$

# Appendix C

## Technical data and procedures

A very helpful guide for the design of the vacuum system and mechanical as well as electrical equipment is [90]. The following encyclopaedia and were used in this thesis: [18] for mathematics, [57] for electronics, [85] for English, and [69, 75] for typesetting.

### C.1 Specifications, physical dimensions, and mechanical drawings

size	small	medium	large
application	compensation	outcoupling	MOT
pieces	2	1	2
turns	88	104	350
free ID/mm	46 (46)	46	130 (130)
OD/mm body	72 (72)	100	190 (164)
OD/mm turns (max)	73 (72)	101	194 (166)
body width /mm			27 (23.5)
width of turns /mm			15 (15)

**Table C.1:** *Dimensions of current (previous) version of all magnetic field coils apart from the Zeeman slower coil. The material of the coil bodies is brass. Short curved copper tubings brazed into the sides connect to the cooling water. Wire thickness  $\varnothing=1.0$  mm.*



eff. crystal length	3.43 mm
Index of refraction	1.803 @ $\lambda = 2\mu$ 1.825 @ $\lambda = 785nm$
Brewster angle	$\phi_b = 60.99^\circ$ $\phi_{b'} = 29.014^\circ$
L1 and L4	60 mm
L2 and L3	10.2 mm
AOI	$13^\circ$

S1	Infrasil flat $\emptyset 12.7 \times 3$ mm, R=98%@1978 nm, AOI=0°; AR < 0,25% @ 1978 nm, AOI=0°
S1a	FS flat $\emptyset 12,7 \times 6,35mm$ , AR <sub>i</sub> 0,25% @ 1978 nm, AOI=0°,uncoated
S2+S3	FS $\emptyset 12.7 \times 6.35$ mm, $r = -20$ mm, HR > 99.9% @ 1978 nm $\oplus$ HT @ 785 nm AOI= 13° AR < 0.25%@ 785 nm AOI= 13°
S4	BK7 $\emptyset 6 \times 2$ mm flat, HR> 99.9% @ 1978 nm,AOI= 0°, AR < 0.25%@ 1978 nm AOI= 0°
See the resonator drawing on page 128 to identify the mirrors S1 through S4.	

		$b/mm$	waist $w_0/\mu m$	focus pos./mm	$\theta/^\circ$
collimated branch	T	128.8	197	0	0.18
	S	116.9	191	0	0.19
before crystal	T	1.8	—	-10.5	—
	S	2.1	—	-11.2	—
behind crystal	T	10,8	58	-1.7	—
	S	3.8	34	-1.7	—
FSR=1023 MHz					

**Table C.2:** *Tm:YAG-laser data: crystal, resonator, mirrors, and beam parameters.*

size	$5 \times 10 \times 40$ mm <sup>3</sup>
application	Pound-Drever-Hall lock of Ti:sapphire and Tm:YAG laser
pieces	2
clear aperture	$4.5 \times 9.5$ mm <sup>2</sup>
crystal axis	z-axis along short side of 5 mm
AR-coating reflectivity	$R < 0.5\%$ per surface
AR-coating peak wavelength	850 nm (Ti:Sa), 1980 nm (Tm:YAG)
AR-coating usability	broadband ( $> \pm 50$ nm from central wavelength)
Parallelism of optical surfaces	$\leq 1$ minute

**Table C.3:** *Specifications of the LiNbO<sub>3</sub> crystal*

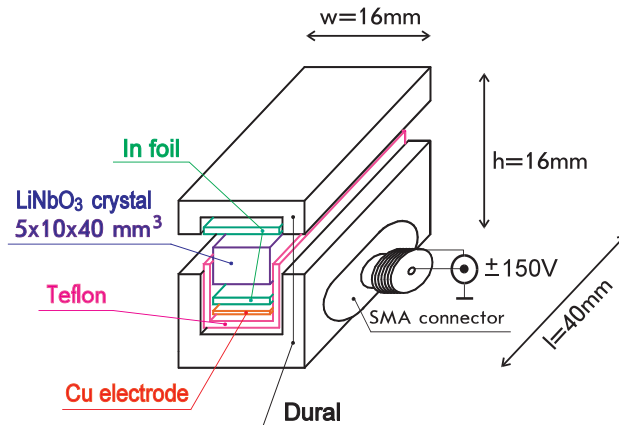


**Figure C.1:** Schematic of the mounted  $\text{LiNbO}_3$  crystal (supplied by Physics Express, Russia)

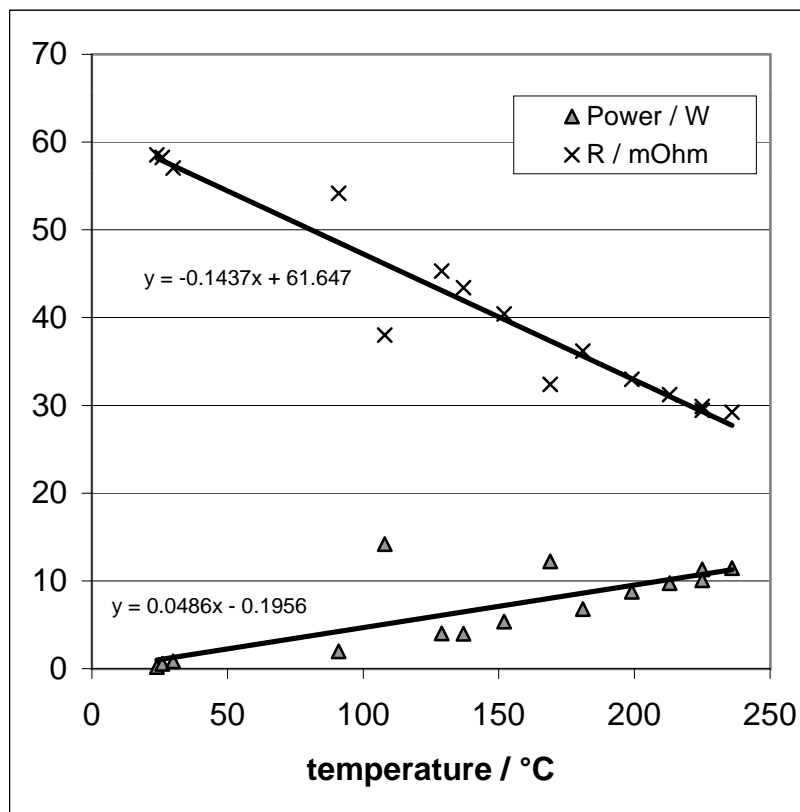


**Figure C.2:** Measurement of the temperature dependent resistance of the tantalum wire heating the reservoir in the prototype calcium discharge lamp. The experiment was performed in air using a high current power supply, see appendix D. Temperature measured with Thermocoax sensor, see footnote on page 29.

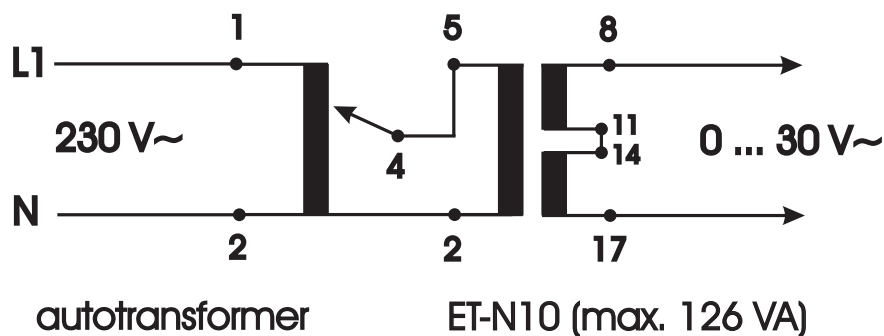


**Figure C.3:** Schematic of power supply for main calcium oven: adding the transformer ET-N10 avoids the risk of accidentally applying 230 V~

	PbSe	PbS	ext. InGaAs	unit
company	CalSensors	CalSensors	Fermionics	
model	BXP	AF-2	FD1000W2.2	
$D^*(\lambda_{pk}, 1000 \text{ Hz}, 1 \text{ Hz})$	typ. $1.8 \cdot 10^{10}$	$1.8 \cdot 10^{10}$	not stated	$\text{cm Hz}^{1/2} \text{ W}^{-1}$
time constant	typ. 2, max. 5		$\approx 35$	$\mu\text{s}$
responsivity	0.03	0.5	1.2	A/W

**Table C.4:** Detectivity  $D^*$ , response time  $\tau$ , and responsivity for FIR-detectors at  $\lambda \approx 2 \mu\text{m}$

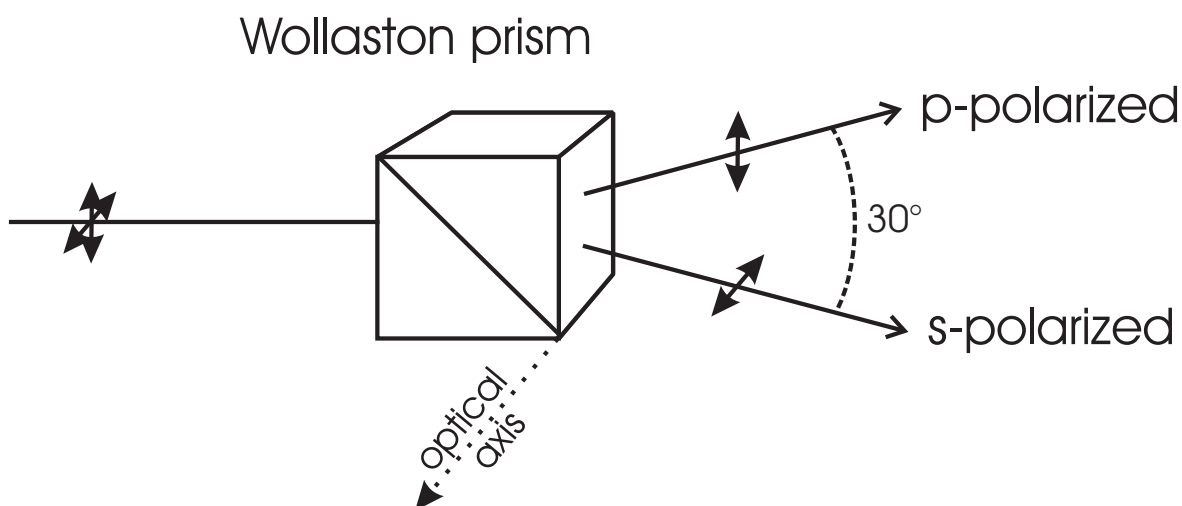


**Figure C.4:** Wollaston prism as used in polarization spectroscopy setup

dimensions	ID 4 mm, OD 6 mm, length 18 mm (original)
max. operating voltage	
in the direction of polarization	1000 V
against the direction of polarization	200 V
axial elongation at $\Delta U = 100 V$	$\Delta x = 8 \mu\text{m}$
radial enlargement at $\Delta U = 1000 V$	$\Delta \varnothing = 2 \mu\text{m}$
axial resonance frequency	80 kHz
radial resonance frequency	75 kHz

**Table C.5:** Specifications of piezoelectric tubes

mirrors	W83 and W84
reflectivities	97.5% at 657 nm ( $0^\circ$ )
substrates	$\varnothing 7.75$ mm, curvature $r = 5$ cm
mirror distance	50 mm

**Table C.6:** Fabry-Perot etalon for analysis of the 657 nm laser

code	wavelength	reflectivity	transmission	application
AR-166	423 nm	1. side $< 0.2\%$ ( $0^\circ$ ) 2. side $0.5\%$ ( $0^\circ$ )		molasses windows
AR-189	420-460 nm	$0.22\%$ (on both sides)	$99.2\%$	slower window

**Table C.7:** Anti-reflection coatings produced at the ILP

code	type	wavelength/nm	number of pieces	dimensions/mm
A-741	HR $45^\circ$ HR $0^\circ$	526 – 591 564 – 670	10	$\varnothing 25.6 \times 6$
A-742	HR $45^\circ$ HR $0^\circ$	478 – 560 507 – 626	5	$\varnothing 25.6 \times 6$
A-746	HR $45^\circ$	844	10	$\varnothing 15 \times 10$
A-604	HR $0^\circ$ HR $45^\circ$ HT $0^\circ$ HT $45^\circ$	640 – 780 600 – 695 404 – 609 390 – 544	short pass filter, also used as mirror in 657 nm PMT setup	$\varnothing 25.6$
A-366	R = 98.5%	650	1	$\varnothing 30$
A-764	R $\cong 8\%$ $0^\circ$ R $< 10\%$ R = 99%	657 570 – 710 1850 – 2050	15	$d = 1$ mm (10 pc.), $d = 5$ mm (2 pc.), $d = 10$ mm (3 pc.)

**Table C.8:** Dielectric coatings produced at the ILP

wavelength	HW	amount	transmission	blocking	blocking range
$422 \pm 1$ nm	11.1 nm	2	$\geq 51\%$	$T \leq 10^{-4}$	x-ray – 1343 nm
$657 \pm 1$ nm	14.6 nm	4	$\geq 72\%$	$T \leq 10^{-4}$	x-ray – 1170 nm
$430_{-0}^{+1.5}$ nm	5 nm	2	$\geq 44\%$	$T \leq 10^{-4}$	x-ray – 1591 nm
			0.1 % @ 422 nm		

**Table C.9:** Dielectric filters (size  $\varnothing 15 \times 7$  mm, by Anders company )

Model	5 Watt	10 Watt
Current Diode 1		25.3 A (1772 h)
Current Diode 2		25.1 A (1775 h)
T(LBO)	151.6°C	150.1°C
T(vanadate)	35.0°C	30.0°C
T(etalon)	75.0°C	61.5°C
T(diode 1)	31.4°C	25.1°C
T(diode 2)	30.1°C	27.0°C
T(base plate)	24.8°C (water 16°C)	

**Table C.10:** Verdi operating parameters

Reading on instrument	192	390	588	785	984
Measured output voltage/V $\pm 0.1$ V	100.0	200.0	300.0	400.0	500.0
Reading on instrument	500	585	634	685	
Measured output voltage/V $\pm 1$ V	516	600	650	700	

**Table C.11:** Calibration data for high voltage supply NSHV-3,5 kV

sheet	30 mW	1.5 mW	1 mW	$< 100 \mu\text{W}$
30–35°C	cont.	1 s <sup>1</sup>	2 s	–
35–36°C	1 s, weak	–	–	–
40–45°C	1 s, weak	1 s, weak	–	–
20–25°C	cont.	cont.	cont.	very diffuse
25–30°C	quick & strong	quick & strong	quick	2–3 s, diffuse
35–40°C	$> 1$ s	$> 1$ s	–	–

**Table C.12:** Response (time and strength) of temperature sensitive sheets to 1978 nm radiation at different power levels

detector	area / mm <sup>2</sup>	resistance	bias	op. voltage
large PbS detector <sup>2</sup>	$10 \times 10$	1.3 M $\Omega$	1 M $\Omega$	630 V
small PbS detector <sup>3</sup>	$2 \times 2$	1.3 M $\Omega$	1 M $\Omega$	100 V

**Table C.13:** Detector operating parameters

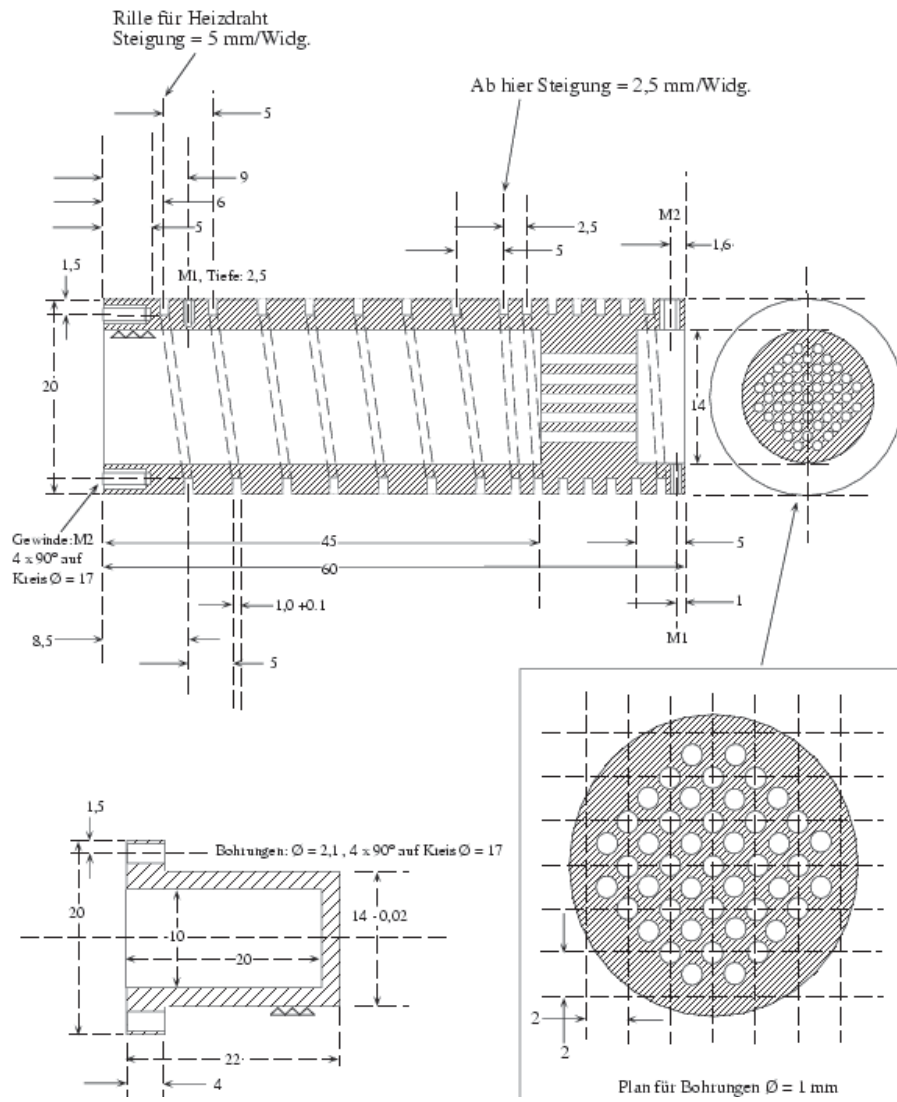


Figure C.5: Calcium oven capsule - atomic beam source

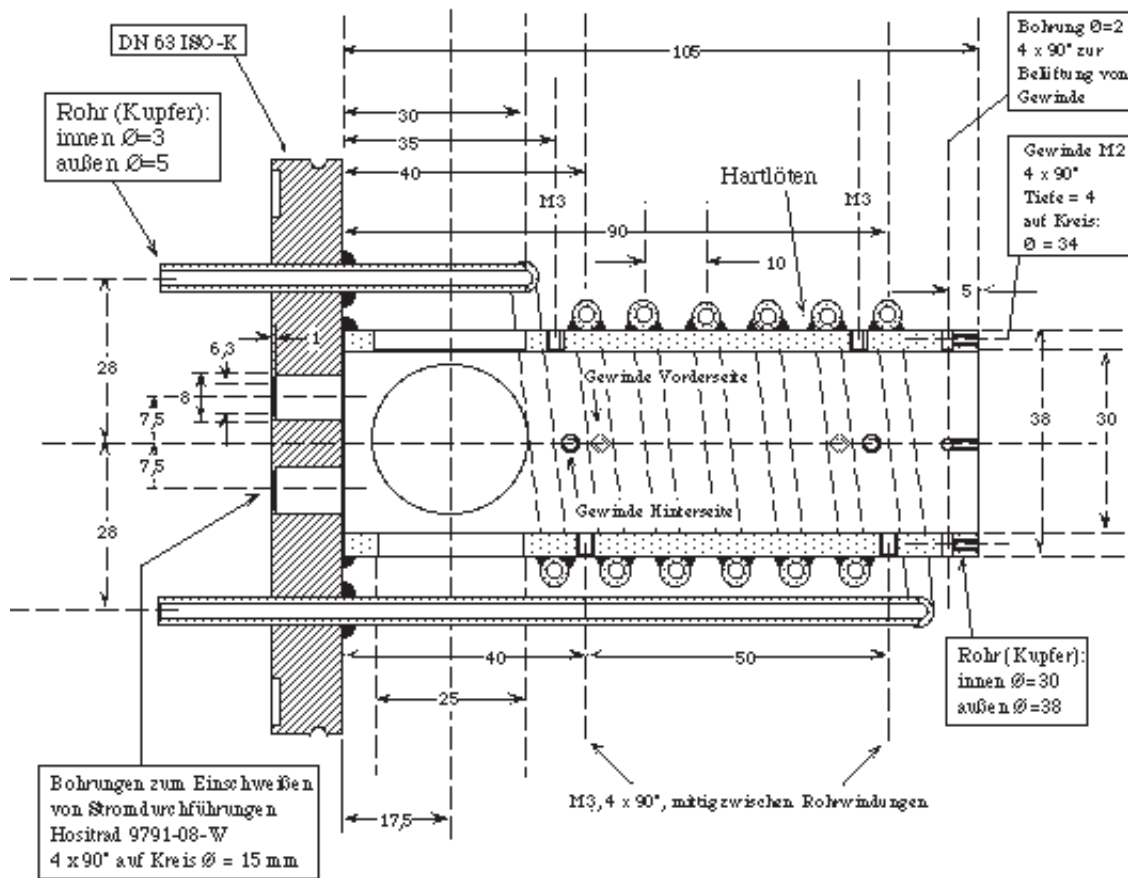
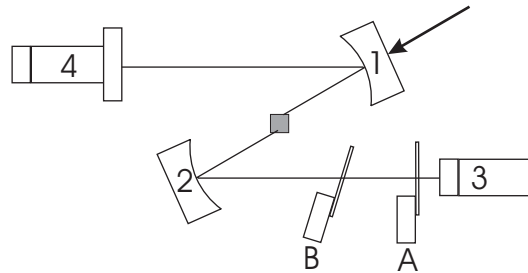


Figure C.6: Technical drawing of the heat shield that surrounds the main calcium oven

## C.2 Tm:YAG resonator adjustment (*Quehl* method)

- Position resonator well relative to the pump laser, so that Brewster reflex of crystal is minimized. This can be observed with the IR-scope which is also used to secure that the pump beam propagates symmetrically through the crystal.
- Fix resonator.  
Glue a mirror mount (A) with an attached microscope slide to the base plate, so that the slide is positioned between flat (3) and curved mirror (2), see figure. Now the pump laser wavelength is changed to a value at which the curved mirror's HT-coating is less transparent.



The beam is now well visible on the microscope slide. A second microscope slide (B) is brought into the beam between the curved mirror and the first slide.

- The first slide (A) is used as a mirror, and its reflection through slide (B) is used to return the beam onto itself.
- Adjust mirror (3) parallel to slide (A) by eyesight.
- Test if the pump laser hits mirror (3), if not adjust mirror (2) and repeat the adjustment of (A) iteratively.
- Slide (B) is removed.
- Look straight through mirror (4) with the IR-viewer. The reflection of the remaining slide as well as the reflection of mirror (3) should be visible, otherwise mirror (1) has to be adjusted. Then adjusting (3) will overlap the two reflections, and finally adjusting (1) brings them to the center of mirror (4).
- The mirror mount with the slide has to be removed *carefully*.
- The pump beam is chopped at 100 Hz, and the Tm:YAG fluorescence is observed behind mirror (4) using the  $10 \times 10$  mm PbS-detector (better than behind mirror (3), where still high pump power is found).
- Two degrees of freedom remain to be adjusted: loosen and move mirror (4) until laser action starts.
- After the laser power is optimized with all mirrors, the etalons can be installed.
- Typical power values without etalons: 75 mW @  $2\mu\text{m}$  with 750 mW @ 786 nm, threshold at 170 mW @ 786 nm
- Optimal power values without etalons: 90 mW @  $2\mu\text{m}$  with 640 mW @ 786 nm (with cooling water at the Tm:YAG crystal)



## C.3 Wavelength measurement

For a rough adjustment of the laser wavelength all lasers of the experiment can be sent into a *wave-meter* or *lambda-meter* which we built for this reason. It doesn't offer the precision to tune the laser exactly onto the atomic resonance but close enough to find the atomic line in subsequent fluorescence measurements on atomic samples. The resolution of the wave meter is  $10^{-12}$  m, the day-to-day reproducibility is better than that, and the accuracy in terms of a systematic error can only be estimated against theoretical and literature values for transition wavelengths to be in the order of several  $10^{-2}$  nm. In table C.14 the corresponding frequency accuracies  $\Delta\nu = -\frac{c}{\lambda^2} \Delta\lambda$  of the wavemeter reading are given for all wavelengths of interest to the calcium experiment. These values can be used to roughly estimate the laser detuning from the atomic resonance.

$\lambda/\text{nm}$	$\Delta\lambda/\text{nm}$	$\Delta\nu/\text{MHz}$
422	$10^{-3}$	1685
430	$10^{-3}$	1623
657	$10^{-3}$	695
671	$10^{-3}$	666
786	$10^{-3}$	486
844	$10^{-3}$	421
861	$10^{-3}$	405
1978	$10^{-3}$	77

**Table C.14:** Accuracy of wavemeter reading at wavelengths relevant to the calcium experiment

## C.4 Impedance measurement

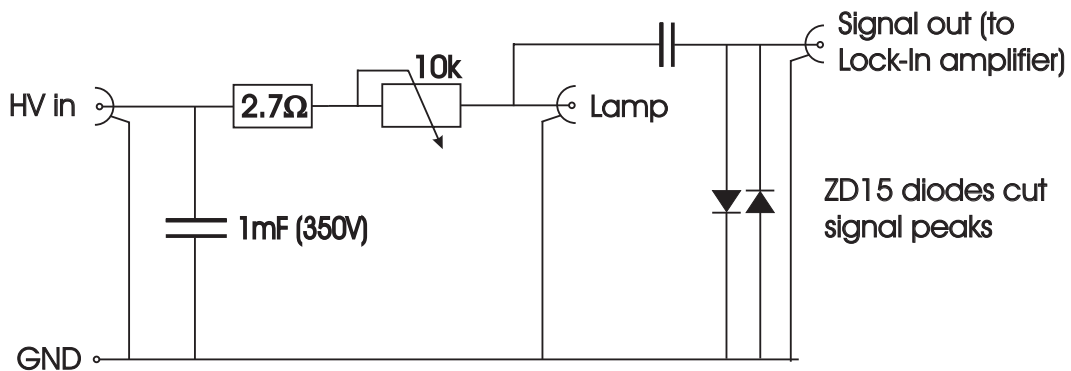


**Figure C.7:** Detection circuit for the hollow cathode lamp impedance.

The high voltage supply has to be stable — the International Power Module IHB250-1 (original supply 100 mA at 210–265 VDC) was modified to give up to 350 VDC at less current, and a 10 Hz low-pass filter was added:

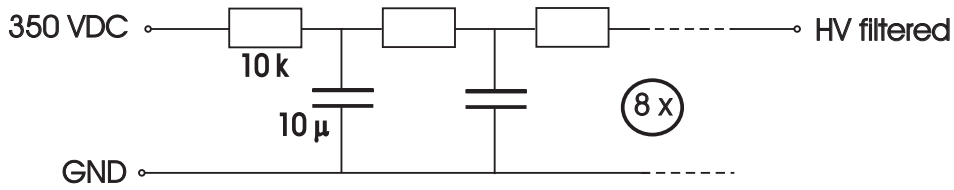


**Figure C.8:** Low pass filter ( $f_{3dB} = 10$  Hz) in high voltage power supply

## C.5 Temperature stabilization

The resistivities  $R_3$  and  $R_4$  that determine the adjustment range for the temperature set point are selected according to

$$R_4 = \frac{U_{\min}}{\Delta U} \cdot (1 \text{ k}\Omega)$$

$$R_3 = \left( \frac{10 \text{ V}}{\Delta U} - 1 \right) (1 \text{ k}\Omega) - R_4$$

Here  $\Delta U = U_{\max} - U_{\min}$  is the voltage range that can be translated into temperature with

$$U/\text{Volt} \hat{=} T/100 \text{ Kelvin.} \quad (\text{C.1})$$

# Appendix D

## Appliances and materials

**Ion Pump** StarCell VacIon Plus 55, Varian / Torino

- flange: DN 63 CF
- pumping speed (N<sub>2</sub>): 50 l/s
- lifetime @ 10<sup>-6</sup> mbar: 80000 hours
- max. starting pressure: 5 · 10<sup>-2</sup> mbar
- final pressure < 10<sup>-11</sup> mbar

**Turbo Pump** Modell HY.Cone 200, Leybold / Köln

- flanges: high vacuum side DN 100 CF, prevacuum/foreline DN 16 KF
- pumping speed (N<sub>2</sub>): 205 l/s
- 51600 rpm, 3 min startup time, M5 screw for venting
- abs. max. rating: 100°C at high vacuum flange
- max. foreline pressure: 10 mbar (security shutdown protected)

**Foreline Pump** Trivac D5E T1-31111112, Leybold / Köln

- flange: DN 16 KF
- pumping speed: 5.2 m<sup>3</sup>/h
- max. starting pressure: 5 · 10<sup>-2</sup> mbar
- final pressure 2 · 10<sup>-3</sup> mbar

**Vacuum leak detector** Ultratest UL200, Leybold / Köln

- flange: DN 16 KF
- pumping speed (He): 1 l/s
- lower detection limit < 5 · 10<sup>-11</sup> mbar l/s
- upper detection limit · 10<sup>-1</sup> mbar l/s

**Pump laser 1** Verdi Model 10 Watt, Coherent Germany / Dieburg

- head S/N V10-A2945, power supply # 906
- laser wavelength 532 nm, average diode current 24.90 A,
- temperature settings: vanadate 30°C, LBO 150.11°C, etalon 61.5°C, diode I 22.72°C, diode II 26.64°C, baseplate 28.29°C

**Pump laser 2** Verdi Modell 5 Watt, Coherent Germany / Dieburg

- head S/N V5G-A4750, power supply # 1739A
- laser wavelength 532 nm, threshold current 15.56 A, rollover 20.76 A
- temperature settings: vanadate 35°C, LBO 151.5°C, etalon 75°C, diode I 27°C, diode II 25°C

**Diode laser @ 657 nm** Type ML 1016R-01, Mitsubishi / Japan

- diode No. 98-947140 (March 14, 1998), center wavelength 659 nm
- threshold current 38 mA, operating current 81 mA, nominal power 30 mW, positive polarity,  $\theta_x = 8.6^\circ$ ,  $\theta_y = 22.4^\circ$

**Diode laser @ 671 nm** Type HL 6714G, Hitachi / Japan

- diode No. 9C0770, center wavelength 673.7 nm
- threshold current 28.3 mA,  $I_S = 0.709$  mA, nominal power 10 mW, negative polarity,  $\eta = 0.71$  mW/mA,  $\theta_{\text{horiz}} = 7.7^\circ$ ,  $\theta_{\text{vert}} = 24.2^\circ$

**Thermal power meter** MeterMate D10MM, Thorlabs / USA

- wavelength range 0.3–10.6  $\mu\text{m}$
- accuracy  $\pm 5\%$  of full scale, 10 mW resolution
- output “ $\times 100$ ”: 100 mV/W, “ $\times 1000$ ”: 1 V/W
- sensor area 2.57  $\text{cm}^2$ , aperture  $\varnothing$  18.1 mm
- max. power 10 W, max. power density 200  $\text{W}/\text{cm}^2$

**Avalanche Photodiode** APD Module C5460-01, Hamamatsu / Japan

- APD diameter 3 mm, spectral response 400–1000 nm, peak at 800 nm
- APD sensitivity 0.5 A/W (at 800 nm, gain=1)
- amplifier range DC–100 kHz (cut-off frequency at -3 dB)
- photoelectric sensitivity  $-1.5 \cdot 10^8$  V/W (incl. APD, 800 nm, default gain=30)
- minimum detection limit  $< 0.01$  nW, typ. 0.005 nW
- max. input light intensity 0.06  $\mu\text{W}$
- max. supply voltage  $\pm 16$  V, max. operating range 0–60°C

**Photo Multiplier Tube** R928, Hamamatsu / Japan

- spectral response 185–900 nm, peak at 400 nm
- anode gain typ.  $10^7$  (at 800 nm, gain=1)
- typ. anode sensitivity: 2500 A/lm and  $7.4 \cdot 10^5$  A/W
- anode dark current after 30 min.: typ. 3 nA, max. 50 nA
- anode to cathode voltage: 1000 Vdc, max. 1250 Vdc
- max. avg. anode current: 0.1 mA

**Digital oscilloscope** LeCroy 9314C, LeCroy / USA

- -3 dB bandwidth: DC to 400 MHz @ 50  $\Omega$ , DC to 230 MHz @ 1 M $\Omega$
- four channels and digitizers, 50k acqu. memory / channel
- max. sampling rate 100 MS/s on each channel
- sensitivity 2 mV/div to 5 V/div; DC accuracy  $\pm 2\%$  full scale
- 1 ns/div to 1000 s/div; clock accuracy  $\leq \pm 0.002\%$

**Signal analyzer** Advantest R4131D

- 10 kHz to 3.5 GHz, input 50 $\Omega$
- abs. max. ratings +20 dBm and  $\pm 25$  VDC

**Lock-in amplifier** SR 530, Stanford Research Systems / USA

- 0.5 Hz to 100 kHz, 80 dB dynamic reserve
- auto-phasing, band filter, noise 7 nV/ $\sqrt{\text{Hz}}$  at 1 kHz
- single-ended and differential voltage inputs
- voltage input impedance 100 M $\Omega$  and 25 pF, ac coupled
- current input  $10^6$  V/A, impedance 1 k $\Omega$  to virtual GND, noise measurement
- oscillator output: 1 Hz up to 100 kHz
- 100 dB common mode rejection dc to 1 kHz for 1 Volt peak

**High current power supply** PhyWe 25 VAC, Germany

- Primary coil (75 turns): max. 12 Amp
- Secondary coils (6 turns): max. 120 Amp

# Bibliography

- [1] B.P. Anderson and M.A. Kasevich, Macroscopic quantum interference from atomic tunnel arrays, *Science* **282** (1998), 1686–1689.
- [2] M.H. Anderson, J.R. Ensher, M.R. Matthews, C.E. Wieman, and E.A. Cornell, Observation of Bose-Einstein condensation in a dilute atomic vapor, *Science* **269** (1995), 198.
- [3] E. Arimondo, W.D. Philips, and F. Strumia (Eds.), *Laser Manipulation of atoms and ions*, Proceedings of the International School of Physics ENRICO FERMI, vol. Course CXVIII, Varenna 1991, North Holland, Amsterdam, 1992.
- [4] A. Aspect, E. Arimondo, R. Kaiser, n. Vansteenkiste, and C. Cohen-Tannoudji, Laser cooling below the one-photon recoil energy by velocity-selective coherent population trapping, *Phys. Rev. Lett.* **61** (1988), no. 7, 826–829.
- [5] A. Aspect, W. Barletta, and R. Bonifacio (Eds.), *Coherent and Collective Interactions of Particles and Radiation Beams*, Proceedings of the International School of Physics ENRICO FERMI, vol. Course CXXXI, Varenna 1995, IOS Press, Amsterdam, 1996.
- [6] M.D. Barrett, J.A. Sauer, and M.S. Chapman, All-optical formation of an atomic Bose-Einstein condensate, *Phys. Rev. Lett.* **87** (2001), no. 1, 010404.
- [7] C.W. Bauschlicher Jr., S.R. Langhoff, and H. Partridge, The radiative lifetime of the  $^1D_2$  state of Ca and Sr: a core-valence treatment, *J. Phys. B* **18** (1985), 1523–1532.
- [8] H.O. Behrens, G.H. Guthörlein, and B. Hähner, *Optogalvanische Spektroskopie, Laser und Optoelektronik* **14** (1982), no. 1, 26.
- [9] N. Beverini, F. Giammanco, E. Maccioni, F. Strumia, and G. Vissani, Measurement of the calcium  $^1P_1-^1D_2$  transition rate in a laser-cooled atomic beam, *J. Opt. Soc. Am. B* **6** (1989), no. 11, 2188–2193.
- [10] T. Binnewies, U. Sterr, J. Helmcke, and F. Riehle, Cooling by Maxwell’s demon: Preparation of single-velocity atoms for matter-wave interferometry, *Phys. Rev. A* **62** (2000), 011601(R).

- [11] T. Binnewies, G. Wilpers, U. Sterr, F. Riehle, J. Helmcke, T.E. Mehlstäubler, E.M. Rasel, and W. Ertmer, Doppler cooling and trapping on forbidden transitions, *Phys. Rev. Lett.* **87** (2001), no. 12, 123002.
- [12] G.C. Bjorklund, M.D. Levenson, W. Lenth, and C. Ortiz, Frequency Modulation (FM) spectroscopy, *Appl. Phys. B* **32** (1983), 145–152.
- [13] I. Bloch, T.W. Hänsch, and T. Esslinger, Atom laser with a cw output coupler, *Phys. Rev. Lett.* **82** (1999), no. 15, 3008–3011.
- [14] M. Bode, I. Freitag, A. Tünnermann, and H. Welling, Frequency-tunable 500-mW continuous-wave source Doubling with  $\text{KNbO}_3$  in an external cavity, *Opt. Lett.* **16** (1991), no. 18.
- [15] S.N. Bose, Plancks Gesetz und die Lichtquantenhypothese, *Zeitschrift für Physik* **26** (1924), 178–181.
- [16] G.D. Boyd and D.A. Kleinman, Parametric interaction of focused Gaussian light beams, *J. Appl. Phys.* **39** (1968), no. 8, 3597.
- [17] C.C. Bradley, C.A. Sackett, J.J. Tollett, and R.G. Hulet, Evidence of Bose-Einstein condensation in an atomic gas with attractive interactions, *Phys. Rev. Lett.* **75** (1995), no. 9, 1687–1690.
- [18] I.N. Bronštejn, *Taschenbuch der Mathematik*, third ed., Verlag Harri Deutsch, Frankfurt am Main, 1997, ISBN 3-8171-2003-6.
- [19] A. Browaeys, A. Robert, O. Sirjean, J. Poupard, S. Nowak, D. Boiron, C.I. Westbrook, and A. Aspect, Thermalization of magnetically trapped metastable helium, *arXiv:physics* (2001), 0102068.
- [20] J.P. Burke Jr., C.H. Greene, and J.L. Bohn, Multichannel cold collisions: simple dependences on energy and magnetic field, *Phys. Rev. Lett.* **81** (1998), no. 16, 3355–3358.
- [21] Keith Burnett (ed.), *Coherent matter waves*, *J. Phys. B: At. Mol. Opt. Phys.* **33** (2000), no. 19, special issue for articles on coherent matter wave research.
- [22] S. Chu, Nobel Lecture: The manipulation of neutral particles, *Rev. Mod. Phys.* **70** (1998), no. 3, 685–706.
- [23] S. Chu, L. Hollberg, J.E. Bjorkholm, A. Cable, and A. Ashkin, Three-dimensional viscous confinement and cooling of atoms by resonance radiation pressure, *Phys. Rev. Lett.* **55** (1985), no. 1, 48–51.
- [24] A. Clairon, P. Laurent, G. Santarelli, S. Ghezali, S.N. Lea, M. Bahoura, E. Simon, S. Weyers, and K. Szymaniec, Proceedings of the fifth Symposium on frequency standards and metrology, Woods Hole, USA, ch. Preliminary accuracy evaluation of a cesium fountain frequency standard, J. Bergquist, World Scientific, 1996.

- [25] A. Clairon, C. Salomon, S. Guellati, and W. Phillips, Ramsey resonance in a Zacharias fountain, *Euro. Phys. Lett.* **16** (1991), 165.
- [26] R.B.M. Clarke, T. Graf, and E. Riis, Dipole traps with mode-locked lasers, *Appl. Phys. B* **70** (2000), 695–700.
- [27] C. Cohen-Tannoudji, Nobel Lecture: Manipulating atoms with photons, *Rev. Mod. Phys.* **70** (1998), no. 3, 707–719.
- [28] C.J. Cooper, G. Hillenbrand, J. Rink, C.G. Townsend, K.P. Zetie, and C.J. Foot, The temperature of atoms in a magneto-optical trap, *Europhys. Lett.* **28** (1994), no. 6, 397–402.
- [29] Alan Corney, *Atomic and laser spectroscopy*, Oxford Science Publications, Oxford University Press, Oxford, 1979.
- [30] E.A. Curtis, C.W. Oates, and L. Hollberg, Quenched narrow-line laser cooling of  $^{40}\text{Ca}$  to near the photon recoil limit, *Phys. Rev. A* **64** (2001), 031403(R).
- [31] J. Dalibard and C. Cohen-Tannoudji, Laser cooling below the Doppler limit by polarization gradients - simple theoretical models, *J. Opt. Soc. Am. B* **6** (1989), 2023–2045.
- [32] K.B. Davis, M.O. Mewes, M.R. Andrews, N.J. van Druten, D.S. Durfee, D.M. Kurn, and W. Ketterle, Bose-Einstein condensation in a gas of sodium atoms, *Phys. Rev. Lett.* **75** (1995), no. 22, 3969–3973.
- [33] Wolfgang Demtröder, *Laserspektroskopie*, 3rd ed., Springer-Verlag, Berlin, Heidelberg, 1993.
- [34] A. Derevianko, Feasibility of cooling and trapping metastable alkaline-earth atoms, *Phys. Rev. Lett.* **87** (2001), 023002.
- [35] A. Derevianko and A. Dalgarno, Long-range interaction of two metastable rare-gas atoms, *Phys. Rev. A* **62** (2000), 062501.
- [36] T.P. Dinneen, K.R. Vogel, E. Arimondo, J.L. Hall, and A. Gallagher, Cold collision of  $\text{Sr}^*$ -Sr in a magneto-optical trap, *Phys. Rev. A* **59** (1999), no. 2, 1216–1222.
- [37] R.W.T. Drever et al., Laser phase and frequency stabilization using an optical resonator, *Appl. Phys. B* **31** (1983), 97.
- [38] A. Einstein, *Phys. Z.* **18** (1917), 121, by English translation in *Sources of Quantum Mechanics*, 1967, edited by B. L. Waerden (North-Holland, Amsterdam), pp. 63–78.
- [39] A. Einstein, Quantentheorie des einatomigen idealen Gases, *Sitz. Ber. Preuss. Akad. Wiss. (Berlin)* **22** (1924), 261.
- [40] D. Frese, B. Ueberholz, S. Kuhr, W. Alt, D. Schrader, V. Gomer, and D. Meschede, Single atoms in an optical dipole trap: towards a deterministic source of cold atoms, *Phys. Rev. Lett.* **85** (2000), no. 18, 3777–3780.



- [41] D.G. Fried, T.C. Killian, L. Willmann, D. Landhuis, S.C. Moss, D. Kleppner, and T.J. Greytak, Bose-Einstein condensation of atomic hydrogen, *Phys. Rev. Lett.* **81** (1998), no. 18, 3811–3814.
- [42] A. Gallagher and D.E. Pritchard, Exoergic collisions of cold  $\text{Na}^*$ -Na, *Phys. Rev. Lett.* **63** (1989), no. 9, 957–960.
- [43] J.R. Gardner, R.A. Cline, J.D. Miller, D.J. Heinzen, H.M.J.M. Boesten, and B.J. Verhaar, Collisions of doubly spin-polarized, ultracold  $^{85}\text{Rb}$  atoms, *Phys. Rev. Lett.* **74** (1995), no. 19, 3764–3767.
- [44] S.D. Gensemer and P.L. Gould, Ultracold collisions observed in real time, *Phys. Rev. Lett.* **80** (1998), no. 5, 936–939.
- [45] E.V. Goldstein, M.G. Moore, and P. Meystre, Nonlinear manipulation and control of matter waves, *Laser Physics* **10** (2000), 8.
- [46] R. Grimm, M. Weidemüller, and Y.B. Ovchinnikov, Optical dipole traps for neutral atoms, *Adv. At. Mol. Opt. Phys.* **42** (2000), 95–170.
- [47] J. Grünert and A. Hemmerich, Optimizing the production of metastable calcium atoms in a magneto-optical trap, *Applied Physics B* **73** (2001), 815–818.
- [48] J. Grünert, G. Quehl, V. Elman, and A. Hemmerich, Ultracold metastable calcium ensembles, a medium for matter wave amplification?, *J. Mod. Opt.* **47** (2000), 2733–2740.
- [49] J. Grünert, S. Ritter, and A. Hemmerich, Sub-Doppler magneto-optical trap for calcium, *Phys. Rev. A* **65** (2002), 041401(R).
- [50] D.J. Han, R.H. Wynar, Ph. Courteille, and D.J. Heinzen, Bose-Einstein condensation of large numbers of atoms in a magnetic time-averaged orbiting potential trap, *Phys. Rev. A* **57** (1998), no. 6, R4114–R4117.
- [51] T.W. Hänsch and A.L. Schawlow, Cooling of gases by laser radiation, *Optics Communications* **13** (1975), no. 1, 68–69.
- [52] A. Hemmerich, Lecture on Laser Cooling, Skriptum, 1998/99, University of Hamburg.
- [53] Guido Henning, Laserkühlung und Einfang von Magnesium-Atomen in einer magneto-optischen Strahlungsdruckfalle, Ph.D. thesis, Universität Bonn, 1992.
- [54] H.F. Hess, Evaporative cooling of magnetically trapped and compressed spin-polarized hydrogen, *Phys. Rev. B* **34** (1986), 3476.
- [55] A. Hohla, V. Vuletic, T.W. Hänsch, and C. Zimmermann, Bichromatic frequency conversion in potassium niobate, *Opt. Lett.* **23** (1998), no. 6, 436–438.

- [56] R. Holzwarth, Th. Udem, T.W. Hänsch, J.C. Knight, W.J. Wadsworth, and P. St. J. Russell, Optical Frequency Synthesizer for Precision Spectroscopy, *Phys. Rev. Lett.* **85** (2000), 2264.
- [57] Paul Horowitz and Winfield Hill, *The art of electronic*, second ed., Cambridge University Press, Cambridge, 1989.
- [58] L.R. Hunter, G.M. Watson, D.S. Weiss, and A.G. Zajonc, High-precision measurement of lifetimes and collisional decay parameters in Ca  $^1D$  states using the two-photon Hanle effect, *Phys. Rev. A* **31** (1985), no. 4, 2268–2278.
- [59] T. Ido, Y. Isoya, and H. Katori, Optical-dipole trapping of Sr atoms at a high phase-space density, *Phys. Rev. A* **61** (2000), R061403.
- [60] M. Inguscio, S. Stringari, and C.E. Wieman (Eds.), *Bose-Einstein condensation in atomic gases*, Proceedings of the International School of Physics ENRICO FERMI, vol. Course CXL, Varenna 1998, IOS Press, Amsterdam, 1999.
- [61] U. Janicke and M. Wilkens, Atomic matter wave amplification by optical pumping, *Adv. At. Mol. Opt. Phys.* **41** (1998), 261–304.
- [62] M. Kasevich and S. Chu, Laser cooling below a photon recoil with three-level atoms, *Phys. Rev. Lett.* **69** (1992), no. 12, 1741–1744.
- [63] H. Katori, T. Ido, Y. Isoya, and M. Kuwata-Gonokami, Magneto-optical trapping and cooling of strontium atoms down to the photon recoil temperature, *Phys. Rev. Lett.* **82** (1999), no. 6, 1116–1119.
- [64] H. Katori, T. Ido, and M. Kuwata-Gonokami, Optimal design of dipole potentials for efficient loading of Sr atoms, *J. Phys. Soc. Jap.* **68** (1999), no. 8, 2479–2482.
- [65] Peter Kersten, *Ein transportables optisches Calcium-Frequenznormal*, PTB-Bericht, Universität Kaiserslautern, März 1998, ISBN 3-89701-133-6.
- [66] M.A. Khashan and A.Y. Nassif, Dispersion of the optical constants of quartz and polymethyl methacrylate glasses in a wide spectral range:  $0.2 - 3 \mu\text{m}$ , *Optics Communications* **188** (2001), 129–139.
- [67] D. King, P. Schenck, K. Smith, and J. Travis, Direct calibration of laser wavelength and bandwidth using the optogalvanic effect in hollow cathode lamps, *Appl. Opt.* **16** (1977), 2617.
- [68] T. Kisters, K. Zeiske, F. Riehle, and J. Helmcke, High-resolution spectroscopy with laser-cooled and trapped calcium atoms, *Applied Physics B* **59** (1994), 89–98.
- [69] Donald E. Knuth, *The T<sub>E</sub>Xbook*, Addison-Wesley Publishing Company, 1984.
- [70] H. Kogelnik and T. Li, Laser Beams and Resonators, *Applied Optics* **5** (1966), no. 10, 1550–1566.

- [71] T. Kurosu, M. Morinaga, and F. Shimizu, Observation of the Ca  $4s^1S_0$ - $4p^3P_1$  transition in continuous free-falling cold atomic flow from an atom trap, *Jpn. J. Appl. Phys.* **31** (1992), L273–L275.
- [72] T. Kurosu and F. Shimizu, Laser cooling and trapping of calcium and strontium, *Jpn. J. Appl. Phys., Part 2* **29** (1990), L2127–L2129.
- [73] T. Kurosu and F. Shimizu, Laser cooling and trapping of alkaline earth atoms, *Jpn. J. Appl. Phys.* **31** (1992), 908–912.
- [74] R.L. Kurucz and B. Bell, 1995 Atomic Line Data, CD-ROM No. **23**, Smithsonian Astrophysical Observatory, Cambridge, Mass., 1995, <http://cfa-www.harvard.edu/amdata/ampdata/kurucz23/sekur.html>.
- [75] Leslie Lamport,  $\text{\LaTeX}$ : A Document Preparation System, Addison-Wesley Publishing Company, 1986.
- [76] Landolt-Börnstein, Eigenschaften der Materie in ihren Aggregatzuständen, 2. Teil: Gleichgewichte ausser Schmelzgleichgewichten, Bandteil a (Gleichgewichte Dampf-Kondensat und osmotische Phänomene), vol. II, Springer, 1960.
- [77] J. Lawall, S. Kulin, B. Saubamea, N. Bigelow, M. Leduc, and C. Cohen-Tannoudji, Three-dimensional laser cooling of helium beyond the single-photon recoil limit, *Phys. Rev. Lett.* **75** (1995), no. 23, 4195–4197.
- [78] L.P. Lellouch and L.R. Hunter, Measurement of the  $4s4p\ ^1P$ - $4s3d\ ^1D$  spontaneous emission rate in calcium by use of a Stark-electric-quadrupole interference, *Phys. Rev. A* **36** (1987), no. 7, 3490–3493.
- [79] P.J. Leo, V. Venturi, I.B. Whittingham, and J.F. Babb, Ultracold collisions of metastable helium atoms, *arXiv:physics* (2001), 0011072v2.
- [80] P. Lett, R. Watts, C. Westbrook, W. Phillips, P. Gould, and H. Metcalf, Observation of atoms laser cooled below the Doppler limit, *Phys. Rev. Lett.* **61** (1988), 169.
- [81] Z.T. Lu, K.L. Corwin, M.J. Renn, M.H. Anderson, E.A. Cornell, and C.E. Wieman, Low-velocity intense source of atoms from a magneto-optical trap, *Phys. Rev. Lett.* **77** (1996), no. 16, 3331–3334.
- [82] W.W. MacAlpine and R.O. Schildknecht, Coaxial resonators with helical inner conductor, *Proc. of the IRE* (1959), 2099–2105.
- [83] M. Machholm, P.S. Julienne, and K.-A. Suominen, Collisions of cold magnesium atoms in a weak laser field, *Phys. Rev. A* **59** (1999), R4113–R4416.
- [84] M. Machholm, P.S. Julienne, and K.-A. Suominen, Calculations of collisions between cold alkaline earth atoms in a weak laser field, *Phys. Rev. A* **64** (2001), 033425.
- [85] F. Malecki and P. Malecki, DicData universal, cd-rom-produktion Malecki, Dachau, 2000.

- [86] Harold J. Metcalf and Peter van der Straten, *Laser cooling and trapping*, Springer-Verlag, New York, Berlin, Heidelberg, 1999.
- [87] M.-O. Mewes, M.R. Andrews, D.M. Kurn, D.S. Durfee, C.G. Townsend, and W. Ketterle, Output coupler for Bose-Einstein condensed atoms, *Phys. Rev. Lett.* **78** (1997), 582.
- [88] H.-J. Miesner and W. Ketterle, Bose-Einstein condensation in dilute atomic gases, *Solid State Comm.*, vol. 107, 1998, Proceedings of the Symposium on “The Advancing Frontiers of Condensed Matter Science”, Philadelphia, Oct. 13-14, 1997., pp. 629–637.
- [89] J. Mitroy, Energy levels and oscillator strengths for neutral calcium, *J. Phys. B: At. Mol. Opt. Phys.* **26** (1993), 3703–3718.
- [90] John H. Moore, Christopher C. Davis, and Michael A. Coplan, *Building Scientific Apparatus*, second ed., Addison-Wesley Publishing Company, 1989.
- [91] G. Morigi, J. Eschner, and C. Keitel, Ground state laser cooling using electromagnetically induced transparency, *Phys. Rev. Lett.* **85** (2000), 4458.
- [92] C.W. Oates, F. Bondu, R.W. Fox, and L. Hollberg, A diode-laser optical frequency standard based on laser-cooled Ca atoms: Sub-kilohertz spectroscopy by optical shelving detection, *Eur. Phys. J. D* **7** (1999), 449–460.
- [93] C.W. Oates, E.A. Curtis, and L. Hollberg, Improved short-term stability of optical frequency standards: approaching 1 Hz in 1 s with the Ca standard at 657 nm, *Opt. Lett.* **25** (2000), no. 21, 1603–1605.
- [94] F. Pereira Dos Santos, J. Leonard, Junmin Wang, C.J. Barrelet, F. Perales, E. Rasel, C.S. Unnikrishnan, M. Leduc, and C. Cohen-Tannoudji, Bose-Einstein condensation of metastable helium, *arXiv:cond-mat* (2001), 0103387.
- [95] W.D. Phillips, Nobel Lecture: Laser cooling and trapping of neutral atoms, *Rev. Mod. Phys.* **70** (1998), no. 3, 721–741.
- [96] E.S. Polzik and H.J. Kimble, Frequency Doubling with  $\text{KNbO}_3$  in an external cavity, *Opt. Lett.* **16** (1991), no. 18.
- [97] S.G. Porsev, M.G. Kozlov, Yu.G. Rakhlina, and A. Derevianko, Many-body calculations of electric-dipole amplitudes for transitions between low-lying levels of Mg, Ca, and Sr, *PRA* **64** (2001), 012508.
- [98] M. Prentiss and A. Cable, Slowing and cooling an atomic beam using an intense optical standing wave, *Phys. Rev. Lett.* **62** (1989), no. 12, 1354–1357.
- [99] G. Quehl, J. Grünert, V. Elman, and A. Hemmerich, A tunable dual frequency Tm:YAG laser, *Optics Communications* **190** (2001), 303–307.

- [100] E. Raab, M. Prentiss, A. Cable, S. Chu, and D. Pritchard, Trapping of neutral sodium atoms with radiation pressure, *Phys. Rev. Lett.* **59** (1987), no. 23, 2631–2634.
- [101] R.J. Rafac, B.C. Young, J.A. Beall, W.M. Itano, D.J. Wineland, and J.C. Bergquist, Sub-dekahertz ultraviolet spectroscopy of  $^{199}\text{Hg}^+$ , *Phys. Rev. Lett.* **85** (2000), 2462.
- [102] N.F. Ramsey, *Molecular Beams*, Clarendon Press, Oxford, 1956.
- [103] L. Ricci, M. Weidemüller, T. Esslinger, A. Hemmerich, C. Zimmermann, V. Vuletic, W. König, and T.W. Hänsch, A compact grating-stabilized diode laser system for atomic physics, *Optics Communications* **117** (1995), 541–549.
- [104] Stephan Ritter, *Entwicklung präziser Laserlichtquellen für Experimente mit ultrakalten Calciumatomen*, Master's thesis, Universität Hamburg, März 2002.
- [105] F. Ruschewitz, J.L. Peng, H. Hinderthür, N. Schaffrath, K. Sengstock, and W. Ertmer, Sub-Kilohertz optical spectroscopy with a time domin atom interferometer, *Phys. Rev. Lett.* **80** (1998), 3173–3176.
- [106] Jean-Paul Sartre, *L'êtré et le néant*, 22. ed., Bibliothèque des idées, nrf, Librairie Gallimard, Paris, 1949.
- [107] Adrien Schoof, *Entwicklung eines ultrastabilen Laserdiodensystems bei 657 nm für die Metrologie*, Master's thesis, Universität Hamburg, March 2001.
- [108] Adrien Schoof, Jan Grünert, Stephan Ritter, and Andreas Hemmerich, Reducing the linewidth of a diode laser below 30 Hz by stabilization to a reference cavity with a finesse above  $10^5$ , *Opt. Lett.* **26** (2001), no. 20, 1562–1564.
- [109] S-Q. Shang, B. Sheeny, and H. Metcalf, Velocity-selective resonances and sub-Doppler laser cooling, *Phys. Rev. Lett.* **67** (1991), no. 9, 1094–1097.
- [110] Anthony E. Siegman, *Lasers*, University Science Books, Mill Valley, California, 1986.
- [111] SMI, *Periodic Table 3.0b*, SMI Corporation, Tulsa, Oklahoma, 1995.
- [112] R. Spreeuw, T. Pfau, U. Janicke, and M. Wilkens, Laser-like scheme for atomic matter waves, *Europhys. Lett.* **32** (1995), 469.
- [113] S. Stenholm, The semiclassical theory of laser cooling, *Rev. Mod. Phys.* **58** (1999), no. 3, 699–739.
- [114] R.C. Stoneman and L. Esterowitz, Efficiently, broadly tunable, laser-pumped Tm:YAG and Tm:YSGG cw lasers, *Opt. Lett.* **15** (1990), no. 9, 486–488.
- [115] A.R. Striganov and N.S. Sventitskii, *Tables of spectral lines of neutral and ionized atoms*, Plenum, New York, 1968, Translated from Russian.
- [116] F. Strumia, Application of laser cooling to the atomic frequency standards, *Laser Science and Technology* (A.N. Chester and S. Marellucci, eds.), Plenum, New York, 1988, pp. 367–401.

- [117] Orazio Svelto, *Principles of Lasers*, Plenum Press, New York, 1998.
- [118] C.G. Townsend, N.H. Edwards, C.J. Cooper, K.P. Zetie, C.J. Foot, A.M. Steane, P. Szriftgiser, H. Perrin, and J. Dalibard, Phase-space density in the magneto-optical trap, *Phys. Rev. A* **52** (1995), no. 2, 1423–1440.
- [119] Th. Udem, S.A. Diddams, K.R. Vogel, C.W. Oates, E.A. Curtis, W.D. Lee, W.M. Itano, R.E. Drullinger, J.C. Bergquist, and L. Hollberg, Absolute frequency measurements of the  $\text{Hg}^+$  and Ca optical clock transitions with a femtosecond laser, *Phys. Rev. Lett.* **86** (2001), 4996.
- [120] K.R. Vogel, T.P. Dinneen, A. Gallagher, and J.L. Hall, *IEEE Trans. Instrum. Meas.* **48** (1999), 618.
- [121] John Wallace, Laser diode has linewidth below 30 Hz, *Laser Focus World* (2001).
- [122] R.C. Weast, M.J. Astle, and W.H. Beyer, *CRC Handbook of Chemistry and Physics*, 69 ed., CRC Press, Boca Raton, Florida, 1988–1989.
- [123] J. Weiner, V.S. Bagnato, S. Zilio, and P.S. Julienne, Experiments and theory in cold and ultracold collisions, *Rev. Mod. Phys.* (1999), no. 71, 1.
- [124] D. Wineland and H. Dehmelt, Proposed  $10^{14} \Delta \nu < \nu$  laser fluorescence spectroscopy on  $\text{Ti}^+$  mono-ion oscillator III, *Bull. Am. Phys. Soc.* **20** (1975), 637.
- [125] A. Witte, T. Kisters, F. Riehle, and J. Helmcke, Laser cooling and deflection of a Ca atomic beam, *J. Opt. Soc. Am. B* **9** (1992), 1030–1037.
- [126] B.C. Young, F.C. Cruz, W.M. Itano, and J.C. Bergquist, Visible lasers with subhertz linewidths, *Phys. Rev. Lett.* **82** (1999), no. 19, 3799–3802.
- [127] C. Zimmermann, A. Hemmerich, and T.W. Hänsch, Generation of Blue and Ultraviolet Light by Frequency Doubling of Semiconductor Laser Radiation, *Festkörperprobleme / Advances in Solid State Physics* **34** (1994), 51–63.
- [128] C. Zimmermann, V. Vuletic, A. Hemmerich, L. Ricci, and T.W. Hänsch, Design for a compact tunable Ti:sapphire laser, *Opt. Lett.* **20** (1995), no. 3, 297–299.
- [129] G. Zinner, T. Binnewies, F. Riehle, and E. Tiemann, Photoassociation of cold Ca atoms, *Phys. Rev. Lett.* **85** (2000), no. 11, 2292–2295.

# Index

- ABCD-law, 41
- abundance, *see* natural abundance
- adjustment procedure, 128
- angel's hair, 51
- AOM, 57
- apatite, 114
- atom laser, 15
- atom optics, 15
- atomic flux, 32
  
- baking, 37
- beam
  - parameter, 40
  - waist, 41
- beam scanner, [48](#), 68
- Bose-Einstein condensate, 14
- boser, 15
- branching ratio, 18, 25
  
- calcium, 114
- calcium cell, 57
- capture range, 84
- chopper, [65](#), 71
- coherent matter wave, 15
- coil(s)
  - anti-Helmholtz, 81
  - compensation, 78
  - dimensions of, 120
  - MOT, 83
  - outcoupling, 78
  - Zeeman, 33
- cold ends, 29
- conductivity
  - gas, 33
  - thermal, 114
- cooling
  - Doppler, 85, 100, 113
  - evaporative, [14](#), 109
  - laser, 13, [74](#), 81
  - polarization gradient, 85, 102, 109
  - quench, 24
  - Raman, 14
  - Sisyphus, 14, 85
  - sub-Doppler, 85
  - transverse, 33
  - Zeeman, 26, 27
- cooling water, 50, 120
  
- deceleration, 75
- detector, [71](#), 94, 123
- discharge lamp, 66
- dressed atom, 110
- dual frequency operation, 46, 60
  
- Earnshaw-Theorem, 81
- EIT, 16
- EOM, 53, 68, [122](#)
- equivalence picture, 41
- excitation probability, [74](#), 75, 90, [119](#)
  
- Fabry-Perot etalon, 45, 70, 119, 124
- finesse, 46
- fluctuations, 79
- fluorite, 114
- FM-modulation, 64
- foreline vacuum, 26
- frequency
  - doubling, 49, 52
  - shifting, 52, 56
  - stabilization, 51, [53](#), 57, 68
  
- g*-factors, 95, [115](#)
- gas discharge lamp, 65
- gate valve, 32, 34, 36
- Gaussian beams, 41
- grating, [64](#), 67
- gravitation, 83, 86

- gypsum, 114
- heating
  - transverse, 76
- high current supply, 133
- high voltage supply, 125
- impedance, 129
- improvements, 108
- indium, 33, 35
- inductivity, 79, 83
- inelastic collisions, 17, 87, 92
- infrared
  - detectors, 71
  - fluorescence, 93
  - laser, 96
  - power, 59
  - transition, 12, 24
- intercombination line, 18–20, 22, 24, 69, 109, 113
- lambda-meter, 63, 129
- lamp, 65
- Landé, *see g*-factors
- Larmor frequency, 95, 115
- laser
  - diode, 64, 67
  - pump, 49
  - Ti:sapphire, 44
  - Tm:YAG, 59
- laser beams
  - diameter of, 87, 90
  - height of, 73
- lifetime
  - natural
    - calculated, 116
    - trap, 87, 90, 97
- light carpet method, 105
- light shift, 110, 110
- light sources, 40
- limestone, 114
- linewidth
  - laser, 50, 59
  - natural, 23, 57, 69, 75, 102, 110, 116
  - power-broadened, 84, 102, 119
- Littrow configuration, 64
- loading rate, 88, 91, 93, 108
- losses
  - linear, 88
  - quadratic, 91
- Lucas description, 32
- magnetizability, 34
- main chamber, 34
- MAO, 16, 91, 108
- Maxwell's demon, 94
- metastable, 24, 65
- mode competition, 45
- mode matching, 43
- natural abundance, 23, 115
- optical
  - molasses, 13, 87
  - pumping, 16, 24, 94, 97
- oscillator strength, 110, 116, 119
- oven, 27, 87, 122, 126
- paraxial optics, 41
- PMT, 71, 97, 133
- precooling, 74, 77
- pump
  - foreline, 27, 131
  - ion-, 57, 131
  - turbo-molecular, 28, 36, 38, 131
- pump power, 47, 59, 62
- Quehl, 128
- Rabi frequency, 75, 119
- rate equations, 90
- recapture method, 100
- reservoir state, 16
- resistivity, 118
- resolved sideband cooling, 20, 112
- resonator
  - bow-tie, 41
  - concentric, 43
  - confocal, 43, 46
  - stability of, 41
  - standing-wave, 45
  - ultrahigh-finesse, 68
- rethermalization, 112



- saturation
  - intensity, 75
  - parameter, 75, 87, 88, 119
- single-mode, 64
- slowing distance, 75
- sodium, 14
- source chamber, 26
- spectroscopy
  - absorption, 57
  - Doppler width, 100
  - NMR-, 150
  - of the atomic transition, 69
  - optogalvanic, 65
  - polarization, 65
  - saturation, 96
- stabilization
  - polarization, 97
  - Pound-Drever-Hall, 53, 68
  - side-of-fringe, 52, 59
  - temperature, 130
- steady-state fluorescence, 97
- steel, 34
  
- temperature, 100, 103, 112
  - Doppler, 23, 85
  - limit, 109
  - recoil, 23, 85
  - sub-Doppler, 85
  - transverse, 76
- time-of-flight, 72, 100, 105
- transfer matrix, 41
- transfer rate, 108
- transition wavelength, 23, 116
- trap
  - dipole, 16, 111
    - far-off-resonance, 18
  - ground-state, 18, 88
  - magneto-optical, 13, 81
  - metastable, 18, 72, 85, 93
  - TOP, 15
  - vapor cell, 27
  
- vacuum
  - master equation, 37
  - quality, 38
  - system, 26
- vapor pressure, 28, 115
- velocity
  - capture, 77, 84, 150
  - mean, 31, 86
  - mean atomic, 30
  - most probable, 31, 88
  - recoil, 28
  - transverse, 59, 77
- Verdi, 49, 60, 125, 132
- vibration, 28
- viewports, 28, 34, 109
- VSCPT, 14
- VSR, 14
  
- walk-off, 45
- wave-meter, *see* lambda-meter
  
- Zeeman slower field, 77

# Publications

- J. Grünert, S. Ritter, and A. Hemmerich, *Sub-Doppler magneto-optical trap for calcium*, Phys. Rev. A **65**, 041401(R) (2002).
- J. Grünert and A. Hemmerich, *Ultracold Metastable Calcium Atoms*, Proceedings of the Sixth Symposium on Frequency Standards and Metrology in St Andrews, Fife, Scotland, 9 - 14 September 2001, to be published June 2002.
- G. Quehl, J. Grünert, V. Elman, and A. Hemmerich, *A tunable dual frequency Tm:YAG laser*, Optics Communications **190** (2001), 303–307.
- J. Grünert and A. Hemmerich, *Optimizing the production of metastable calcium atoms in a magneto-optical trap*, Applied Physics B **73** (2001), 815–818.
- A. Schoof, J. Grünert, S. Ritter, and A. Hemmerich, *Reducing the linewidth of a diode laser below 30 Hz by stabilization to a reference cavity with a finesse above  $10^5$* , Opt. Lett. **26** (2001), no. 20, 1562–1564.
- J. Grünert, G. Quehl, V. Elman, and A. Hemmerich, *Ultracold metastable calcium ensembles, a medium for matter wave amplification?*, J. Mod. Opt. **47** (2000), 2733–2740.

# Acknowledgement

Experimental physics is a team sport, even though it might seem different at times when the lab is dark late at night and the institute seems deserted. Already before I started to work on this project, my advisor Andreas Hemmerich came up with the inspiring idea for the experiment which carried us through all the often tedious labor, and he has stayed with me all along the way. If anyone then he should claim a major stake in the success of this venture.

In the first two years our group consisted only of four people, so apart from sharing the office and lab with Vladimir Elman I also had the pleasure to learn a great deal of small insights from him although we officially never worked on the same project. Gunnar Quehl and I complemented each other — his theoretical background and his freeriding pleasure in finding things out helped more than once when I was close to giving up on some intricate problem. It was a serious setback for the project to lose him to the better paying world.

The two diploma students on this project have given more than the usual share to the progress of the whole, Adrien Schoof building up the ultra-stable diode laser system in an amazingly determined style, and Stephan Ritter creating a new Ti:sapphire ring laser but most notably spending so much time on the experiment with me that we both wondered how in the world his thesis might look like. Questioning the obviousness he patiently searched solutions to the shortcomings of my sometimes rushed and flawed answers.

Dirk Hansen and Janis Mohr are taking over the project, and I wish them good luck and a lot of patience to figure out the riddles I involuntarily built into the system.

A second lab jumped into existence — due to the friendly nature of Thilo Elsässer, Boris Nagorny, and Nils Rehbein we never rivaled but instead together raised enough momentum to install a weekly seminar that Thilo kept alive, against all odds.

During the years several physicists have temporarily joined the group and contributed to the project: our Brazilian friends from Campinas University not only added some pieces to the mosaic but brought with them besides their impressive names a basket of bright smiles: Reinaldo Luiz Cavasso filho and Daniela de A. Manoel as well as their advisor Prof. Flavio C. Cruz. Vasiliy M. Entin from Novosibirsk tested our nerves with a new video camera but left us with a wealth of information on the handling of transients in current-switching applications.

Science doesn't travel on one straight road — while modern scientific experiments must be planned meticulously from the beginning still many of the vital breakthroughs base on circumstantial or at least apparently unforeseen incidents. A minor side street at first glance may turn out as the only unblocked path to the final goal. As such many conversations with friends and colleges raised my interest on vital aspects, where I want to mention

the researchers at the PTB around the calcium project, mainly Fritz Riehle and Tomas Binnewies, as well as the people at the magnesium project at Hannover, Jochen Keupp and Tanja Mehlstäubler. What better reason to miss a last train than forgetting time over discussions on physics and new experiments.

When I initially entered the lab I found an empty optical table with nothing on it, beneath or above it, not to speak of the empty drawers and shelves. Indispensable for any new experiment, the team of the mechanical workshop greatly took part in filling the void: Rainer Knut experienced most of the pitfalls in the construction of the vacuum chamber; Monika Dengler had to bear that I chose her as the contact person when her boss was absent; she, Horst Möller, Reinhold Kilian, and F. Jonas coped with the rising demand for aluminium parts resembling mass-production. More than a few of our electronic circuits would still rest on the sketch block or never have left the prototype stage without the expert help from Horst Biedermann, Reinhold Mielck, and the rest of the electronics team.

Thanks to the well maintained machinery of Uwe Pape and Frank Holweg I could adjust the shape of countless parts to suit the experiment. Egon Paeth produced specially tailored dielectric coatings, and Dieter Barlösius joined me in developing and testing the calcium discharge lamp. In times of tight university budgets it cannot be taken for granted to find a glass blower and a specialist for coatings as staff in a research institute — their expertise helps tremendously when special scientific requirements fall besides industrial standards.

Finally I very dearly want to thank my family and friends who never gave up hope that I might succeed one day, even though they more than once lost their train of thoughts in the railroad of light beams listening to my explanations when we stood in front of the puzzling machine, that large and seemingly incomprehensible refrigerator for yet so small particles.

# Curriculum Vitae

**JAN GRÜNERT**  
M.A., Dipl.Phys.

**DATE OF BIRTH** September 19th, 1971  
**PLACE OF BIRTH** Mainz  
**NATIONALITY** German  
**MARITAL STATUS/SEX** Single / Male  
**PERMANENT ADDRESS** Maienweg 286, 22335 Hamburg, Germany

## EDUCATION

**University of Hamburg** since 01.11.1997  
PhD program at the Institute for Laser-Physics (project see below)

**University of Würzburg** 24.12.1994 – 22.04.1996  
Diploma in Physics, April 1996 (“sehr gut” = best grade)  
with specialization in Geophysics

**University of Texas at Austin, USA** 15.08.1993 – 23.12.1994  
cumulative GPA: 3.66  
Master’s of Arts in Physics: December 1994

**University of Würzburg** 01.10.1990 – 01.08.1993  
Prediploma (Vordiplom) in Physics, November 1992, grade 1.8

**Schubart Gymnasium Ulm** 01.09.1981 – 30.05.1990  
Abitur, Mai 1990, average grade 1.7 (best possible is 1.0)

## PROFESSIONAL EXPERIENCE

**Institute for X-ray diagnostics at the university hospital of Würzburg**  
03.06.1996 – 30.06.1997 as diploma physicist in medical research at the MR-Tomography laboratory in fulfillment of German civil service requirements

**University of Texas at Austin, Dept. of Physics, Quantum Optics Laboratory**  
01.09.1994 – 31.10.1994: Graduate Research Assistant,

**Computer Aktuell Ulm (Firma Baumann)** 01.08.1990 – 01.10.1990: Technical service, maintenance and distribution of computer systems

## MEMBERSHIPS

Deutsche Physikalische Gesellschaft DPG, since September 1997  
 American Physical Society APS, since July 1993  
 European Student Association ESA, Austin, Texas: 08/1993 - 12/1994  
 Fachschaftsvertretung Physik, University of Würzburg: 07/1992 - 07/1993

## LANGUAGES

excellent fluency in English (US graduation), basic proficiency of French, Spanish and Latin, some experience in Chinese (Mandarin)

## RESEARCH

### **PhD Project: Ultracold metastable calcium atoms in a bichromatic magneto-optical trap**

A dense and cold ensemble of neutral calcium atoms is produced by longitudinal cooling in a Zeeman slower and consequently trapped in a magneto-optical trap at 423 nm. A second trap at 1978 nm is superimposed to the first, traps the atoms in their metastable state, and further cools them. Finally, optical pumping brings the atoms back into the ground state. A far detuned optical lattice or dipole trap will store these atoms and allow the observation of quantum-statistic phenomena.

Supervisor: Prof. A. Hemmerich, Inst. for Laser-Physics, University of Hamburg

### **Applied Physics in Medicine: In vivo $^{31}\text{P}$ -NMR-Spectroscopy of the Human Myocard**

Localized spectra of the phosphor metabolites in the myocardial wall of the left ventricle are recorded using a 1.5 Tesla all-body tomograph. A comparison of healthy individuals to patients with myocardial diseases shall determine if NMR-spectroscopy can present additional valuable information for evaluation of pathological states of the myocard. This would be the case if damages could be detected already at a cellular level before current clinical diagnostics show signs of vitality degradation.

Co-workers: Prof. Dr. Hahn, Dr. T. Pabst, Dept. for X-ray diagnostics, University Hospital of Würzburg, Germany

### **Master's Project: Laser Cooling of an Atomic Beam**

A beam of neutral rubidium atoms was slowed with radiation pressure from a counterpropagating, resonant laser beam. The changing Doppler shifts of the decelerating atoms were compensated by a spatially varying Zeeman shift which was induced by a tapered magnet coil. The theory, construction, and operation of this Zeeman slower was demonstrated by decreasing the average atomic velocity from a thermal velocity of several hundred meters per second to about 30 m/s, the capture velocity of a magneto-optic trap.

Supervisors: Dr. Daniel J. Heinzen, Dr. Jeffery R. Gardner, Dr. John W. Keto  
 University of Texas at Austin, Dept. of Physics, Austin, Texas, USA

**PERSONAL INTERESTS**

Sailing (skipper on student training vessel), piano, jazz, fencing, surfing, biking, tennis, snowboarding, skiing, chess, Chinese calligraphy

**REFERENCES** request:

**Permanent Address**

Tokajerweg 22, 89075 Ulm, Germany  
phone +49-731-51702, fax +49-731-51703

**Current Private Address**

Maienweg 286, 22335 Hamburg, Germany  
phone +49-40-50048087, mobile +49-170-8643588

**Office and Lab Address**

Institute for Laser Physics, University of Hamburg,  
Jungiusstraße 9, 20355 Hamburg, Germany  
phone +49-40-42838-4426, fax +49-40-42838-6571

**Web locations**

gruenert@physnet.uni-hamburg.de  
[www.physnet.uni-hamburg.de/ilp/hemmerich/en/gruenert.html](http://www.physnet.uni-hamburg.de/ilp/hemmerich/en/gruenert.html)